Terahertz Spectroscopic Study of Solvent Dynamics, Charge Transfer and Carrier Recombination

A thesis
submitted in partial fulfilment of the requirements
for the degree of
Doctor of Philosophy
by

Sohini Sarkar
(ID: 20113124)

Indian Institute of Science Education and Research Pune

2017

Dedicated to

Baba, Maa and Babai

IISER PUNE

भारतीय विज्ञान शिक्षा एवं अनुसंधान संस्थान, पुणे
INDIAN INSTITUTE OF SCIENCE EDUCATION AND RESEARCH (IISER) PUNE
(An Autonomous Institution of Ministry of Human Resource Development, Govt. of India)
Dr. Homi Bhabha Road, Pune - 411008.

DECLARATION

I declare that this written submission represents my ideas in my own words and wherever other's ideas have been included; I have adequately cited and referenced the original sources. I also declare that I have adhered to all principles of academic honesty and integrity and have not misrepresented or fabricated or falsified any idea / data / fact / source in my submission. I understand that violation of the above will cause for disciplinary action by the Institute and can also evoke penal action from the sources which have thus not been properly cited or from whom proper permission has not been taken when needed.

Ms. Sohini Sarkar
(ID: 20113124)

Date: 29th August 2017

भारतीय विज्ञान शिक्षा एवं अनुसंधान संस्थान, पुणे
INDIAN INSTITUTE OF SCIENCE EDUCATION AND RESEARCH (IISER) PUNE
(An Autonomous Institution of Ministry of Human Resource Development, Govt. of India)
Dr. Homi Bhabha Road, Pune - 411008.

Dr. Pankaj Mandal
Associate Professor
Department of Chemistry,
IISER Pune

CERTIFICATE

Certified that the work incorporated in the thesis entitled "***Terahertz Spectroscopic Study of Solvent Dynamics, Charge Transfer and Carrier Recombination***" submitted by **Ms. Sohini Sarkar** was carried out by the candidate, under my supervision. The work presented here or any part of it has not been included in any other thesis submitted previously for the award of any degree or diploma from any other university or institution.

Date: 29th August 2017

Dr. Pankaj Mandal
(Research Supervisor)

Acknowledgements

First and foremost, I would like to express my heartfelt gratitude to my supervisor, Dr. Pankaj Mandal for his constant support, guidance and encouragement during my PhD tenure. With utmost patience, he taught me how to build a complicated LASER lab from scratch. He has always encouraged free thinking and gave me the freedom to explore and experiment. I feel fortunate to have been his first PhD student. His strong work ethics and not settling for shortcut to achieve the goal are few virtues I would like to emulate. Sir, you have been an excellent mentor both in science and life. Thank you!

I wish to thank my Research Advisory Committee members, Dr. Sayan Bagchi, Dr. G. V. Pavan Kumar and Dr. Partha Hazra for their insightful comments, encouragement and guidance during the annual RAC meetings. I am thankful to Dr. Partha Hazra, Dr Arnab Mukherjee, Dr. Angshuman Nag and Dr. Nirmalya Ballav for giving me the opportunity to collaborate with them on several research projects. I express my gratitude towards Dr. Prasenjit Ghosh for his valuable suggestions throughout the course of this PhD program and acting as a mentor to me.

Indian Institute of Science Education and Research, Pune has undeniably provided me with the best research atmosphere. A very special gratitude goes out to our Director, Prof. Dr. K. N. Ganesh for providing us with the state of the art research facilities and generous funding required to build a high-tech Laser lab. Time and again he has supported my endeavour to attend various conferences. I would also like to thank Prof. Dr. M. Jayakannan, Chair Chemistry for his support. I thank all non-teaching and technical staffs for their support, particularly, Tushar, Mayuresh, Nayana and Anil. My special thanks to Mr. S Morrison, for taking care of our LASERs! I would also like to thank IISER, Pune for providing funding and University Grants Commission (UGC) for research fellowship. I am thankful to Chemical Abstract Service, a division of the American Chemical Society for selecting me as SciFinder Future leaders, 2014.

My heartfelt gratitude goes out to my alma mater Presidency College for inculcating in me the inquisitiveness for pursuing research. A special thanks to Dr. Sanjib Ghosh for introducing me to the intriguing world of spectroscopy, Dr. Samraggi Dutta, Dr. Pradipta Ghosh, Dr. Gautam Chattopadhyay, Dr. Sujoy Chakraborty, Dr. Swapan Chakraborty, Dr. Chaitali Mukhopadhyay, Dr. Nikhil Guchhait, Dr. Kamal Bhattacharya and Dr. Pinaki Chaudhuri for instilling in me the confidence to take challenges head on.

I wish to thank all my fellow labmates Reddy, Sneha, Avinash, Shabnum, Mayank and Aman. A special shout out to Sneha and Reddy for their significant contribution to my PhD work. The sleepless nights we worked together before deadlines, and for all the fun we have had while struggling to align optics and re doing it all over again when we moved to a new laboratory. I am thankful to have had the privilege to collaborate with Abhigyan, Debasis, Vikash, Abhishek and Plawan during my course of stay at IISER Pune. I would also like to recognize Sumit (working with Dr Umakant Rapol), Kashyap and Rejaul for providing insightful counsel.

The path to PhD was not without its ups and downs and one could not have remained sane during this period without an effective support system. Exploring culinary skills with Arundhati, pseudo intellectual debates with Kajari, gossips with Sudeshna and whole night lab sessions with Sneha made the PhD life so much fun filled. I shall always cherish the time spent with Tanmoy, Abhigyan da, Barun, Kunal, Soumya, Partha, Sagar ,Debasis, Anupam da, Biplab, Tanpreet di, Aditi, Sunil, Sumit da, Krishna and Rajkumar be it the celebration for every milestone we crossed or the unfailing encouragement when the going got tough.

Friends from yesteryears who were just a phone call away - Esha, Sritama, Mainak, Suchi, Saheli, Pritha di, Deepika, Aniruddha and Mampi, this work could not have been completed without your constant emotional support. I would also like to acknowledge my Chemistry teacher Bhui Sir, Physics teacher Majhi Sir and Maths teacher Deb Sir who made me fall in love with science.

Words may not be sufficient to express my gratitude towards my parents, Mr Pradip Sarkar and Mrs Sujita Sarkar. You both have been the pillars of my strength. A special thanks to my uncle, Mr Bikash Sarkar and aunt, Mrs Anita Biswas for their support and confidence in me. I would also like to thank my other family members and my in-laws Dr Saradindu Ghosh, Mrs Mousumi Ghosh and Samanwita Ghosh. Your prayer for me was what sustained me thus far.

Last but not the least, I would like to mention Sayantan, for providing me the strongest support even while living across the globe. Your presence is all I need.

Synopsis

The principal focus of this thesis is to utilize Terahertz as a spectroscopic tool to understand the dynamics occurring in condensed matter. A major part of this thesis work involved building the THz spectrometer using the output from an amplified ultrafast laser system and using ambient air for the generation and detection of broadband (0.5 – 15) THz radiation. Since 1 THz corresponds to 1 ps in timescale and 4 meV in energy, it strongly interacts with systems having a lifetime in picosecond timescale and energies in meV range like relaxation dynamics and low frequency intermolecular vibrational modes of various solvents, exciton transitions in bulk and nanostructured materials, carrier recombinations in semiconductor materials, etc. Also, time-resolved THz spectroscopy which gives evolution of far infrared spectrum after an optical excitation provides a noncontact ac probe of complex conductivity. This noncontact conductivity measurement becomes particularly important for semiconductor nanoparticles where attaching wires is physically improbable, and the carrier dynamics is in ps time scale.

Chapter 1. *Introduction:* In this chapter, a brief introduction to Terahertz (THz) spectroscopy is given. In THz spectroscopy, the transient electric field of the THz waveform is mapped in time, Fourier transformation of which allows resolving amplitude and phase of the spectral components making up the pulse in contrast to other spectroscopic techniques that give only intensity information. This chapter briefly describes the potential of Terahertz as a spectroscopic tool since it can be used to study solvent dynamics, charge transfer and carrier recombination dynamics in nanoparticle and bulk semiconductors.

Chapter 2. *Instrumentation and Data Analysis:* This chapter describes the setup of the time-domain THz spectrometer in detail. It also describes the setup used for doing optical pump THz probe experiments, also known as time-resolved THz spectroscopy (TRTS). Further, this chapter describes how various useful parameters like complex refractive index, complex conductivity, and complex dielectric function can be calculated from the recorded THz electric field.

Chapter 3. *Broadband Terahertz Dielectric Spectroscopy of Alcohols:* Complex dielectric properties of a series of alcohols in wide (0.5-10 THz) frequency range using

THz time-domain spectroscopy (THz-TDS) is reported. Because of the complexities involved in generating a broadband THz pulse, previous studies in this frequency regime were limited to 5 THz.

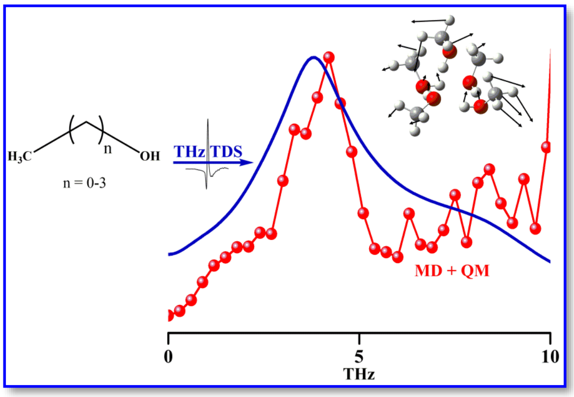

Figure 1. Experimentally observed (blue) and theoretically predicted (red) absorbance of methanol in the THz frequency range of 0.5 – 10 THz.

The dielectric response observed has contributions from a Debye relaxation process and three damped harmonic oscillators. Combination of experimental observations and all-atom molecular dynamics (MD) simulations and *ab initio* quantum calculations reveals that the complex dielectric spectra of alcohols result from a complex dynamics involving vibrational motions of several atoms across multiple interacting alcohol molecules. Primarily three types of motions were identified: the overall motion of alcohol molecules give rise to peak close to 2 THz, the peaks in intermediate frequency range (4-6 THz) are due to alkyl group oscillations, and the peaks at higher frequency range are probably the signatures of the movement of H-bonded OH groups of the alcohol molecules. The present work, therefore, aims to expand the scope and understanding of liquid dynamics while at the same time complements previous studies on alcohols at lower frequencies.

Publication from this chapter:

Broadband Terahertz Dielectric Spectroscopy of Alcohols

Sohini Sarkar, Debasis Saha, Sneha Banerjee, Arnab Mukherjee*, and Pankaj Mandal*

Chemical Physics Letters **2017**,*678,* 65-71

Chapter 4. ***Hot Electron and Hole Transfer from Colloidal CsPbBr$_3$ Perovskite Nanocrystals:*** Efficient interfacial transfer of photogenerated electrons and holes, essential for a good photovoltaic and photocatalytic material, is studied in CsPbBr$_3$ NCs in presence of benzoquinone (BQ) and phenothiazine (PTZ) molecules as electron and hole acceptors, respectively, using time resolved THz spectroscopy (TRTS).

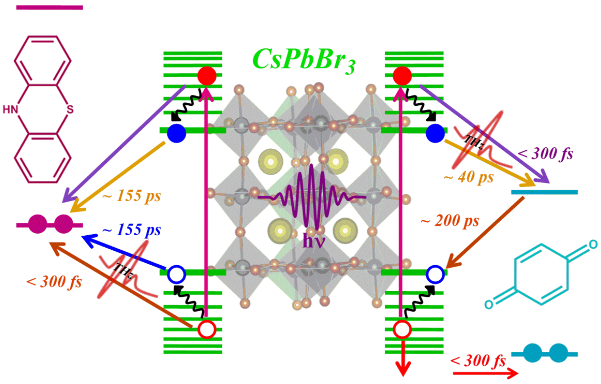

Figure 2. Schematic showing ultrafast hot carrier transfer (sub- 300 fs time scale) followed by secondary transfer of thermalized electrons (~ 40 ps) and holes (~ 155 ps) from CsPbBr$_3$ NCs in presence of BQ and PTZ as electron and hole acceptors, respectively.

Efficient hot electron/hole transfer with a sub-300 fs timescale is the major channel of carrier transfer, thus overcomes the problem related to Auger recombination. A secondary transfer of thermalized carriers also takes place with time scales of 20-50 ps for electrons and 137-166 ps for holes. This work suggests that suitable interfaces of CsPbX$_3$ NCs with electron and hole transport layers would harvest hot carriers, increasing the photovoltaic and photocatalytic efficiencies.

Publication from this chapter:

Terahertz Spectroscopic Probe of Hot Electron and Hole Transfer from Colloidal CsPbBr$_3$ Perovskite Nanocrystals

Sohini Sarkar, Vikash Kumar Ravi, Sneha Banerjee, Gurivi Reddy Yettapu, Ganesh B. Markad, Angshuman Nag, and Pankaj Mandal*

Nano Letters **2017**, *17*, 5402–5407

Chapter 5. ***Effect of Capping Ligand Engineering on Carrier Dynamics in $CsPbI_3$ Nanocrystals:*** Cubic phase $CsPbI_3$ NCs are highly sought after solar cell material due to their appropriate band gap of 1.73 eV. Nevertheless, the NCs are capped by insulating ligands. For utilizing these NCs in device fabrication, dot-to-dot electronic transport is essential which can be achieved by removal of the capping ligands by washing with methyl acetate and lead acetate.

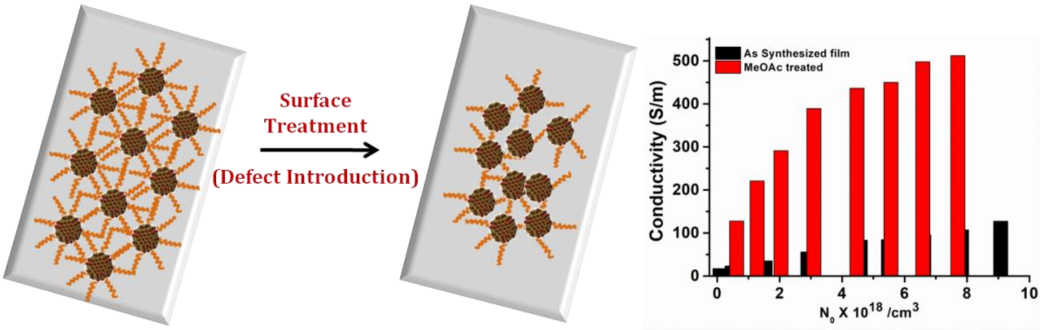

Figure 3. Schematic showing the effect of surface treatment on NC film. A significant increase in photoconductivity for ligand treated films is observed.

TRTS has been used to study the photoconductivity and mobility of as-cast, methyl acetate, and lead acetate treated $CsPbI_3$ NC films on nonconducting substrate. We see that ligand treatment enhances inter NC coupling but also introduces new defect states confirmed by the presence of a new decay pathway for the treated films. However, the resultant effect of ligand treatment is beneficial.

Publication from this chapter:

Effect of Capping Ligand Engineering on Carrier Dynamics in $CsPbI_3$ Nanocrystals

Sohini Sarkar, Abhishek Swarnkar, Sneha Banerjee, Angshuman Nag, and Pankaj Mandal*
(manuscript under preparation)

Chapter 6. ***Understanding Carrier Dynamics in Reduced Graphene Oxide (rGO) Film:*** Film of reeeduced graphene oxide (rGO) synthesized by Jha *et al.* using a novel method exhibits a remarkable all-solid-state supercapacitor performance. Employing TRTS, we have measured the photoconductivity and studied the carrier dynamics in this rGO film. The ac conductivity of the rGO film measured using the noncontact TRTS technique is similar to the dc conductivity value determined by four probe I-V measurements. The overall carrier dynamics is very similar to that reported for single layer graphene.

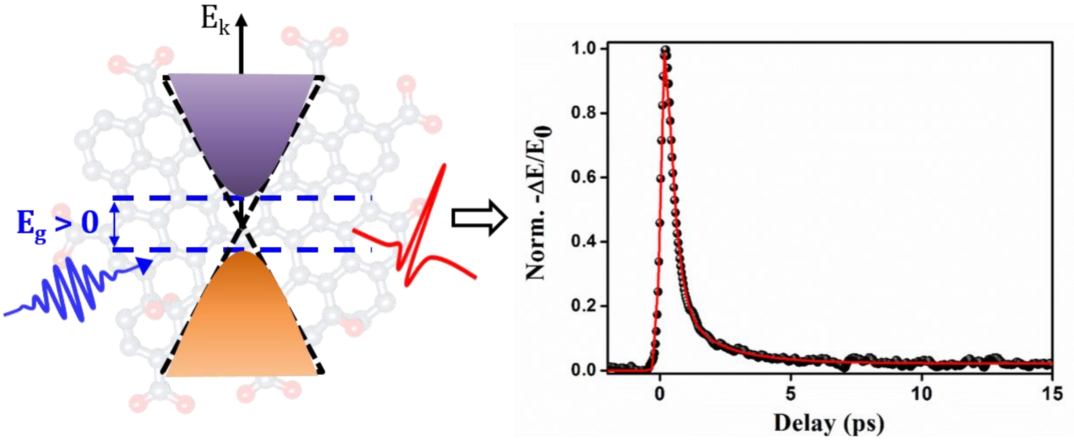

Figure 4. Schematic showing the band structure in rGO. Rapid relaxation of hot carriers is observed.

The rapid relaxation of carriers in the rGO film is mainly dictated by 1) optical phonon emissions (< 300 fs), 2) disorder mediated acoustic phonon emissions of thermalized carriers (1-2 ps), and 3) inefficient slow relaxation of electrons and holes in deep trap states (50-200 ps).

Publication from this chapter:

Understanding Carrier Dynamics in Reduced Graphene Oxide (rGO) Film

Sohini Sarkar, Plawan Kumar Jha, Sneha Banerjee, and Pankaj Mandal*

(manuscript under preparation)

Contents

Glossary of Acronyms

BQ	: Benzoquinone
CB	: Conduction Band
$CsPbBr_3$	: Cesium lead bromide
$CsPbI_3$	: Cesium lead iodide
DFT	: Density Functional Theory
EO	: Electro-optic
fs	: femtosecond
FWM	: Four wave mixing
GO	: Graphene oxide
HDPE	: High density polyethylene
HMN	: 2,2,4,4,6,8,8-heptamethyl nonane
HRTEM	: High resolution Transmission Electron Microscope
IR	: Infrared
LASER	: Light Amplification by Spontaneous Emission of Radiation
MD	: Molecular Dynamics
meV	: milli electron volt
mm	: millimetre
ms	: millisecond
NC	: Nanocrystal
nm	: nanometre
NMR	: Nuclear magnetic resonance
OPTP	: Optical pump THz probe
PC	: Photoconductive
PL	: Photoluminescence
PMT	: Photomultiplier tube

ps	: picosecond
PTZ	: Phenothiazine
rGO	: reduced graphene oxide
SEM	: Scanning electron microscope
SHG	: Second Harmonic Generation
TA	: Transient absorption
TDS	: Time Domain Spectroscopy
TFISH	: Terahertz field induced second harmonic
THz	: Terahertz
Ti	: Titanium
TPX	: polymethyl pentene
TRMC	: Time Resolved Microwave Conductivity
TRTS	: Time Resolved THz Spectroscopy
TW	: Terawatt
UV-vis	: Ultraviolet-visible
VACF	: Velocity Autocorrelation Function
VB	: Valence band
VDOS	: Vibrational Density of States
Λ	: Lambda
µm	: micrometre
µs	: microsecond

Chapter 1

Introduction

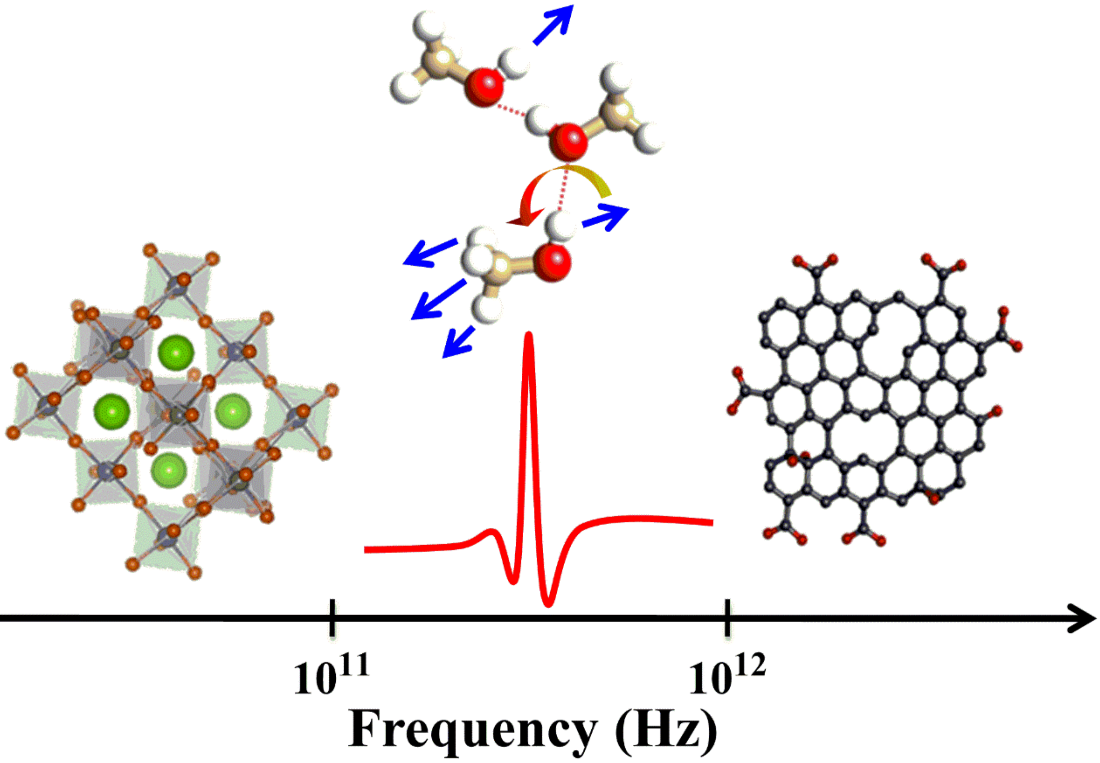

1 THz ~ 1 ps ~ 300 μm ~ 33.3 cm^{-1} ~ 4 meV

1.1 Introduction to Terahertz Spectroscopy

Terahertz (THz) Spectroscopy, a relatively new spectroscopic technique has immense potential of providing significant insights into numerous physical, chemical and biological processes occurring on the picosecond time scale with energies in meV range. THz spectroscopy roughly spans from 0.3 to 20 THz where 1 THz corresponds to 33.3 cm^{-1} in wavenumber, 4 meV in energy and 300 μm in wavelength. Nevertheless, THz (also referred to as far-infrared) region of the electromagnetic spectrum flanked by microwave in the lower frequency range and infra-red at the higher frequency range (Figure 1.1) was hard to pin down. For an extended period, the low-frequency part couldn't be accessed electronically and the high-frequency part couldn't be accessed optically creating a gap in the electromagnetic spectrum commonly known as the Terahertz Gap.[1-3] Only after the invention of ultrafast LASERs this region could be accessed since THz generation and detection relies on ultrafast pulses.[4,5]

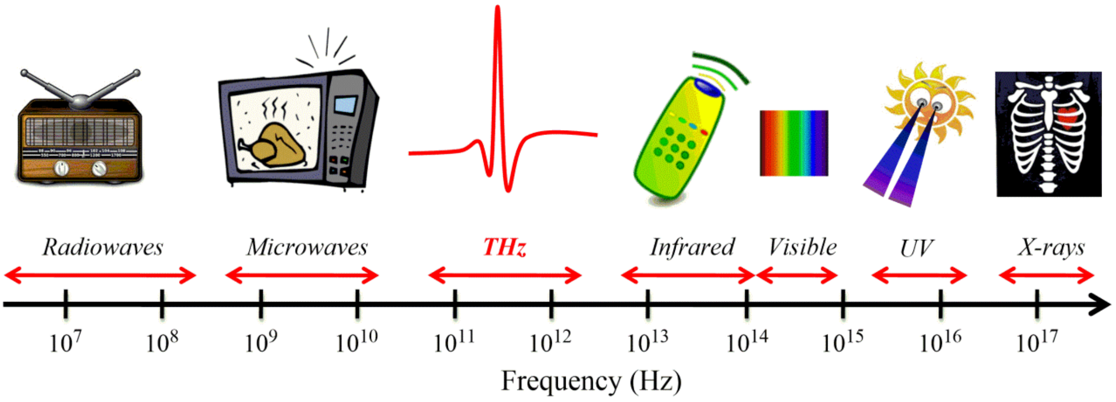

Figure 1.1 Schematic of electromagnetic spectrum showing THz lies between microwave and IR region.

In standard bench top experiments, THz pulses are generated and detected using ultrashort laser pulses from Ti-sapphire lasers with pulse width varying from ~100-10 fs. Since a fs gating beam is used to map the ps-THz waveform, coherent detection can be accomplished. Furthermore, since the transient electric field of the THz waveform is mapped in the time domain, Fourier transformation of it allows resolving amplitude and phase of the spectral components making up the pulse in contrast to other spectroscopic techniques that give only intensity information. From the amplitude, one can calculate absorption coefficient and from phase, the refractive index of the sample can be calculated. Hence the complex-valued permittivity can be evaluated without involving Kramers-Kronig analysis.[6] Since fs laser pulses are used for THz detection, time resolved THz study with sub-picosecond temporal resolution can be carried out as well. Though free electron lasers or synchrotrons produce highly intense far IR pulses with ~3 ps or greater duration, they are more expensive and less accessible compared to the table top ultrafast laser setup that produces THz radiation with equal or more brightness.

According to Maxwell's equations, electric current varying with time emits electromagnetic radiation. Using this knowledge, the generation and detection of far IR light as a freely propagating radiation from transmission lines was pioneered by Dan Grischkowsky, David Auston and Martin Nuss.[4,7] Free propagation of radiation marked the genesis of THz Time Domain Spectroscopy where one could place a sample between the THz emitter and detector.

To begin with, the effort was predominantly directed towards pulsed THz generation and detection by different methods and understanding the theory behind the same.[8] There are different methods of pulsed THz generation and detection using fs light, the oldest one being using photoconductive antennas.[7,9-14] Photoconductive THz generation is a resonant process where optical excitation causes interband transition and stimulates conductivity alteration. Second and more popular method of THz generation and detection is a non-resonant process that involves use of nonlinear crystals.[15-19] Most recent method involves utilizing ambient air for broadband THz generation and detection.[20-22] The generation and detection of THz radiation from air are described in detail in Chapter 2.

1.2 THz as a Spectroscopic Tool

1.2.1 Time Domain THz Spectroscopy

Terahertz radiation has several applications[23] of which the optoelectronic applications involving security screening,[24-26] imaging,[27-31] quality control of pharmaceutical products,[32-34] and as a spectroscopic tool have been extensively studied.[6,35-38] 1 THz corresponds to 1 ps in timescale and 4 meV in energy. Thus, THz radiation will strongly interact with systems having a lifetime in picosecond timescale and energies in meV range. Dipole relaxation dynamics and low frequency intermolecular vibrational modes of various solvents,[39-42] low-frequency vibrational modes of diverse biological matters,[43-50] exciton transitions in bulk and nanostructured materials,[51-53] free charges,[54] phonon vibrations in semiconductors and crystalline solids[55,56] are few examples of such systems which strongly couple to THz radiations.

In this thesis work, THz spectrometer which has an ultra-broad bandwidth of 0.5 – 15 THz has been built utilizing ambient air for THz generation and detection.[21,22] Subsequently, the prospective of THz as a spectroscopic tool has been exploited by employing THz time-domain and time-resolved THz study to investigate different systems in the condensed phase. THz time-domain spectroscopy (THz-TDS) experiment have been performed in transmission mode and is like steady state absorption spectroscopy in which a freely propagating electromagnetic pulse transmits through the sample to be studied and falls onto the detector. However, unlike classical absorption spectrometers in which intensity is measured, in THz-TDS the electric field of the transmitted THz pulse is measured as a function of time; hence the name "Time Domain". A detailed description of THz-TDS setup is given in Chapter 2. Figure 1.2 shows the representative electric field of THz waveforms transmitted through the empty cell (red) and sample (blue) recorded as a function of time.

THz TDS gives information on transmittance and phase difference from which absorption (α) and refractive index (n) of a sample can be computed respectively.

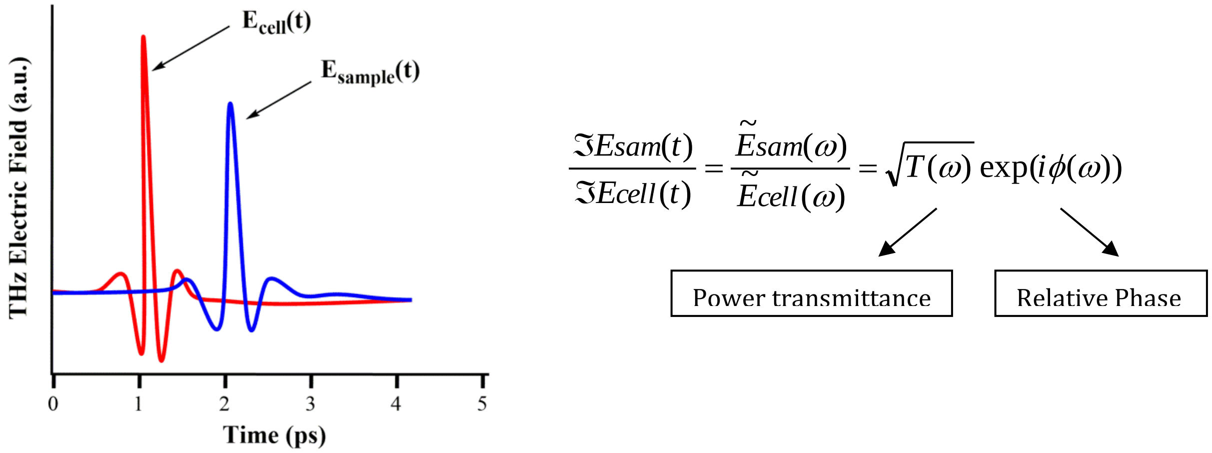

$$\frac{\Im Esam(t)}{\Im Ecell(t)} = \frac{\tilde{E}sam(\omega)}{\tilde{E}cell(\omega)} = \sqrt{T(\omega)}\,\exp(i\phi(\omega))$$

Figure 1.2. THz-TDS waveforms transmitted through empty cell (red) and sample (blue). Fourier transformation of electric field in time domain gives amplitude and phase of spectral components making up the THz pulse.

Further, using α and n other parameters like extinction coefficient (k), complex refractive index ($\hat{n}$), complex dielectric function ($\hat{\varepsilon}$), and complex conductivity ($\hat{\sigma}$), can be evaluated.

1.2.2 Understanding Solvent Dynamics

THz-TDS can be used to study the complex dielectric function of liquid molecules. The reorientation of liquid dipoles, either permanent dipoles in polar (water, alcohols)[39,41,43] or collision-induced dipoles in nonpolar (benzene, carbon tetrachloride) liquids[57-59] occurring in picosecond timescales is manifested as their dielectric response in the lower THz frequency region. When an oscillating electric field interacts with liquid molecules, the dipoles associated with the molecules tend to keep up with the oscillating field by aligning themselves to the field. The dielectric response is a measure of it. The electric field creates an induced polarization in the liquids,

$$\vec{P} = (\varepsilon - \varepsilon_0)\vec{E}$$

where ε_0 is the vacuum permittivity.

When the frequency of the oscillating field is much higher than liquid reorientation frequency, there is a lag between the applied field frequency and alignment of the dipole which leads to a drop in the dielectric function(ε). So, frequency dependent dielectric study provides information on reorientation dynamics of liquids.

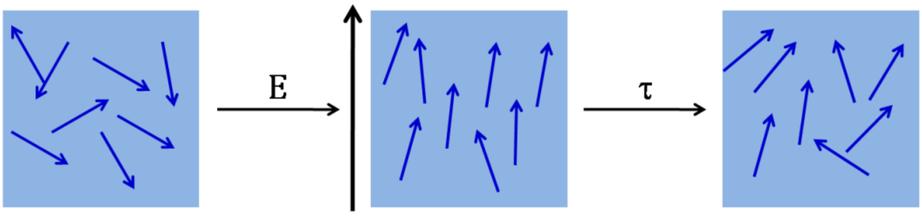

Figure 1.3 Schematic showing alignment of liquid dipoles in presence of external electric field followed by the relaxation of the dipoles.

When the frequency of the applied field surpasses the reorientation timescale of the liquids, it becomes resonant with the low-frequency infrared (IR) active modes of the liquid that no longer involve dielectric relaxation. For polar liquids, such modes appear in the THz region and hence THz acts as a bridge between the low-frequency dielectric relaxation dynamics and high-frequency oscillatory motions of the liquids.[39,41]

Understanding relaxation dynamics and low frequency intermolecular vibrational modes is crucial from the biological and chemical standpoint.[60,61] Relaxation timescales of liquids influence the rate of chemical reactions as increased solvation of transition state may reduce the activation energy thereby increasing the reaction rate. Besides the solutes in an excited state, stabilize by transferring intramolecular vibrational energy to the low-frequency intermolecular modes of the liquids. Therefore, solvent milieu affects both kinetics and thermodynamics of chemical reactions.

We utilized THz TDS to study the frequency dependent complex dielectric function of five mono-hydroxy alcohols: methanol, ethanol, 1-propanol, 2-propanol, and 1-butanol. A high-frequency tail of Debye relaxation was observed with the time scale of 0.7-2 ps and was attributed to H bond breaking and making. Beyond 1 THz oscillatory motions in the alcohols originating from intermolecular vibrations became prominent. With the help of Molecular Dynamics simulation and *ab-initio* calculations modes giving rise to absorption at different THz frequencies was assigned. Chapter 3 describes this work in detail.

1.2.3 Time Resolved THz Spectroscopy

Time-resolved THz spectroscopy (TRTS) also known as Optical Pump THz Probe (OPTP) is an extension of time-resolved or pump probe technique in the far IR region. In typical pump probe experiments sample is first excited with a relatively intense ultrafast laser (pump) pulse followed by monitoring the temporal evolution of the optical constants of the sample with weaker probe pulse. Figure 1.4 shows typical pump probe setup.

Pump and probe pulses spatially overlap onto the sample and the delay between the pump and probe pulses is adjusted by moving the variable delay stage. The pump pulse first passes through the sample which excites the sample and then the probe pulse monitors the evolution of the photoexcited sample as a function of the pump probe delay. TRTS is a subset of the pump probe technique.

Pump and probe pulses spatially overlap onto the sample and the delay between the pump and probe pulses is adjusted by moving the variable delay stage. The pump pulse first passes through the sample which excites the sample and then the probe pulse monitors the evolution of the photoexcited sample as a function of the pump probe delay.

TRTS is a subset of the pump probe technique.

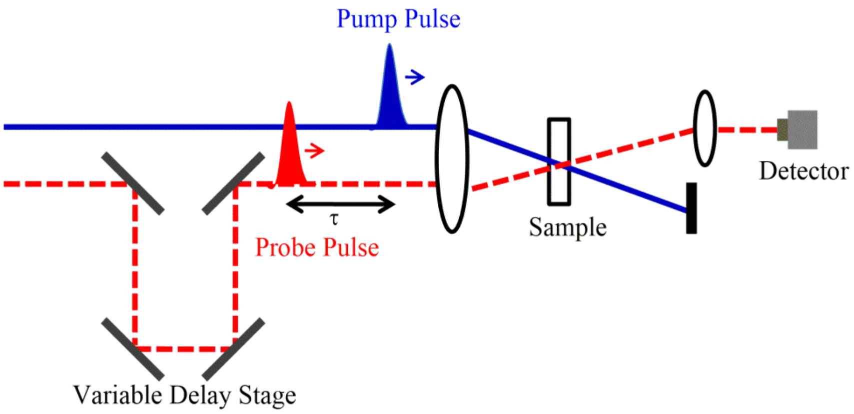

Figure 1.4 Schematic of pump-probe setup. Pump pulse (blue) excites the sample and the probe pulse (red) monitors the optical properties. τ is the delay between the pump and the probe pulse adjusted by the variable delay stage.

Pump and probe pulses spatially overlap onto the sample and the delay between the pump and probe pulses is adjusted by moving the variable delay stage. The pump pulse first passes through the sample which excites the sample and then the probe pulse monitors the evolution of the photoexcited sample as a function of the pump probe delay. TRTS is a subset of the pump probe technique.

Advancements in THz-TDS laid the foundation for TRTS. [62] As mentioned earlier, in contrast to classical spectroscopic methods since THz-TDS engages generation and detection of optically gated THz pulses, it can be aptly utilized for exploring nonequilibrium states created by optical excitation with sub picosecond resolution.[51,63] This attribute of THz-TDS enabled development of optical pump THz probe experiments in which weaker THz pulses are used to probe the pump induced far-infrared changes of the susceptibility spectrum of the sample.[63] Essentially there are two ways of conducting the TRTS experiments. One is to position the sample at peak of THz waveform and vary the pump probe delay to map out the pump induced change in THz peak amplitude. This gives an average response of the sample over the experimental temporal window. This is commonly referred to as frequency averaged THz study.[6] Second method is to scan the entire THz probe waveform at several fixed pump probe delay times following photoexcitation by the optical pump. A meticulous study can be carried out by creating a 2D grid that builds the THz waveform at several narrowly spaced pump delay times. This is generally called the frequency resolved THz study.[6] Details of TRTS technique is described in Chapter 2.

The conductivity in bulk or nanocrystal semiconductor arises due to free and weakly bound carriers that have low excitation energies.[64] The exciton binding energies and optically active exciton transitions occur in meV range. Again, the carrier phonon scattering occurs in a sub-ps time scale that gives rise to dispersion in the dielectric spectrum in meV energy scales.[65] Thus, TRTS is a significant tool to study these carriers since 1 THz corresponds to ~ 4 meV in energy.

1.2.4 Interaction of THz radiation with photoexcited semiconductor NCs

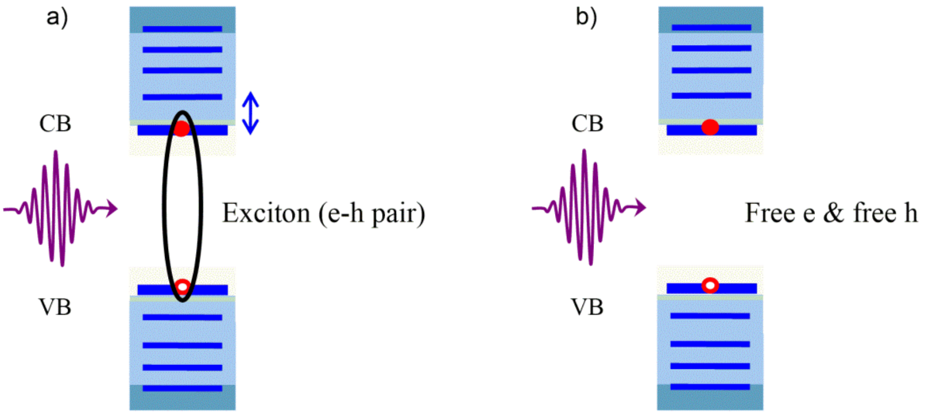

Figure 1.5 Creation of a) excitons and b) free carriers on above bandgap excitations.

Above band gap excitation of the nanocrystals may create either excitons or free carriers. THz can interact with the excitons and it is nonresonant interaction since THz energy is much less compared to intraband excitation energy. Yet there will be a change in polarizability which is manifested in the form of AC dielectric function.[66] When free carriers are formed on above band gap excitation, THz photon energies are transferred to the carriers. This is a resonant interaction where the acceleration of charge carriers in presence of THz radiation results in an increase of real conductivity.

Using TRTS, semiconductor properties like pump induced photoconductivity, mobility and diffusion length can be measured along with understanding the nature of carriers formed, their recombination pathways and carrier-phonon scattering.[51,67] TRTS is the solitary tool for sub-ps non-contact electrical measurements for semiconductor nanocrystals where it is difficult to attach wires for conductivity measurements and when carrier recombination time scale is in ps. TRTS measures the local ac conductivity of the sample and is insensitive to defects that encumber long range charge transport.[68] Per se THz measurements yield intrinsic upper limits for carrier transfer.

1.2.5 TRTS of Colloidal $CsPbX_3$ Nanocrystals

Fossil fuels are the worldwide major energy source, but we will shortly run out of them. Also, burning fossil fuels result in the enormous emission of greenhouse gases that are accountable for global warming.[69] Consequently, there is a pressing need to explore renewable energy sources and sun is a potential source of inexhaustible renewable energy. Scientists are striving to achieve durable and cheap photovoltaic devices that convert solar energy to electricity. Silicon based solar cells that dominate the photovoltaics market today are expensive. Recently, a new genre of thin film photovoltaic cells using hybrid organic inorganic perovskites have surfaced that entails low-cost fabrication and have shown outstanding device performance by achieving >22 % power conversion efficiency in a brief span.[70-75] Perovskites are the class of compounds that have a crystal structure similar to $CaTiO_3$. The general formula for perovskite structure is ABX_3 where A is organic cation (methylammonium or formamidinium), B = Pb/Sn/Ge and X = halide anion (Cl/Br/I).[54,76] Perovskites were first used in photovoltaics as methylammonium lead tri-iodide in 2009.[73] They exhibit high charge carrier mobility, long diffusion lengths, low exciton binding energies and appropriate band gap for broad solar spectrum absorption.[77,78] Nonetheless the organic cation makes them vulnerable to environmental stress.[79] They tend to dissociate into CH_3NH_3X and PbX_2. All inorganic perovskites are more robust since they are more heat and moisture resistant.[80,81] Bulk $CsPbX_3$ were already known for more than 50 years.[82] Very recently Kovalenko and co-workers reported the synthesis of low-cost solution processed $CsPbX_3$ nanocrystals whose excellent optical properties make them an exceptional choice to be used in optoelectronic devices.[83-85] Composition and size tunable $CsPbX_3$ show band gap energies and emission spectra that can be tuned over the entire visible range. They have very high quantum yield (> 80 %), narrow emission bandwidth (~ 85 meV), and exhibit reduced fluorescence blinking.[83,86] These materials also have a very low threshold (~ 5 μJ/cm^2) lasing capability that can be tuned across the entire visible spectral range. Recently

$CsPbBr_3$ NCs were used as photo catalyst for converting CO_2 into solar fuel in presence of non-aqueous solvents.[87] Defect tolerant nature of the NCs is attributed to be the reason for their excellent optical properties.[85] It is important to note that all these alluring optical properties of the perovskite nanocrystals are their excited state features and that's why understanding their excited state photophysics is crucial.[88] Several time resolved studies like time resolved photoluminescence, transient absorption, and TRTS are employed to investigate their excited state properties.[68,86,89]

Other time resolved techniques using visible or IR light though provide time scales for carrier recombination, they are unable to measure conductivity and mobility. Further visible or IR studies mostly investigate the conduction band dynamics. TRTS is an exclusive non-contact ac probe to measure carrier dynamics (both electron and hole) and semiconductor properties like conductivity, mobility and diffusion length. In chapter 4 and 5, we have utilized TRTS to investigate the charge transfer and carrier recombination processes occurring in colloidal $CsPbX_3$ NCs in solution and in thin films.

1.2.6 THz study of Reduced Graphene Oxide

Graphene, an allotrope of carbon is made up of tightly packed sp^2 hybridized carbon atoms organized in a two-dimensional honey comb lattice. It has a unique band structure with a zero band gap that is responsible for its remarkable optical and electronic properties.[90-94] Graphene has shown potential applications in photovoltaic cells,[95,96] mode-locked lasers,[97] supercapacitors, photodetectors,[98] etc. A cost effective way of manufacturing large scale graphene is by reduction of graphene oxide (GO), obtained by chemical exfoliation of graphite.[99,100] Recently, Jha *et al.* have synthesized rGO using a novel technique where a moderate reducing agent has been used to reduce GO (Jha *et al.* Chem 2017, in press). The rGO synthesized by this method exhibits a remarkable all-solid-state supercapacitor performance without any further treatment. In chapter 6, we have measured the photoconductivity and studied the carrier dynamics in rGO film using TRTS. The ac conductivity of the rGO film measured using the noncontact TRTS technique is similar to the dc conductivity value determined by four probe I-V measurements. The overall carrier dynamics is very similar to that reported for single layer graphene. The rapid relaxation of carriers in the rGO film is mainly dictated by 1) optical phonon emissions (< 300 fs), 2) disorder mediated acoustic phonon emissions of thermalized carriers (1-2 ps), and 3) inefficient slow relaxation of electrons and holes in deep trap states (50-200 ps).

1.3 References

(1) Clough, B.; Dai, J.; Zhang, X.-C. *Mater. Today* **2012**, *15*, 50-58.
(2) Gwyn, P. W. *Rep. Prog. Phys* **2006**, *69*, 301.
(3) Tonouchi, M. *Nat Photon* **2007**, *1*, 97-105.
(4) van Exter, M.; Fattinger, C.; Grischkowsky, D. *Opt. Lett* **1989**, *14*, 1128-1130.
(5) Kafka, J. D.; Watts, M. L.; Pieterse, J. W. J. *IEEE J. Quant. Electron***1992**, *28*, 2151-2162.
(6) Schmuttenmaer, C. A. *Chem. Rev* **2004**, *104*, 1759-1780.
(7) Smith, P. R.; Auston, D. H.; Nuss, M. C. *IEEE J. Quant. Electron* **1988**, *24*, 255-260.
(8)Ferguson, B.; Zhang, X.-C. *Nat Mater* **2002**, *1*, 26-33.
(9) Fattinger, C.; Grischkowsky, D. *Appl. Phys. Lett* **1989**, *54*, 490-492.
(10) Exter, M. v.; Fattinger, C.; Grischkowsky, D. *Appl. Phys. Lett* **1989**, *55*, 337-339.
(11) Exter, M. v.; Grischkowsky, D. R. *IEEE Trans. Microw. Theory Tech.* **1990**, *38*, 1684-1691.
(12) Tani, M.; Matsuura, S.; Sakai, K.; Nakashima, S.-i. *Appl. Opt* **1997**, *36*, 7853-7859.
(13) Martin, M.; Ming, X.; Roman, J. B. D.; Harald, K.; Bernd, S.; Harald, S.; Manfred, H.; Stephan, W. *Nanotechnology* **2013**, *24*, 214007.
(14) Shen, Y. C.; Upadhya, P. C.; Beere, H. E.; Linfield, E. H.; Davies, A. G.; Gregory, I. S.; Baker, C.; Tribe, W. R.; Evans, M. J. *Appl. Phys. Lett* **2004**, *85*, 164-166.
(15) Gallot, G.; Grischkowsky, D. ***J. Opt. Soc. Am. B*** **1999**, *16*, 1204-1212.
(16) Auston, D. H.; Nuss, M. C. *IEEE J. Quant. Electron* **1988**, *24*, 184-197.
(17) Carrig, T. J.; Rodriguez, G.; Clement, T. S.; Taylor, A. J.; Stewart, K. R. *Appl. Phys. Lett* **1995**, *66*, 121-123.
(18) Hu, B. B.; Zhang, X. C.; Auston, D. H.; Smith, P. R. *Appl. Phys. Lett* **1990**, *56*, 506-508.
(19) Nahata, A.; Weling, A. S.; Heinz, T. F. *Appl. Phys. Lett* **1996**, *69*, 2321-2323.
(20) Xie, X.; Dai, J.; Zhang, X. C. *Phys. Rev. Lett* **2006**, *96*, 075005.
(21) Dai, J.; Xie, X.; Zhang, X. C. *Phys. Rev. Lett* **2006**, *97*, 103903.
(22) Dai, J.; Zhang, X.-C. *Phys. Rev. Lett* **2009**, *94*, 021117.
(23) Jepsen, P. U.; Cooke, D. G.; Koch, M. *Laser Photon.Rev* **2011**, *5*, 124-166.
(24) Kawase, K.; Ogawa, Y.; Watanabe, Y.; Inoue, H. *Opt. Express* **2003**, *11*, 2549-2554.
(25) Karpowicz, N.; Zhong, H.; Zhang, C.; Lin, K.-I.; Hwang, J.-S.; Xu, J.; Zhang, X.-C. *Appl. Phys. Lett* **2005**, *86*, 054105.
(26) Ma, Y.; Yan, L.; Seminario, J. M. **2006,** 6212, 621204-621208.
(27) Siegel, P. H. *IEEE Trans. Microw. Theory Tech.* **2004**, *52*, 2438-2447.
(28) Woodward, R. M.; Wallace, V. P.; Pye, R. J.; Cole, B. E.; Arnone, D. D.; Linfield, E. H.; Pepper, M. *J. Invest. Dermatol* **2003**, *120*, 72-78.
(29) Hu, B. B.; Nuss, M. C. *Opt. Lett* **1995**, *20*, 1716-1718.
(30) Jansen, C.; Wietzke, S.; Peters, O.; Scheller, M.; Vieweg, N.; Salhi, M.; Krumbholz, N.; Jördens, C.; Hochrein, T.; Koch, M. *Appl. Opt* **2010**, *49*, E48-E57.
(31) Son, J.-H. *J. Appl. Phys* **2009**, *105*, 102033.
(32) Taday, P. F. *Philosophical Transactions of the Royal Society of London. Series A: Mathematical, Physical and Engineering Sciences* **2004**, *362*, 351-364.
(33) Taday, P. F.; Bradley, I. V.; Arnone, D. D.; Pepper, M. *J. Pharm. Sci* **2003**, *92*, 831-838.
(34) Zeitler, J. A.; Kogermann, K.; Rantanen, J.; Rades, T.; Taday, P. F.; Pepper, M.; Aaltonen, J.; Strachan, C. J. *Int. J. Pharm* **2007**, *334*, 78-84.

(35) Němec, H.; Kužel, P.; Sundström, V. *J Photochem Photobiol A Chem* **2010**, *215*, 123-139.
(36) Beard, M. C.; Turner, G. M.; Schmuttenmaer, C. A. *J. Phys. Chem B* **2002**, *106*, 7146-7159.
(37) Beard, M. C.; Turner, G. M.; Schmuttenmaer, C. A. *J. Phys. Chem A* **2002**, *106*, 878-883.
(38) Baxter, J. B.; Guglietta, G. W. *Anal. Chem* **2011**, *83*, 4342-4368.
(39) Kindt, J.; Schmuttenmaer, C. *J. Phys. Chem* **1996**, *100*, 10373-10379.
(40) Nagai, M.; Yada, H.; Arikawa, T.; Tanaka, K. *J Infrared Millim Terahertz Waves* **2006**, *27*, 505-515.
(41) Venables, D. S.; Schmuttenmaer, C. A. *J. Phys. Chem* **2000**, *113*, 11222-11236.
(42) Sato, T.; Buchner, R. *J. Phys. Chem A* **2004**, *108*, 5007-5015.
(43) Tielrooij, K. J.; Paparo, D.; Piatkowski, L.; Bakker, H. J.; Bonn, M. Biophys. J. **2009**, *97*, 2484-2492.
(44) He, Y.; Ku, P. I.; Knab, J. R.; Chen, J. Y.; Markelz, A. G. *Phys. Rev. Lett* **2008**, *101*, 178103.
(45) Arikawa, T.; Nagai, M.; Tanaka, K. *Chem. Phys. Lett* **2008**, *457*, 12-17.
(46) Walther, M.; Fischer, B. M.; Uhd Jepsen, P. *J. Chem. Phys* **2003**, *288*, 261-268.
(47) Heyden, M.; Bründermann, E.; Heugen, U.; Niehues, G.; Leitner, D. M.; Havenith, M. *J. Am. Chem. Soc* **2008**, *130*, 5773-5779.
(48) Born, B.; Weingärtner, H.; Bründermann, E.; Havenith, M. *J. Am. Chem. Soc* **2009**, *131*, 3752-3755.
(49) Heugen, U.; Schwaab, G.; Bründermann, E.; Heyden, M.; Yu, X.; Leitner, D. M.; Havenith, M. Proc *Natl Acad Sci U.S.A* **2006**, *103*, 12301-12306.
(50) Kim, S. J.; Born, B.; Havenith, M.; Gruebele, M. *Angew. Chem. Int.***2008**, *47*, 6486-6489.
(51) Beard, M. C.; Turner, G. M.; Schmuttenmaer, C. A. *Phys. Rev. B* **2000**, *62*, 15764-15777.
(52) Grischkowsky, D.; Keiding, S.; van Exter, M.; Fattinger, C. *J. Opt. Soc. Am. B* **1990**, *7*, 2006-2015.
(53) Groeneveld, R. H. M.; Grischkowskyt, D. *J. Opt. Soc. Am. B* **1994**, *11*, 2502-2507.
(54) Herz, L. M. *Annu. Rev. Phys. Chem* **2016**, *67*, 65-89.
(55) Schall, M.; Walther, M.; Uhd Jepsen, P. *Phys. Rev. B* **2001**, *64*, 094301.
(56) Mandal, P. K.; Chikan, V. *Nano Lett.* **2007**, *7*, 2521-2528.
(57) Pedersen, J. E.; Keiding, S. R. *IEEE J. Quant. Electron* **1992**, *28*, 2518-2522.
(58) Keiding, S. R. *J. Phys. Chem. A* **1997**, *101*, 5250-5254.
(59) Flanders, B. N.; Cheville, R. A.; Grischkowsky, D.; Scherer, N. F. *J. Phys. Chem.* **1996**, *100*, 11824-11835.
(60) Jimenez, R.; Fleming, G. R.; Kumar, P. V.; Maroncelli, M. *Nature* **1994**, *369*, 471-473.
(61) Maroncelli, M. *J. Phys. Chem.* **1991**, *94*, 2084-2103.
(62) Zielbauer, J.; Wegener, M. *Appl. Phys. Lett.* **1996**, *68*, 1223-1225.
(63) Němec, H.; Kadlec, F.; Kužel, P. *J. Phys. Chem.* **2002**, *117*, 8454-8466.
(64) Bonn, M. In *Conference on Lasers and Electro-Optics/International Quantum Electronics Conference*; Optical Society of America: Baltimore, Maryland, 2009, p CMT3.
(65) Ulbricht, R.; Hendry, E.; Shan, J.; Heinz, T. F.; Bonn, M. *Rev. Mod. Phys* **2011**, *83*, 543-586.
(66) Wang, F.; Shan, J.; Islam, M. A.; Herman, I. P.; Bonn, M.; Heinz, T. F. *Nat. Mater.* **2006**, *5*, 861.
(67) Beard, M. C.; Turner, G. M.; Schmuttenmaer, C. A. *J. Appl. Phys.* **2001**, *90*, 5915-5923.
(68) Yettapu, G. R.; Talukdar, D.; Sarkar, S.; Swarnkar, A.; Nag, A.; Ghosh, P.; Mandal, P. *Nano Lett.* **2016**, *16*, 4838-4848.
(69) Le Quere, C.; Raupach, M. R.; Canadell, J. G.; Marland, G.; et al. *Nature Geosci* **2009**, *2*, 831-836.

(70) Green, M. A.; Emery, K.; Hishikawa, Y.; Warta, W.; Dunlop, E. D. *Progress in Photovoltaics: Research and Applications* **2016**, *24*, 905-913.
(71) Ahn, N.; Son, D.-Y.; Jang, I.-H.; Kang, S. M.; Choi, M.; Park, N.-G. *J. Am. Chem. Soc* **2015**, *137*, 8696-8699.
(72) http://www.nrel.gov/ncpv/images/efficiency_chart.jpg, N. E. C.
(73) Kojima, A.; Teshima, K.; Shirai, Y.; Miyasaka, T. *J. Am. Chem. Soc* **2009**, *131*, 6050-6051.
(74) Stoumpos, C. C.; Kanatzidis, M. G. *Acc. Chem. Res* **2015**, *48*, 2791-2802.
(75) Stranks, S. D.; Eperon, G. E.; Grancini, G.; Menelaou, C.; Alcocer, M. J. P.; Leijtens, T.; Herz, L. M.; Petrozza, A.; Snaith, H. J. *Science* **2013**, *342*, 341-344.
(76) Gratzel, M. *Nat Mater* **2014**, *13*, 838-842.
(77) Stranks, S. D.; Snaith, H. J. *Nat Nano* **2015**, *10*, 391-402.
(78) Johnston, M. B.; Herz, L. M. *Acc. Chem. Res* **2016**, *49*, 146-154.
(79) Manser, J. S.; Saidaminov, M. I.; Christians, J. A.; Bakr, O. M.; Kamat, P. V. *Acc. Chem. Res* **2016**, *49*, 330-338.
(80) Eperon, G. E.; Paterno, G. M.; Sutton, R. J.; Zampetti, A.; Haghighirad, A. A.; Cacialli, F.; Snaith, H. J. *J. Mater.Chem. A* **2015**, *3*, 19688-19695.
(81) Kulbak, M.; Cahen, D.; Hodes, G. *J. Phys. Chem. Lett.* **2015**, *6*, 2452-2456.
(82) Moller, C. K. *Nature* **1958**, *182*, 1436-1436.
(83) Protesescu, L.; Yakunin, S.; Bodnarchuk, M. I.; Krieg, F.; Caputo, R.; Hendon, C. H.; Yang, R. X.; Walsh, A.; Kovalenko, M. V. *Nano Lett.* **2015**, *15*, 3692-3696.
(84) Manser, J. S.; Christians, J. A.; Kamat, P. V. *Chem. Rev.* **2016**, *116*, 12956-13008.
(85) Swarnkar, A.; Ravi, V. K.; Nag, A. *ACS Energy Lett.* **2017**, *2*, 1089-1098.
(86) Swarnkar, A.; Chulliyil, R.; Ravi, V. K.; Irfanullah, M.; Chowdhury, A.; Nag, A. *Angew. Chem. Int.* **2015**, *54*, 15424-15428.
(87) Xu, Y.-F.; Yang, M.-Z.; Chen, B.-X.; Wang, X.-D.; Chen, H.-Y.; Kuang, D.-B.; Su, C.-Y. *J. Am. Chem. Soc* **2017**, *139*, 5660-5663.
(88) Miyata, A.; Mitioglu, A.; Plochocka, P.; Portugall, O.; Wang, J. T.-W.; Stranks, S. D.; Snaith, H. J.; Nicholas, R. J. *Nat Phys* **2015**, *11*, 582-587.
(89) Mondal, N.; Samanta, A. *Nanoscale* **2017**, *9*, 1878-1885.
(90) Novoselov, K. S.; Geim, A. K.; Morozov, S. V.; Jiang, D.; Katsnelson, M. I.; Grigorieva, I. V.; Dubonos, S. V.; Firsov, A. A. *Nature* **2005**, *438*, 197-200.
(91) Zhang, Y.; Tan, Y.-W.; Stormer, H. L.; Kim, P. *Nature* **2005**, *438*, 201-204.
(92) Castro Neto, A. H.; Guinea, F.; Peres, N. M. R.; Novoselov, K. S.; Geim, A. K. *Rev. Mod. Phys* **2009**, *81*, 109-162.
(93) Kim, K. S.; Zhao, Y.; Jang, H.; Lee, S. Y.; Kim, J. M.; Kim, K. S.; Ahn, J.-H.; Kim, P.; Choi, J.-Y.; Hong, B. H. *Nature* **2009**, *457*, 706-710.
(94) Liu, M.; Yin, X.; Ulin-Avila, E.; Geng, B.; Zentgraf, T.; Ju, L.; Wang, F.; Zhang, X. *Nature* **2011**, *474*, 64-67.
(95) Shi, E.; Li, H.; Yang, L.; Zhang, L.; Li, Z.; Li, P.; Shang, Y.; Wu, S.; Li, X.; Wei, J.; Wang, K.; Zhu, H.; Wu, D.; Fang, Y.; Cao, A. *Nano Lett.* **2013**, *13*, 1776-1781.
(96) Miao, X.; Tongay, S.; Petterson, M. K.; Berke, K.; Rinzler, A. G.; Appleton, B. R.; Hebard, A. F. *Nano Lett.* **2012**, *12*, 2745-2750.
(97) Sun, Z.; Hasan, T.; Torrisi, F.; Popa, D.; Privitera, G.; Wang, F.; Bonaccorso, F.; Basko, D. M.; Ferrari, A. C. *ACS Nano* **2010**, *4*, 803-810.
(98) Xia, F.; Mueller, T.; Lin, Y.-m.; Valdes-Garcia, A.; Avouris, P. *Nat Nano* **2009**, *4*, 839-843.
(99) Gilje, S.; Han, S.; Wang, M.; Wang, K. L.; Kaner, R. B. *Nano Lett.* **2007**, *7*, 3394-3398.

(100) Gómez-Navarro, C.; Weitz, R. T.; Bittner, A. M.; Scolari, M.; Mews, A.; Burghard, M.; Kern, K. *Nano Lett.* **2007**, *7*, 3499-3503.

Chapter 2

Instrumentation and Data Analysis

In this chapter, the THz-TDS and TRTS setup, experimental procedures, data acquisition, and data analysis procedures are described. Ambient air is used for generation and detection of broadband THz. The objective of data analysis is to find out the optical constants, and photoconductivity of the different samples studied in this work.

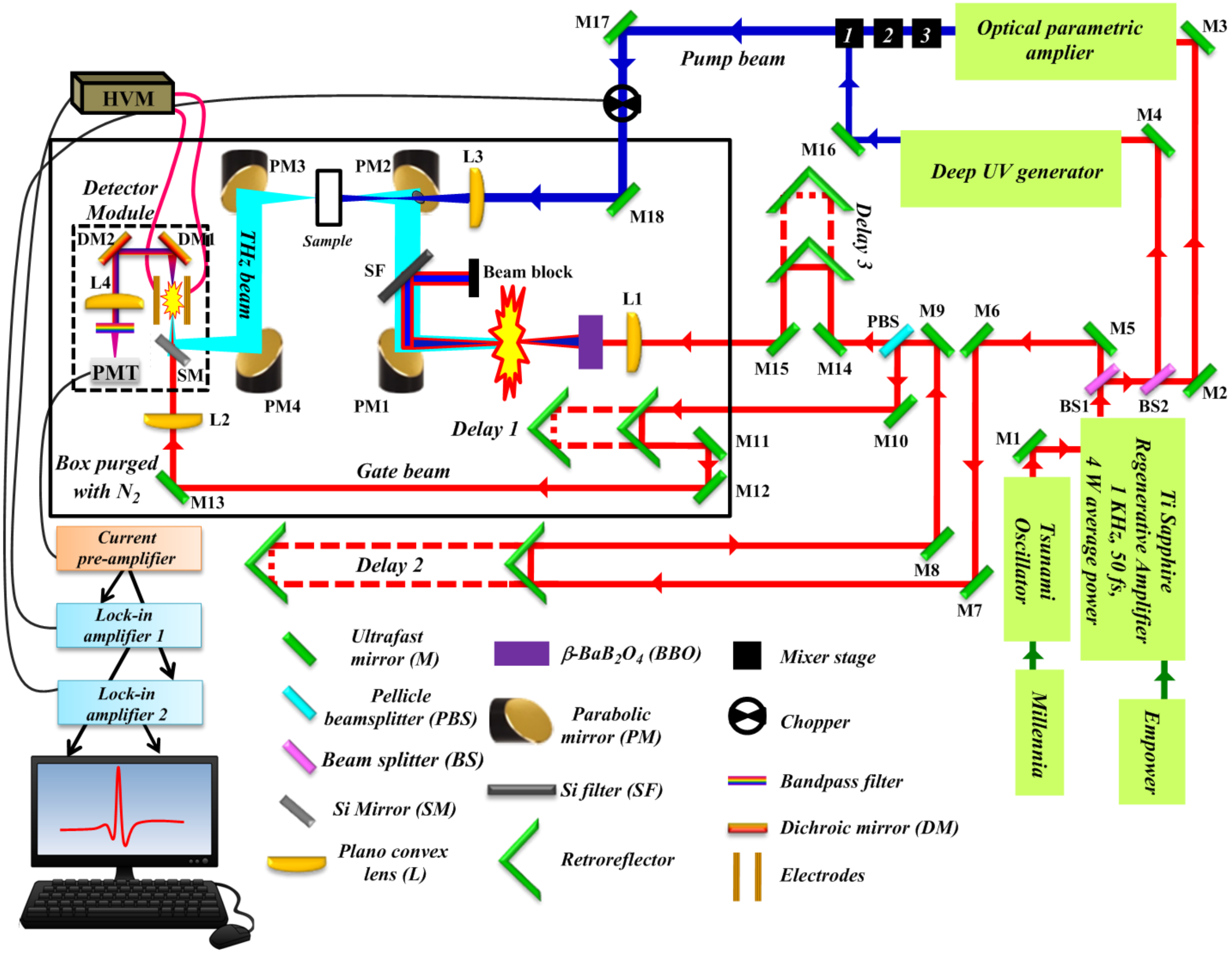

Figure 2.1. Schematic of time-resolved THz spectrometer

2.1 Description of the spectrometer

Figure 2.1 depicts the schematic of our time resolved THz setup. The optical source is a Ti-sapphire amplified laser (Spitfire Pro XP, Spectra Physics) seeded by an oscillator (Tsunami, Spectra Physics) that generates pulses with a central wavelength of 800 nm, 35 fs pulse duration (FWHM), 4 mJ of average pulse energy and 1 kHz repetition rate. The amplifier output is split using a 50:50 beam splitter (BS1 in Figure 2.1). Half of the average power is used for THz generation and detection. The remaining half is fed into an optical parametric amplifier (OPA) that produces pulses of tunable wavelengths in the range of 184 nm to 2600 nm. The output of the OPA is used as the pump pulse in our time-resolved THz experiments. The laser beam used for THz generation and detection is further split using a pellicle beam splitter (PBS; R:T = 8:92), where 8 % is reflected and 92% is transmitted. The transmitted beam is focused using a plano-convex lens (PL1) of focal length 125 mm into ambient air. A type I BBO crystal of 100 μm thickness is placed between the plano-convex lens and its focal point. The polarization and intensity of the 2ω can be varied by rotating the ordinary axis of the BBO crystal with respect to the incoming fundamental pulse polarization. The lens focuses both the ω and 2ω beams. Air plasma is generated at the focal point. The air plasma emits a wide range of electromagnetic radiations including intense, highly directional, broadband THz light. We use a high-resistivity silicon filter, SF (1 mm thick, 50% transmission) to block the ω, 2ω pulses and white light while transmitting THz radiation. The THz beam is collimated by the 1st off axis gold coated parabolic mirror (PM1) and focused onto the sample by the second parabolic mirror (PM2). The THz beam transmitted through the sample is recollimated and finally focused between two electrodes by another pair of parabolic mirrors. A mirror (SM) placed before the electrodes, reflects the converging THz beam between the two electrodes. The reflected beam from the beam splitter (PBS) acts as the near IR gate beam used for THz detection. The gate beam is reflected by a retroreflector mounted on a 50 mm stage (MTS50-Z8, Thorlabs) which is denoted as Delay 1 in Figure 2.1. The gate beam from the retroreflector is routed using several mirrors and passes through a hole drilled in the mirror SM placed just before the electrodes. The THz beam and the gate beam become collinear after mirror SM and focus at the same position between the electrodes. A high voltage modulator (HVM), synchronized with the laser repetition rate, supplies an AC bias of 1.5 kV to the electrodes. The HVM is modulated at 500 Hz which is half of the laser repetition rate (1 KHz). The THz field induces second harmonic (400 nm) of the gate beam (800 nm) in presence of the external bias which is directed into a photomultiplier tube (PMT) by two adjustable dichroic mirrors (DM1 and DM2). A lens is used to collimate the beam. A 400 nm bandpass filter with 10 nm bandwidth restricts any fundamental light from reaching the PMT. The gain voltage of the PMT is set between 100 mV and 400 mV. The current from PMT goes to the current preamplifier, which filters, amplifies, and converts the signal into a voltage signal. The voltage signal is then fed into the lock-in amplifier (SR830, Stanford Research Systems) locked to the frequency of the HVM. For THz detection, the spatial and temporal overlap of the THz and gate beam between the two electrodes is crucial. The second harmonic signal, which is proportional to the THz electric field, is recorded as the temporal overlap between the THz and the gate pulse is varied by moving the delay stage 1. Thus, the electric field of the THz waveform is mapped by the gate beam as a function of time. Fourier transformation of the time-domain signal is the complex THz spectrum. The generated THz radiation is detected using Zomega Air Photonics Detector Module (ZAP APD). The entire THz setup is enclosed in a transparent box and is under continuous dry nitrogen flow so that the relative humidity is maintained below 2 % within the box to avoid absorption of THz light by water vapour. While performing THz-TDS and TRTS experiments, we need to operate delay stages, acquire and save data from lock-in amplifiers and analyze the data to get optical parameters from them. The interface program was developed in LabVIEW (National Instruments). Using LabVIEW Virtual Instrument we have written computer programs that can do all the above-mentioned operations automatically.

2.2 THz & gate beam alignment

The THz and gate beam are horizontally polarized. Since THz is not visible to eyes, the optical beam used for THz generation is used for alignment. During alignment power of both the optical beam and the gate beam are reduced and only 10 mW power is sufficient for aligning the laser beams. Variable neutral density filter placed in the path of 2 mJ laser output used for THz generation and detection controls the laser power used for alignment. Inside the THz detector module, the spatial overlap of the gate and the THz beam is checked at the electrode position. For this purpose, the mirrors after the electrodes are removed and a card is placed there to view both the beams.

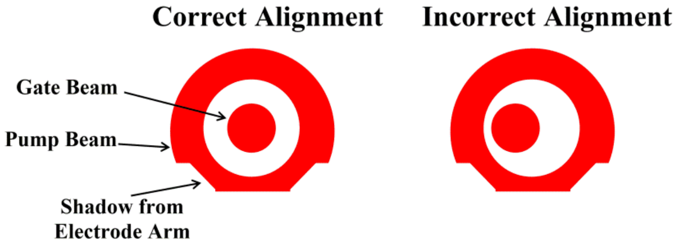

Figure 2.2. Pattern observed on card during correct and incorrect alignment of gate beam and beam used for THz generation

Figure 2.2 shows the pattern of both the beams falling on the card during correct and incorrect alignment. Optics outside the detector are adjusted to get the perfect alignment.

2.3 THz Generation and Detection from Ambient Air

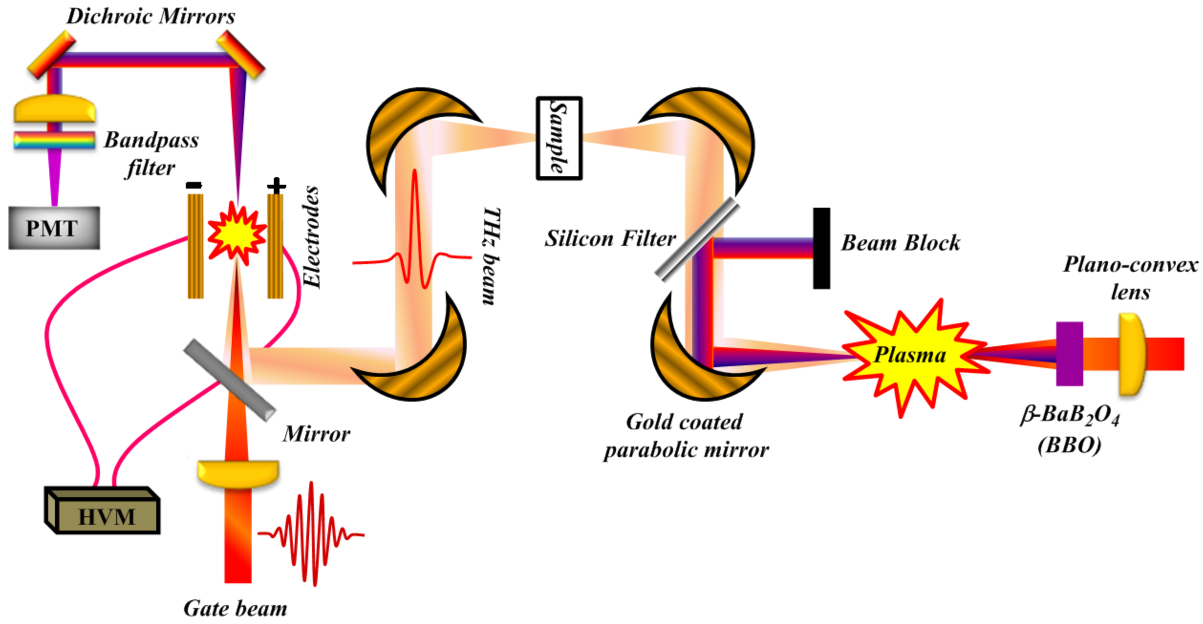

Figure 2.3. Schematic of setup for THz generation and detection from the air.

THz gas photonics has several advantages over other methods like using photoconductive antenna or electro-optic (EO) crystals for THz generation and detection. The THz bandwidth is only limited by the optical pulse duration and gap free bandwidth till 20 THz can be realized for 80 fs pulse using gas photonics[1] which is the primary advantage compared to other methods. Furthermore, the broad bandwidth accomplished using air based generation and detection is not blighted by phonon absorption, phase matching limitations, dispersions and damage threshold. There are reports of achieving ultra-broad bandwidth exceeding 100 THz, using sub 20 fs optical pulse.[2] Using air also enables remote generation of THz by creating THz near the target.[3] The second harmonic beam is locally produced and then co-propagated with the fundamental in free space where they focus and mix at a distance to produce THz radiation. This approach prevents THz waves from getting absorbed by atmospheric water vapour and facilitates remote THz sensing and imaging. Finally, data analysis becomes simpler using air photonics since with EO generation and detection surfaces create reflection echoes in time domain waveform. In our laboratory, we have setup THz spectrometer based on air photonics.

2.3.1 THz Generation

THz wave generation from the air was first reported by Hamster *et al.* where they focused intense laser beam (peak power ~ 1 TW) into the air.[4] At the focal point, the air molecules get ionized and in presence of the ponderomotive potential of the intense laser field the ions and electrons get separated that gives rise to a resultant dipole with the emission of THz radiation.[4,5] However, the efficiency of THz generation using single wavelength was less. Later, Cook *et al.* came up with the idea of mixing the fundamental wave with its second harmonic, and focusing them in the air indeed produced intense THz radiation.[6] They also proposed the mechanism for THz generation from the air. The role of air plasma in THz generation was further studied by Roskos and co-workers.[7] Zhang and coworkers conducted a more systematic study by separately monitoring effect of polarization, phase, and amplitude of fundamental and second harmonic beams in THz generation.[8]

According to four-wave mixing (FWM) model,[6] THz generation is a third order nonlinear process involving mixing of four waves, $\Omega_{THz,}$ 2ω, - ω, - ω. The frequencies of the three input beams (2ω, - ω, - ω) add to nearly zero ($\Omega_{THz,}$ THz frequency).

$$\Omega_{THz} = (2\omega + \Omega_{THz} - \omega - \omega) \quad (1)$$

In presence of pulsed laser, the envelope of the input fields give rise to the nonlinear response and the output rectified wave is the THz wave. According to four wave mixing, the THz field has the form:

$$E_{THz}(t) \propto \chi^{(3)} \mathrm{E}^{2\omega}(\mathrm{t}) \mathrm{E}^{*}_{\omega}(\mathrm{t}) \mathrm{E}^{*}_{\omega}(\mathrm{t}) \cos(\varphi) \quad (2)$$

$$E_{THz}(t) \propto \chi^{(3)} \sqrt{\mathrm{I}_{2\omega}} \mathrm{I}_{\omega}(\mathrm{t}) \cos\varphi \quad (3)$$

However, this model predicts a significantly lower THz field strength than that was observed experimentally. The origin of third order nonlinearity ($\chi^{(3)}$,) is also ambiguous. To answer the incongruity of FWM mechanism, Kim, *et al*. proposed the asymmetric transient current (ATC) model.[9,10] According to the ATC model, intense laser field causes suppression of the coulomb barrier leading to tunnel ionization of electrons from the atoms or the molecules of gases present in the air. Thus, THz radiation is emitted from a non-diminishing transverse photocurrent via Maxwell's equations.

In the presence of fundamental and second harmonic beam where the laser field symmetry is perturbed, asymmetric current results in THz emission. The two-colour field is given by,

$$E_{2C} = E_{\omega}(t)\cos(\omega t) + E_{2\omega}(t)\cos(2\omega t + \phi) \quad (4)$$

When the laser intensity at the focal point is > 1 x 10^{14} W/cm^2, the tunneling ionization becomes dominant. Ionization rate gives the electron density, from which electron current can be calculated according to the equation, $J(t) = \sum_i e\, N_e(t) v_i(t)$ where e is the charge of an electron and $v(t)$ is the electron velocity acquired in presence of two colour field. The electric field of the generated THz radiation is proportional to the time varying current, $E_{THz} \propto \frac{dJ}{dt}$.

Andreeva *et al.* in a very recent study on ultra-broadband THz generation from air plasma have solved the enduring debate on the mechanism of THz generation from two color air filament.[11] They demonstrated that both nonionized molecules which they referred to as neutrals and plasma contribute to THz generation.[11] They further illustrated that neutrals contribute via four wave mixing to higher frequency THz generation while plasma contributes to the intense low frequency THz generation.

2.3.2 THz Detection

Coherent THz detection allows determination of both amplitude and phase of the spectral component making up the THz pulses. The THz detection using photoconductive (PC) antenna is limited by carrier lifetime of the semiconductor substrate of which the PC is made of. Also, the transverse optical phonon absorption in PC antenna and EO crystals and phase mismatch in EO crystals restrict the THz bandwidth that can be detected using these popular techniques (PC antenna and EO sampling) of coherent THz detection. Ambient air has been successfully utilized to generate broadband THz, and third order nonlinear process contributes to it. THz wave detection can also be realized by the reciprocal process of third order optical nonlinearity responsible for THz generation. In the year 2006, broadband detection of THz using air was reported for the first time.[6] The THz field induces second harmonic (SH) generation of the gate beam and is detected by measuring this SH signal at plasma point. The terahertz field induced second harmonic (TFISH) generation can be explained using the following equation:[12]

$$E_{2\omega}^{THz} \propto \chi^{(3)} E_{\omega} E_{\omega} E_{THz} \quad (5)$$

where $\chi^{(3)}$ is the third order non-linear susceptibility, $E_{2\omega}^{THz}$, E_{ω} and E_{THz} are the electric field amplitude of the 2ω, ω, and THz waves respectively. Since $E_{2\omega}^{THz} \propto E_{THz}$, the intensity is related to $I_{2\omega}^{THz} \propto I_{THz}$ and is not phase sensitive i.e. the measurement is incoherent. One possible way of overcoming this problem is to use highly intense gate beam. An intense gate pulse allows SHG within the plasma, which can mix with the 2ω produced due to TFISH, enabling quasi-coherent THz detection. But this technique demands very intense gate beam and strong THz field. This technique can be upgraded by introducing a local oscillator at the plasma point that makes heterodyne phase sensitive THz detection possible. The local oscillator can be introduced in the form of a high voltage ac bias through a pair of electrodes at the plasma point. This heterodyne technique is known as the air biased coherent detection (ABCD), and perturbative four wave mixing can precisely describe the detection mechanism.[12] Including the local oscillator, the second harmonic electric field is given by,

$$E_{2\omega} \propto \chi^{(3)} E_{\omega} E_{\omega} (E_{2\omega}^{THz} + E_{2\omega}^{LO}) \qquad (6)$$

and the second harmonic intensity has the form,

$$I_{2\omega} \propto (E_{2\omega})^2 \propto \left(\chi^{(3)}\right)^2 I_{\omega}^2 \left((E_{2\omega}^{THz})^2 + 2E_{2\omega}^{THz} E_{2\omega}^{LO} cos\phi + (E_{2\omega}^{LO})^2\right) \qquad (7)$$

where ELO is the electric field supplied by the electrodes and φ is the phase difference between the $E_{2\omega}^{THz}$ and $E_{2\omega}^{LO}$. The above equation can be written as

$$(E_{2\omega})^2 = \left(\chi^{(3)} I_{\omega}\right)^2 I_{THz} + 2\,\chi^{(3)} I_{\omega} E_{2\omega}^{LO} E_{THz} \cos\varphi + (E_{2\omega}^{LO})^2 \qquad (8)$$

The first term in above equation is proportional to the intensity of the THz wave. The second term, which is a cross correlation term between $E_{2\omega}^{LO}$ and $E_{2\omega}^{THz}$, is proportional to E_{THz}. This term is the key component for coherent THz detection. The third term in the equation 8 is the dc contribution from LO, and is eliminated by using a lock-in amplifier locked to the modulating frequency of the ac bias. Local oscillator significantly enhances the detection sensitivity. Hence, even a low gate beam intensity (that may be insufficient for producing plasma) is adequate for ABCD. Also, using ABCD, ultra-broad THz bandwidth can be accomplished. In our spectrometer, we have achieved a spectral bandwidth of 15 THz. Left panel in figure 2.4 shows time domain THz waveform we obtain from our spectrometer and right side shows the frequency domain amplitude obtained by Fourier transformation of the time domain waveform.

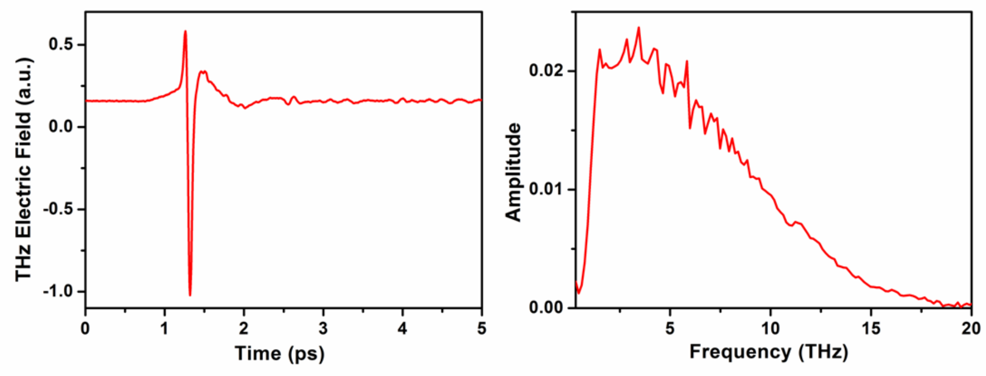

Figure 2.4. THz time domain waveform and frequency domain amplitude as obtained from our spectrometer.

2.4 Time-Domain THz Spectroscopy (THz-TDS)

In THz-TDS we measure the THz light absorbed by a sample in the non-photoexcited state. It is like any other steady state absorption spectroscopy in the sense that in both cases the attenuated light after absorption by the sample is recorded. But a crucial difference is that in THz-TDS we directly measure the THz electric field, and not just the intensity, from which we can calculate the amplitude and phase of the spectral components making up the THz pulse. We conducted THz-TDS in transmission mode where the sample to be studied was placed at the focal point of PB2 and PB3 (Figure 2.1). First, we measure THz transmission through the empty sample cell that gives E_{ref}. Then we place the sample and record the transmission data, which gives E_{sam}. The ratio of Fourier transformation of the E_{sam} to E_{ref} gives the power transmittance and relative phase.

2.5 Time-Resolved THz Spectroscopy (TRTS)

An optical parametric amplifier (TOPAS C) is used to generate the pump beam required for exciting the sample in time resolved THz experiments. Optional frequency mixers designated as mixer 1, 2 and 3 are used at the TOPAS-C output to extend the tuning range into visible, ultra violet and/or infrared. As per requirement of the sample, the pump wavelength can be altered using a dedicated software package WinTOPAS.

The delay between the THz probe pulse and the optical pump pulse can be tuned by scanning the 300 mm delay stage (PI-M413) denoted as Delay 2 in Figure 2.1.

The pump power is manipulated using a variable neutral density filter, placed in the pump path. A chopper rotating at a frequency of 333 Hz is used to chop the pump beam. The pump beam is made to pass through a hole drilled in the parabolic mirror so that it becomes collinear with the THz probe beam. The pump beam diameter is usually kept three times the diameter of the probe beam to ensure uniform probing of excited sample. Knife-edge technique is utilized to measure the diameter of the pump and the probe beam. During TRTS, a black polyethylene sheet is placed between the third and fourth parabolic mirror that blocks the transmitted and scattered pump light from reaching the PMT but is transparent to the THz light.

2.6 Knife-edge measurement of beam diameter

Knife-edge technique for beam diameter measurement is a very popular and simple technique. The total power of the beam is recorded as the knife is translated through the beam using a calibrated translation stage. The power meter records the power when the beam is fully exposed till when the knife completely blocks the beam.

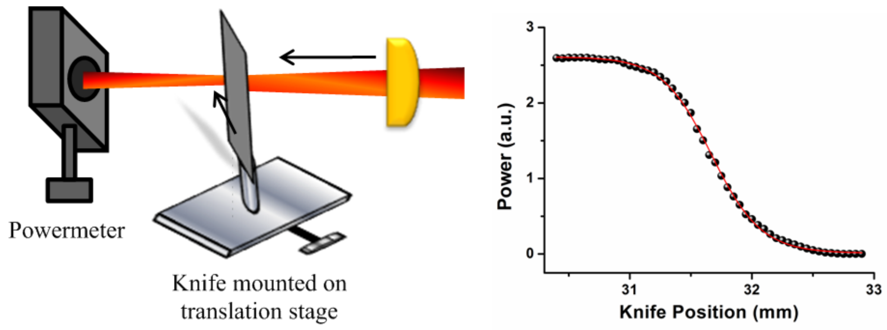

Figure 2.5. Schematic of knife-edge experimental setup and a typical curve obtained during beam diameter measurement.

By fitting the data using the following equation beam diameter can be measured:

$$P = P_0 + \frac{P_{max}}{2}\left(1 - \operatorname{erf}\left(\frac{\sqrt{2}(x - x_0)}{w}\right)\right) \qquad (9)$$

Where P_0 is a background power, P_{max} is the maximum power, x_0 is the stage position at half of maximum power, and erf is a standard error function and w is the beam radius.

2.7 Double Lock-in Technique

TRTS is carried out using a double lock-in technique[13] which allows simultaneous detection of the pump induced change in THz transmission ($-\Delta E(t_p)$) and the corresponding THz transmission through the non-photoexcited NCs ($E_0(t_p)$).[5] Two lock-in amplifiers are used. The first lock-in amplifier is referenced to the frequency of the local oscillator (modulation frequency of the ac bias) that modulates the THz probe beam at 500 Hz. The other lock-in amplifier is locked to the chopper frequency of 333 Hz that modulates the pump beam. The output from the current preamplifier is split and separately sent to the lock-in amplifiers. To minimise the crosstalk between the signals measured by each lock-in amplifier, harmonic and subharmonic of the two modulating frequencies are deliberately avoided. So, the probe and pump beam are modulated at 500 and 333 Hz, respectively.

2.8 Different Types of Scans

In TRTS we collect data in two ways.[14] In one case, the Delay 1 (Figure 2.1) is kept fixed at a position which corresponds to the maximum of the time-domain THz waveform and the Delay 2 (300 mm stage, Figure 2.1) is scanned. Scanning delay 2 varies the delay between optical pump and THz probe. The pump induced change in the THz peak amplitude $\Delta E(t_{max}, t_p)$ is recorded. Overall, we get an average response of the sample over the experimental temporal window. This is commonly referred to as frequency averaged TRTS.[15]

The second method is to scan the entire THz probe waveform by moving the delay 1 or delay 3 (50 mm stage, Figure 2.1) at several fixed pump probe delay. Here we record the pump induced change in THz waveform $\Delta E(t, t_p)$, at a fixed pump probe delay (t_p). This is known as the frequency resolved TRTS.

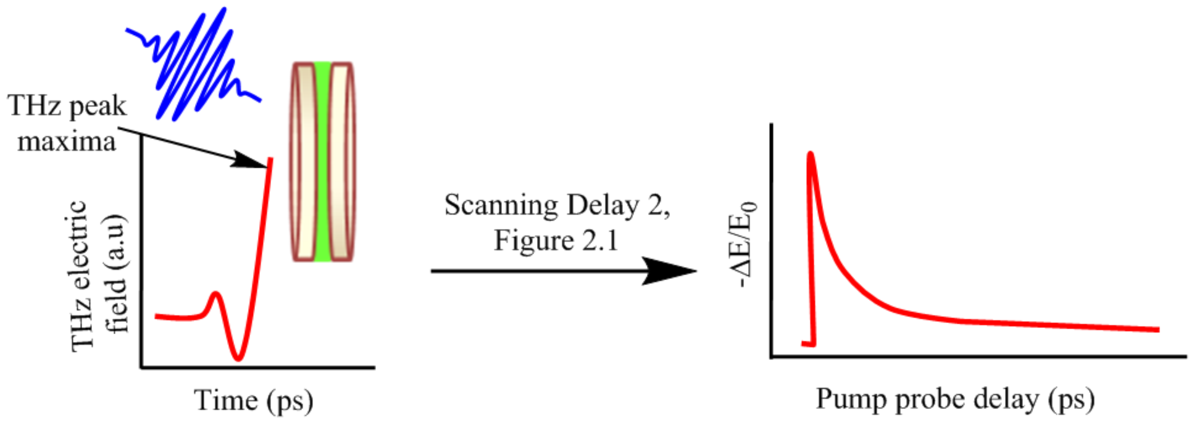

Figure 2.6. Schematic showing the temporal evolution of pump induced change in THz peak amplitude on scanning delay stage 2 (Figure 2.1).

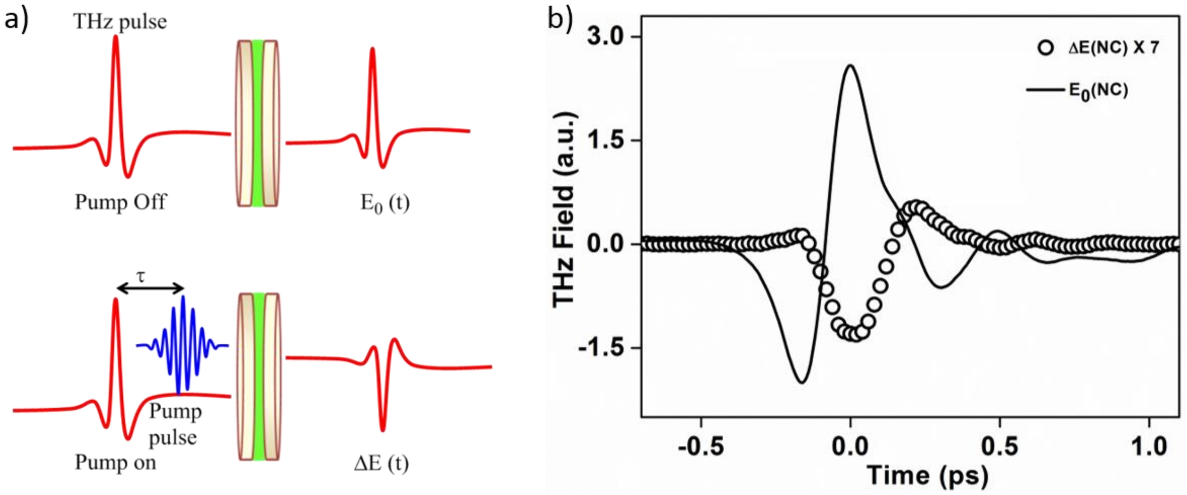

Figure 2.7. a) Schematic showing pump induced change in THz waveform (ΔE(t)). b) Typical THz waveforms in TRTS measurements. E_0 is the pump-off signal plotted in black solid line. Pump induced change of THz field is plotted as ΔE (black empty circles).

2.9 Sample Cells for liquid samples

Figure 2.8. A typical sample cell for liquid samples where the sample is injected between the two windows separated by a spacer.

All THz experiments described in this thesis were carried out in transmission mode. Liquid samples were injected in a demountable liquid cell procured from Harrick Scientific Products, DLC-M25. For THz-TDS experiments of alcohols, high resistivity silicon was used as windows. Polytetrafluoroethylene (PTFE) spacers of different thickness were used to vary the sample path length. For TRTS measurements of colloidal $CsPbBr_3$ nanocrystals and its complexes dispersed in heptamethylnonane (HMN), TPX windows separated by a 950 μm Teflon spacer were used. Windows can be of different materials; common are silicon, TPX, and HDPE windows. For measurements of solid samples, thin films of the samples were cast on high-density polyethylene (HDPE) substrate.

2.10 Data Analysis

THz-TDS allows a simple determination of both phase and amplitude. The complex refractive index of a material can be computed from complex transmittance, from which we solve for other optical constants.

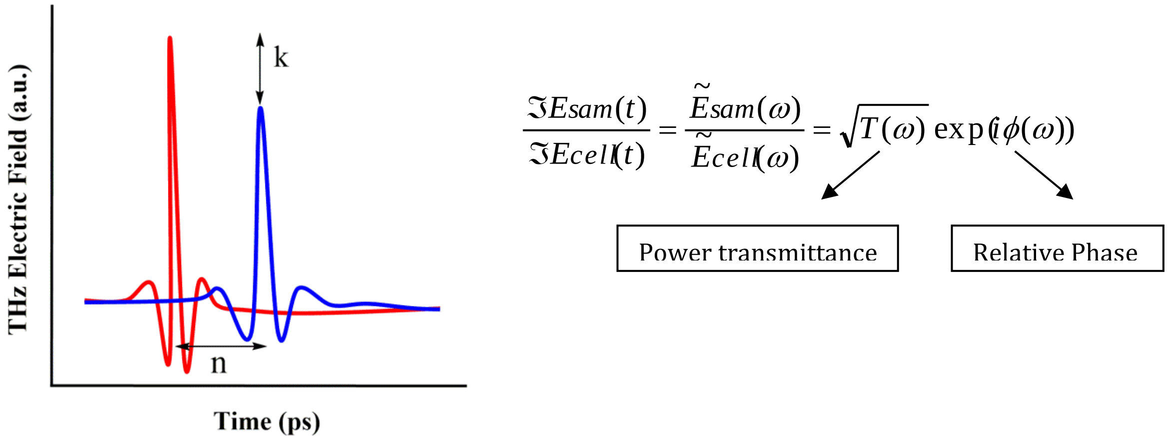

Figure 2.9. Reference (red) and sample (blue) THz waveforms showing the effect of constant n(ω) and k(ω).

Further, using k (extinction coefficient) and n (refractive index), other optical constants can be evaluated according to the following equations:

$$\textit{Absorption coefficient}, \alpha = \frac{2\omega k}{c} \qquad (10)$$

$$\textit{Refractive index}, n = 1 + \frac{c}{2\pi\omega d}(\phi - \phi_0) \qquad (11)$$

$$\textit{Complex dielectric function}, \hat{\varepsilon}(\omega) = \hat{n}^2 = (n + ik)^2 = n^2 - k^2 + i2nk \qquad (12)$$

$$\textit{Complex refractiveindex}, \hat{n} = n + ik \qquad (13)$$

$$\textit{Complex conductivity}, \hat{\sigma} = -i\omega\varepsilon_0\hat{\varepsilon} \qquad (14)$$

By taking the ratio of complex Fourier transformation of $E_{sam}(t)$ and $E_{cell}(t)$, the complex refractive index of the sample can be obtained as,

$$\frac{fE_{sam}(t)}{fE_{cell}(t)} = \frac{\tilde{E}_{sam}(\omega)}{\tilde{E}_{cell}(\omega)} = \sqrt{T(\omega)}\exp\big(i\varphi(\omega)\big) \quad (15)$$

where $T(\omega)$is the power transmittance and $\varphi(\omega)$ is the relative phase.

The Fresnel reflection and transmission losses were considered while extracting the complex refractive index $\big(\tilde{n}(\omega) = n_{re}(\omega) + in_{im}(\omega)\big)$ from $T(\omega)$ and $\varphi(\omega)$ using an iterative method following Nashima *et al.*[16] Windowing functions were used prior to complex Fourier transformation. For a better frequency resolution of the measurements it is better to take longer scan in time domain. But if only the main transmitted pulse is considered i.e. the scan is taken only till that point so that any reflection is avoided, the spectral resolution becomes worse.

2.10.1 Time-resolved Data

The pump induced change in complex photoconductivity ($\Delta\hat{\sigma}$) of liquid samples placed between the two windows, under the condition that $\Delta n \ll 1$, is given by, [17]

$$\Delta\hat{\sigma}(\omega) = -2i\omega\varepsilon_0 n_2 \Delta\hat{n}(\omega) \qquad (16)$$

where n_2 is the refractive index of the non-photoexcited sample and $\Delta\hat{n}$ is given by,

$$\Delta\hat{n} = \left[\frac{i\omega l}{c} - \frac{n_2 - n_1}{n_2(n_2+n_1)} + MR\right]^{-1} \frac{\Delta E(\omega)}{E(\omega)} \qquad (17)$$

where MR stands for multiple reflections. Here, l is the path length of the sample, n_1 is the refractive index of the window, n_2 is the refractive index of the sample, MR is multiple reflection term and $\Delta E(\omega)$, $E(\omega)$ are the Fourier transforms of the time-domain traces of the pump-induced and pump-off transmitted THz electric fields, respectively.

The pump induced change in the complex dielectric function of NCs solution can be obtained from the pump induced change in complex conductivity:

$$\Delta\hat{\varepsilon}(\omega) = i\Delta\hat{\sigma}(\omega)/\omega\varepsilon_0 \qquad (18)$$

The effective dielectric constant of the photoexcited NCs (${\hat{\varepsilon}_{eff}}^{pe}$) can be calculated from the effective dielectric constant of the non photoexcited NCs (${\hat{\varepsilon}_{eff}}^{np}$) and pump induced change in dielectric constant of NCs solution ($\Delta\hat{\varepsilon}$) using the following equation:

$${\hat{\varepsilon}_{eff}}^{np} + \Delta\hat{\varepsilon} = {\hat{\varepsilon}_{eff}}^{pe} \qquad (19)$$

After calculating ${\hat{\varepsilon}_{eff}}^{pe}$ using equation 19 and using this value in equation 20 (effective medium approach)[18], the intrinsic dielectric constant of the photoexcited NCs can be calculated (${\varepsilon_i}^{pe}$). The simple effective medium approach has the following equation:

$$\varepsilon_{eff}(\nu) = \mathrm{f}\,\varepsilon_i(\nu) + (1-\mathrm{f})\,\varepsilon_{\hbar}(\nu) \qquad (20)$$

where $\varepsilon_{eff}(\nu)$, $\varepsilon_i(\nu)$ and $\varepsilon_h(\nu)$ are the complex dielectric functions of the composite (NC solution, experimentally determined from THz-TDS), the inclusion (NCs) and the host medium (solvent) respectively; and f is the volume fraction of the NCs in the solution. The difference between ${\varepsilon_i}^{pe}$ and ${\varepsilon_i}^{np}$ (intrinsic dielectric constant of the non-photoexcited NCs) is given by,

$$\Delta{\hat{\varepsilon}_i}^{pe} = {\hat{\varepsilon}_i}^{pe} - {\hat{\varepsilon}_i}^{np} \tag{21}$$

which is the pump induced dielectric constant of NCs. Again, by incorporating the value of $\Delta{\hat{\varepsilon}_i}^{pe}$, the pump induced conductivity ($\Delta\sigma_{ind}$) of NCs can be calculated from eq. 18.

2.10.2 Thin film approximation

For TRTS analysis of samples cast on HDPE substrate, we used thin film approximation.[19] Generally, this approximation is used when the thickness of the film is so thin that a THz pulse passing through the film acquires a phase shift much smaller than the typical wavelength i.e., $n_f(\omega/c)\, d_f <<1$ where n_f is the refractive index and d_f is the thickness of thin film. Also, the sample is optically much denser compared to the substrate ($n_f >> n_s >1$). The complex transmittance is given by the equation:[20]

$$T^*(\omega) = |T(\omega)|e^{i\varphi(\omega)} = \frac{1+n_s}{1+n_s+Z_0\sigma^*(\omega)d_f} \tag{22}$$

where Z_0 = 376.7Ω is the impedance of free space. Experimentally we obtain $T^*(\omega)$. From the above equation complex conductivity (σ*) can be analytically solved:

$$\sigma^*(\omega) = \frac{1+n_s}{Z_0 d}\left(\frac{cos\varphi(\omega)}{|T(\omega)|} - 1 - i\frac{sin\varphi(\omega)}{|T(\omega)|}\right) \tag{23}$$

We also need to fit the experimentally observed complex dielectric functions and complex conductivity spectra to a suitable physical model to extract more insightful parameters. The details of the fitting procedures required have been discussed in the individual chapters.

2.11 References

(1) Ho, I. C.; Guo, X.; Zhang, X. C. *Opt. Express* **2010**, *18*, 2872-2883.
(2) Thomson, M. D.; Blank, V.; Roskos, H. G. *Opt. Express* **2010**, *18*, 23173-23182.
(3) Wang, T. J.; Daigle, J. F.; Yuan, S.; Théberge, F.; Châteauneuf, M.; Dubois, J.; Roy, G.; Zeng, H.; Chin, S. L. *Phys. Rev. A* **2011**, *83*, 053801.

(4) Hamster, H.; Sullivan, A.; Gordon, S.; White, W.; Falcone, R. W. *Phys. Rev. Lett.* **1993**, *71*, 2725-2728.
(5)Hamster, H.; Sullivan, A.; Gordon, S.; Falcone, R. W. *Phys. Rev. E* **1994**, *49*, 671-677.
(6) Cook, D. J.; Hochstrasser, R. M. *Opt. Letters* **2000**, *25*, 1210-1212.
(7) Kress, M.; Löffler, T.; Eden, S.; Thomson, M.; Roskos, H. G. *Opt. Letters* **2004**, *29*, 1120-1122.
(8) Xie, X.; Dai, J.; Zhang, X. C. *Phys. Rev. Lett.* **2006**, *96*, 075005.
(9) Kim, K. Y.; Glownia, J. H.; Taylor, A. J.; Rodriguez, G. *Opt. Express* **2007**, *15*, 4577-4584.
(10) Kim, K. Y.; Taylor, A. J.; Glownia, J. H.; RodriguezG *Nat Photon* **2008**, *2*, 605-609.
(11) Andreeva, V. A.; Kosareva, O. G.; Panov, N. A.; Shipilo, D. E.; Solyankin, P. M.; Esaulkov, M. N.; González de Alaiza Martínez, P.; Shkurinov, A. P.; Makarov, V. A.; Bergé, L.; Chin, S. L. *Phys. Rev. Lett.* **2016**, *116*, 063902.
(12) Dai, J.; Xie, X.; Zhang, X. C. *Phys. Rev. Lett.* **2006**, *97*, 103903.
(13) Iwaszczuk, K.; Cooke, D. G.; Fujiwara, M.; Hashimoto, H.; Jepsen, P. U. *Opt. Express* **2009**, *17*, 21969-21976.
(14) Beard, M. C.; Turner, G. M.; Schmuttenmaer, C. A. *Phys. Rev B* **2000**, *62*, 15764-15777.
(15) Schmuttenmaer, C. A. *Chemical Reviews* **2004**, *104*, 1759-1780.
(16) Nashima, S.; Morikawa, O.; Takata, K.; Hangyo, M. *J. Appl. Phys.* **2001**, *90*, 837-842.
(17) Knoesel, E.; Bonn, M.; Shan, J.; Wang, F.; Heinz, T. F. *J. Chem. Phys.* **2004**, *121*, 394-404.
(18) Mandal, P. K.; Chikan, V. *Nano Lett* **2007**, *7*, 2521-2528.
(19) A.C.S. Van Heel (Ed.), *Advanced Optical Techniques*, North-Holland, Amsterdam, **1967**, 268
(20) Nuss, M. C.; Mankiewich, P. M.; O'Malley, M. L.; Westerwick, E. H.; Littlewood, P. B. *Phys. Rev. Lett.* **1991**, *66*, 3305-3308.

Chapter 3

Broadband Terahertz-Dielectric Spectroscopy of Alcohols

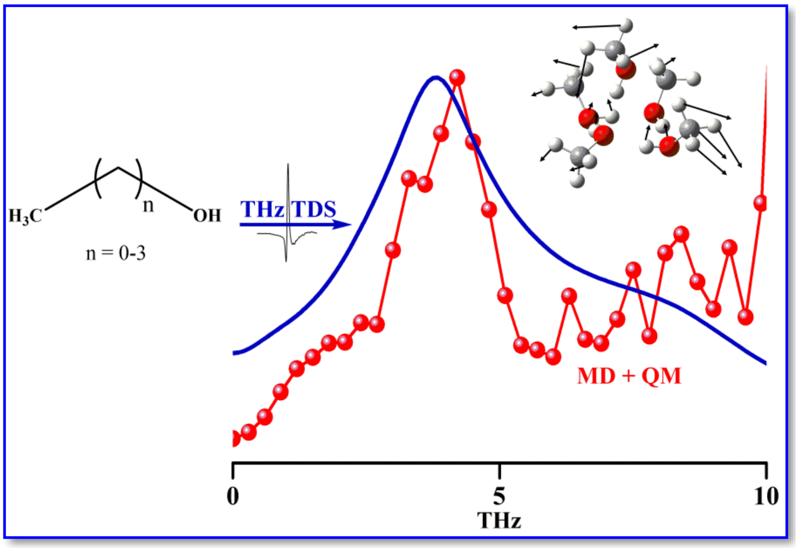

3.1 Introduction

Alcohols are an interesting class of H-bonded liquids that contain both hydrophilic groups and hydrophobic “tails”. Alcohols can donate only one hydrogen bond but can accept two[3,4] and thus they lack the extensive H-bond network that is present in water. A change in the size and shape of the hydrophobic part can alter the hydrophobic interactions and may also affect the H-bond network. Moreover, alcohols are miscible with myriads of polar and non-polar solvents. Studies on the molecular structure of liquid alcohols using X-ray scattering, MD simulations, etc. reveal that alcohol molecules associate to form ring or chain like structure.[5-8] However, the degree of association is still debatable and the relation between the structure and dynamics is not well understood. NMR relaxation experiments suggest that with increasing alkyl chain length the rotational correlation time of the OH group slows down from methanol (~5 ps) to 1-hexanol (~ 90 ps).[9] Using OH stretching mode as an indicator; polarization sensitive pump-probe and 2D IR spectroscopy have been recently employed to understand H-bond dynamics in alcohols.[10] The study reveals that OH dynamics predominantly has two time scales; a fast component (~100 fs) assigned to librations and H-bond stretching, common for both water and alcohols, and a slower component (a few picoseconds) arising from the diffusion-dictated H-bond exchange dynamics present only in alcohols. In another recent study, Using polarization resolved fs-IR spectroscopy Hunger *et al.* demonstrated that the OD stretch vibration is faster in methanol (~ 0.75 ps) as compared to ethanol (~0.9 ps) and its higher homologues.[11]

Dielectric spectroscopy provides further insights into the reorientation dynamics of the alcohols.[12-16] This method records the response of polar molecules to an applied oscillating electric field in the form of dielectric loss and dispersion functions which result from the reorientation of molecular dipoles. Thus, the frequency dependent complex permittivity, $\epsilon(\nu) = \epsilon^{'}(\nu) - i\epsilon^{''}(\nu)$, can be measured. This, in turn, provides the relaxation time (τ_j) and dispersion amplitudes $\left(\Delta\epsilon_j\right)$ of the fundamental relaxation processes. Alcohols show three distinct relaxation dynamics in the timescales of one to hundreds of picoseconds depending on the size of the alcohol molecule: a) a slow relaxation process originating from the alignment of dipoles in the H-bonded network, b) an intermediate relaxation process stemming from the reorientation of alcohol monomers, and c) a very fast process related to the flipping or rotation of the free OH group or breaking and reformation of H-bond in a translational motion.[17-19]

At Terahertz (THz) (1 THz = 33.33 cm^{-1} = 4 meV) frequency range (0.1 to 15 THz), the molecular reorientation and several intermolecular vibrations (local oscillations of dipoles) may coexist contributing to the overall liquid dynamics. Nevertheless, dielectric properties in THz frequency regime remained unexplored for a long time since this region of the electromagnetic spectrum could not be accessed until recently.[20,21] Time-domain THz spectroscopy (THz TDS) technique measures the electric field, rather than intensity, and thus provides both the amplitude and phase of the spectral components making up the THz pulse. Absorption coefficient and the refractive index of the sample can be calculated from the amplitude and phase. This allows for the evaluation of the complex-valued permittivity of the sample without involving Kramers-Kronig analysis.[21]

Kindt and Schmuttenmaer initiated the study of dielectric properties of methanol, ethanol, 1-propanol utilizing THz-TDS in the narrow frequency range of 0.06-1.0 THz.[22] They found a good agreement between their data and multiple relaxation models up to 1 THz. At higher frequencies, there is an onset of oscillatory motions, which cannot be fitted using relaxation models. Kindt *et al.,* however, did not observe the onset of resonant absorption till 1 THz, necessitating the measurement of dielectric properties at higher frequencies. Fukasawa *et al.* analyzed the complex dielectric and Raman spectra of H-bond liquids from microwave to THz frequency range combining microwave and far infrared (FIR) techniques.[23] Their study reveals that the dielectric spectrum for methanol deviates from the relaxation model at frequencies above $\nu \sim 290$ GHz. Three Debye relaxation processes (τ_1 = 51.8 ps, τ_2 = 8.04 ps, and τ_3 = 0.89 ps) combined with two damped oscillators with peaks at ~55 and 125 cm^{-1} reproduced the dielectric spectrum of methanol within 50 MHz to 5 THz frequency range.[23] Yomogida*et al.* studied temperature dependent complex permittivity of 14 monohydric alcohols in the frequency range of 0.2-2.5 THz. According to their study, the complex permittivity of the alcohols has contribution from three parts: the high frequency part of the dielectric relaxation, a broad vibrational mode around 1.2 THz, and a low frequency tail of another high frequency oscillatory motion located above 2.5 THz.[24,25] However, the precise nature of this high frequency mode and its effect to the dynamics could not be ascertained since the study was limited to 2.5 THz.

In the present study, broadband THz-TDS (0.5-10 THz) has been utilized to study the dielectric properties of methanol, ethanol, 1-propanol, 2-propanol, and 1-butanol. We have also performed all-atom molecular dynamics (MD) simulations and *ab initio* quantum calculations of the alcohols to gain the molecular level understanding of the vibrational modes responsible for the observed absorption pattern in the THz region.

3.2 Methods and Materials

3.2.1 Terahertz time domain spectroscopy (THz-TDS)

Generation of THz pulsed waves from air plasma and detection using air-biased coherent detection (ABCD) technique has been elaborately discussed in Chapter 2.[26-28] The spectral bandwidth detected in our laboratory is often more than 15 THz. In spite of the broad THz range offered by our spectrometer, the frequency range for the present study is confined to 0.5-10 THz since the amplitude of THz field drops below 1/e of the maximum amplitude at frequencies below 0.5 THz. Besides, beyond 10 THz, there is considerable absorption by the alcohols making the transmission very poor. For recording THz transmission data of alcohols, we used two high resistivity silicon windows (2 mm thickness, 1-inch diameter) separated by polytetrafluoroethylene (PTFE) spacer and the sample cell was placed at the focal point of two parabolic mirrors. First, the THz field transmitted through an empty cell was recorded as the reference signal ($E_{cell}(t)$). Next, THz signal transmitted through the sample cell filled with alcohol was measured ($E_{sam}(t)$). To obtain a satisfactory signal-to-noise (S/N) ratio, an average of several measurements (normally 30-50) was carried out. The shape, amplitude, and the phase of $E_{sam}(t)$ differ from $E_{cell}(t)$ due to the reflection, absorption, and dispersion of THz light by the sample. Exact Blackman windowing function was applied to the time domain signal prior to the Fourier transformation. By taking the ratio of complex Fourier transformation of $E_{sam}(t)$ and $E_{cell}(t)$, the complex refractive index of the sample can be obtained as,

$$\frac{fE_{sam}(t)}{fE_{cell}(t)} = \frac{\tilde{E}_{sam}(\omega)}{\tilde{E}_{cell}(\omega)} = \sqrt{T(\omega)}\exp\big(i\varphi(\omega)\big) \qquad (1)$$

where $T(\omega)$is the power transmittance and $\varphi(\omega)$ is the relative phase. The Fresnel reflection and transmission losses were considered while extracting the complex refractive index $\big(\tilde{n}(\omega) = n_{re}(\omega) + in_{im}(\omega)\big)$ from $T(\omega)$ and $\varphi(\omega)$ using an iterative method following Nashima *et al.*[29] An average spectrum for each alcohol was obtained from measurements using three different path lengths (100, 150, and 250 μm) at the room temperature.

3.2.2 Materials

The alcohols studied in this work are methanol, ethanol, 1-propanol, 2-propanol, and 1-butanol. Methanol and 1–butanol (purity 99.8 %) were purchased from Sigma Aldrich. Ethanol (purity ≥ 99.9 %) was purchased from Merck. 1-propanol and 2-propanol (HPLC grade, 99.8 % purity) were procured from Rankem. All alcohol samples were used without further purification.

3.2.3 Computational Study

A computational study was carried out by Debasis Saha working under the supervision of Dr. Arnab Mukherjee.

Both classical and quantum approaches were used to understand the interactions amongst alcohol molecules within the THz frequency range in molecular detail. Classical molecular dynamics simulations were used to generate vibrational density of states (VDOSs) and normal modes. Quantum calculations were also performed to compare the modes at different frequencies obtained from classical simulations and to calculate H-bond strengths of alcohols. Details of the method are provided below.

(i) Molecular Dynamics (MD) Simulation

MD simulations were performed using OPLS (Optimized Potential for Liquid Simulations) force field for all systems (methanol, ethanol, 1-propanol, 2-propanol, and 1-butanol).[30] For each system, a cubic box was created and was filled with alcohol molecules for simulation. The simulations were carried out by employing periodic boundary condition in all directions to mimic the effect of the bulk. The numbers of molecules taken in the simulations were: 631 for methanol, 501 for ethanol, 501 for 1-propanol, 465 for 2-propanol and 424 for butanol. Each system was energy minimized using steepest descent[31], followed by heating up to 300 K using Berendsen thermostat[32] with a coupling constant of 0.2 ps. This was followed by an equilibration run for 5 ns at constant temperature (300 K) and 1 bar pressure using Nosé-Hoover thermostat[33,34] and Parrinello-Rahmanbarostat[35], respectively, with a coupling constant of 0.2 ps for each. Particle Mesh Ewald (PME) method [36] with 10 Å cut-off was used for electrostatic interactions. Experimental compressibility[37] was used to achieve the correct density. A cut-off of 10 Å was used for the van der Waals interactions. All the simulations were carried out using GROMACS[38] software package.

(ii) Vibrational density of states (VDOS) calculation

VDOS was calculated from both the velocity autocorrelation function (VACF) and normal mode analyses (NMA). In the first approach, VDOS was calculated from the Fourier transformation of the velocity autocorrelation function (VACF) of all the atoms of the system defined as,

$$I(\omega) = \frac{1}{k_B T} \sum_j m_j \left[\frac{1}{2\pi} \int_{-\infty}^{\infty} \exp(-i\omega t) \langle \boldsymbol{v}_j(0) . \boldsymbol{v}_j(t) \rangle dt \right] \qquad (2)$$

where $\boldsymbol{v}_j(t)$ is the velocity of the j^{th} atom at time t. To calculate the VACF, the equilibrated structure was simulated for 1 ns under the same conditions as the equilibration run and the frames were saved at every 5 fs. An initial 500 ps long trajectory was sufficient to get a smooth VACF profile. For the calculation of VDOS using normal mode analysis, 10 frames were extracted from the 1 ns trajectory at 100 ps intervals and the Hessian matrix was generated for every frame. Diagonalization of the Hessian matrix provided the normal modes (vibrational spectrum) of different frequencies. The final vibrational spectrum was obtained from the average of 10 different vibrational spectra for each alcohol system. Both the VACF calculation and the normal mode analyses were carried out using GROMACS[38] software package. The modes at the frequency range obtained from fitting of the experimental data were plotted using Gaussview software[39].

(iii) Ab-initio Calculations

Random configurations consisting of four or five alcohol molecules were collected from MD simulations and were optimized using density functional theory (DFT) with B3LYP functional[40] and 6-31G(d,p) basis set. B3LYP functional was used because it shows a good agreement with experimental frequencies for several systems reported by Czarnecki *et al.*[41] However, a smaller basis set was used here to reduce computational cost. Frequency calculations were performed on the optimized configurations to obtain the vibrational spectrum. Twenty configurations were used to obtain an average spectrum for each system. Similar approach has been used before for ion-water systems [42,43]Moreover, H-bonding strength of different alcohols was evaluated by calculating the quantum mechanical energy as a function of H-bond distance between the oxygen and hydrogen atoms of a H-bonding pair using Second-order Møller–Plesset (MP2) method with aug-cc-pVDZ[44] basis set. All quantum calculations were performed using Gaussian09 software package.[45]

3.3 Results and Discussion:

3.3.1 THz-TDS: The time domain and Fourier transformed frequency domain data of the empty sample cell, and that filled with alcohols are shown in Figure 3.1a and 3.1b, respectively.

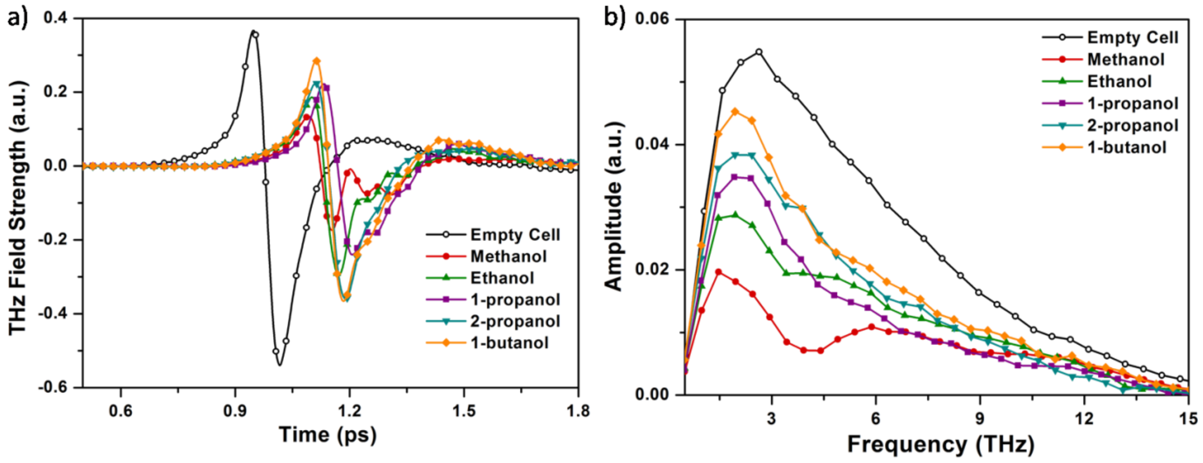

Figure 3.1. a) Time domain THz waveforms and corresponding b) frequency domain amplitude spectra of the empty sample cell and cells filled with methanol and 1-butanol (path length 150 μm).

From the frequency domain data, we have extracted the frequency dependent absorptions and refractive indices (Figures 3.2a and 3.2b). The errors associated with the refractive index values of the alcohols studied are given in Table 3.1. In all cases, the error is between 2-6 %.

The absorption spectrum of methanol (Fig. 3.2 a) shows a prominent absorption peak at ~3.8 THz (~ 127 cm^{-1}) and a broad peak at ~ 8 THz (~ 266 cm^{-1}). These two absorption features are clearly visible in case of ethanol as well. However, for all other alcohols studied here the absorption feature at about 4-5 THz is visible, and seems to have shifted towards a higher frequency with the increasing number of carbon atoms in the alcohol molecule. Note that, methanol has a strikingly higher absorbance compared to other alcohols almost throughout the entire frequency range.

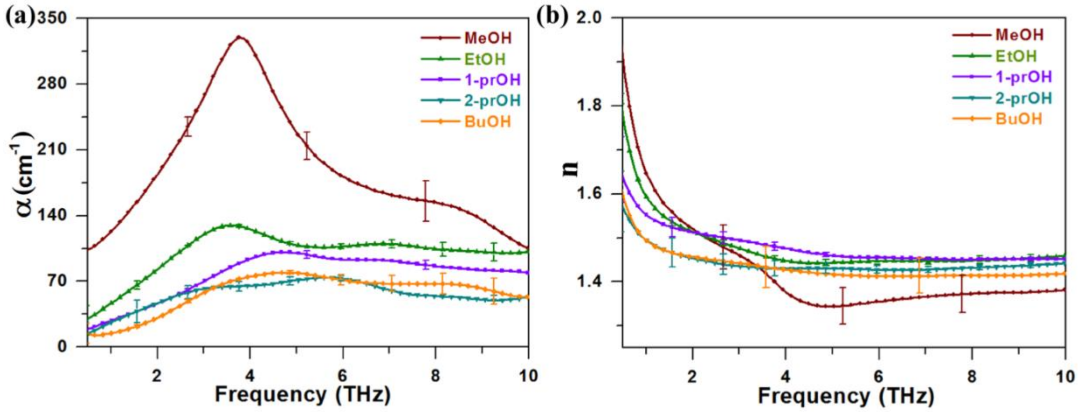

Figure 3.2. Frequency dependent a) absorption and b) real refractive indices of alcohols. Error bars for some selected frequency only are shown to preserve clarity. Note that, the errors are large at the extremes of the frequency range.

Table 3.1. Percentage error in refractive index, real and imaginary dielectric function values calculated by the root mean square deviation method from three set of data collected using 100 μm, 150 μm, and 250 μm spacers.

Alcohols	% Error		
	Refractive Index (n)	Real dielectric function (ε’)	Imaginary dielectric function (ε”)
Methanol	3.11	6.27	14.2
Ethanol	2.26	4.5	9.3
1-propanol	5.25	10.7	10.3
2-propanol	3.21	6.49	6.87
1-butanol	2.58	5.19	14.8

The absorbance decreases in alcohols with increasing alkyl chain length. It is interesting to note that the absorption spectra of 1-propanol and 2-propanol are quite different even though the numbers of carbon atoms are same in both molecules. This probably indicates that 2-propanol having a branched hydrophobic part exhibits different structure and dynamics than its isomer 1-propanol.

However, the absorption and refractive index data can only provide the information on the optical properties of the medium. A better insight into the liquid dynamics can be obtained from the frequency dependent complex dielectric function as defined below.

$$\hat{\epsilon}(\omega) = \epsilon^{'}(\omega) - i\epsilon^{''}(\omega) \quad (3)$$

The complex dielectric constant and the complex refractive index are related as,

$$\hat{n}(\nu) = n(\nu) - ik(\nu) \quad (4)$$

$$\epsilon^{'}(\omega) = n^2(\omega) - k^2(\omega) \quad (5)$$

$$\epsilon^{''}(\omega) = 2n(\omega)k(\omega) \quad (6)$$

Where $\omega = 2\pi\nu$ and $k(\omega) = \frac{\lambda\alpha(\omega)}{4\pi} = \frac{c\alpha(\omega)}{2\omega}$. α is the absorption coefficient, λ is the wavelength, and c is the speed of light in vacuum. Figures 3.3 a) and 3.3 b) respectively show the frequency dependent real and imaginary components of the dielectric function of different alcohols. The error in evaluating the real and imaginary dielectric function values using three spacer sizes is 4-10% and 6-15%, respectively. Details are provided in Table 3.2 and 3.3. The errors in our measurements are mainly due to the uncertainty in the sample path length, and are similar to that reported by Kindt *et al.*[10] The real and imaginary values of dielectric function obtained here are in good agreement (within error bars) with the previous literature reports in the common frequency range (0.5-2.5 THz). [23-25]An inflection point at ~4 THz is observed in the dielectric dispersion of methanol (Fig. 3.3a). Corresponding to this there is a peak in the dielectric loss spectrum (Fig. 3.3b).

To understand various relaxation processes contributing to the dielectric spectra of the alcohols, we tried fitting the dielectric dispersion and dielectric loss spectra using a Debye relaxation model. According to this model, the complex permittivity is given by,

$$\hat{\epsilon}(\omega) = \epsilon_\infty + \sum_{j=1}^{n} \frac{\epsilon_j - \epsilon_{j+1}}{1 + i\omega\tau_j} \quad (7)$$

where ω is the angular frequency, ϵ_1 is the static dielectric constant, ϵ_j's are the strengths of dielectric relaxation processes, ϵ_∞ is the dielectric constant at high frequency, n is the number of relaxation processes, and τ_j's are the relaxation times.

However, the Debye relaxation model, even with the inclusion of multiple relaxation times, failed to provide an acceptable fit (determined by χ^2 and correlation coefficient value) to the experimental data.

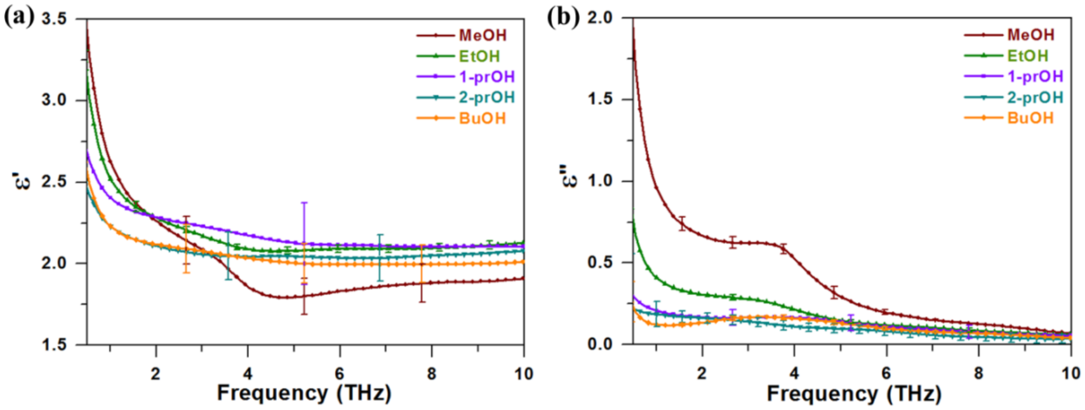

Figure 3.3. Frequency dependent a) real and b) imaginary dielectric spectra of alcohols.

As mentioned above, lower frequency limit of our experimental data in this study is 0.5 THz which is much higher than the frequency for which Debye relaxation models were used in earlier reports.[18,19] Furthermore, Fukasawa *et al.* reported that at frequencies ~290 GHz, there is a significant discrepancy between the experimental dielectric spectrum of methanol and its fit to the Debye model.[23] Therefore, only Debye relaxation may not be an appropriate model to describe the dielectric function of alcohols beyond 0.5 THz. At higher THz frequencies, resonant or oscillatory motions of a molecule or a group of molecules come into play[22]. Such motions are apparent in the absorptions that are associated with inflection points in the refractive index graph. In such cases, Debye relaxation model may become inadequate; instead damped harmonic oscillator model has to be used to understand the oscillatory motions of the molecules. Accordingly, we attempted fitting the dielectric spectra using different models that are combinations of Debye relaxation and damped harmonic oscillator models. The complex dielectric spectrum in oscillator model is given by,

$$\hat{\epsilon}(\omega) = \sum_{i=1}^{n} \frac{A_i}{\omega_i^2 - \omega^2 - i\omega\gamma_i} \quad (8)$$

where A_i is the amplitude of the oscillatory motion, ω_i is the angular frequency, and γ_i is the damping coefficient. Among all combinations attempted, only the model with single Debye and three oscillators could simultaneously fit the experimentally observed real and imaginary dielectric functions. The χ^2 values of the fits were less than 0.001 and correlation coefficient values were very close to 1 (Table 3.4.B), ensuring good fit to the experimental data. Figure 3.4 shows the experimental real and imaginary dielectric functions of the alcohols and their fits to single Debye and triple oscillator model. The complex equation combining single Debye and three damped harmonic oscillator model is given by,

$$\hat{\epsilon}(\omega) = \epsilon_\infty + \frac{\Delta\epsilon}{1 + i\omega\tau} + \frac{A_1}{\omega_1^2 - \omega^2 - i\omega\gamma_1} + \frac{A_2}{\omega_2^2 - \omega^2 - i\omega\gamma_2} + \frac{A_3}{\omega_3^2 - \omega^2 - i\omega\gamma_3} \quad (9)$$

Table 3.2. Debye and oscillator model parameters by fitting experimental dielectric loss spectra to Single Debye and triple damped oscillator model.

Alcohols	τ (ps)	ω_1 (THz)	ω_2 (THz)	ω_3 (THz)
Methanol	0.78 (0.03)	0.94 (.07)	3.68 (0.05)	7.9 (0.2)
Ethanol	0.82 (0.03)	1.9 (0.7)	3.82 (0.09)	9.54 (2.1)
1-propanol	1.10 (0.01)	1.87 (0.05)	4.38 (0.02)	9.5 (1.1)
2-propanol	2.01 (0.22)	1.9 (0.2)	5.09 (0.14)	13.5 (0.5)
1-butanol	1.12 (0.06)	2.4 (0.9)	4.9 (0.35)	15.6 (2.2)

Table 3.2 lists the relaxation time and oscillator frequencies obtained by fitting the experimental dielectric functions to equation 8. There is a relaxation process occurring at the time scale of 0.7- 2 ps for all alcohols studied. The timescales we obtain by fitting the dielectric function of alcohols are also very similar to the timescale of rupture and reformation of individual H-bonds in alcohols and water reported earlier.[46-49] Hence, we assign the Debye relaxation process contributing to our broad band THz data to the H-bond breaking and reforming dynamics. The other parameters like amplitude of oscillatory motions (A_i), damping coefficient (γ_i) and dielectric constant at high frequency (ε_0) are listed in Table 3.3.

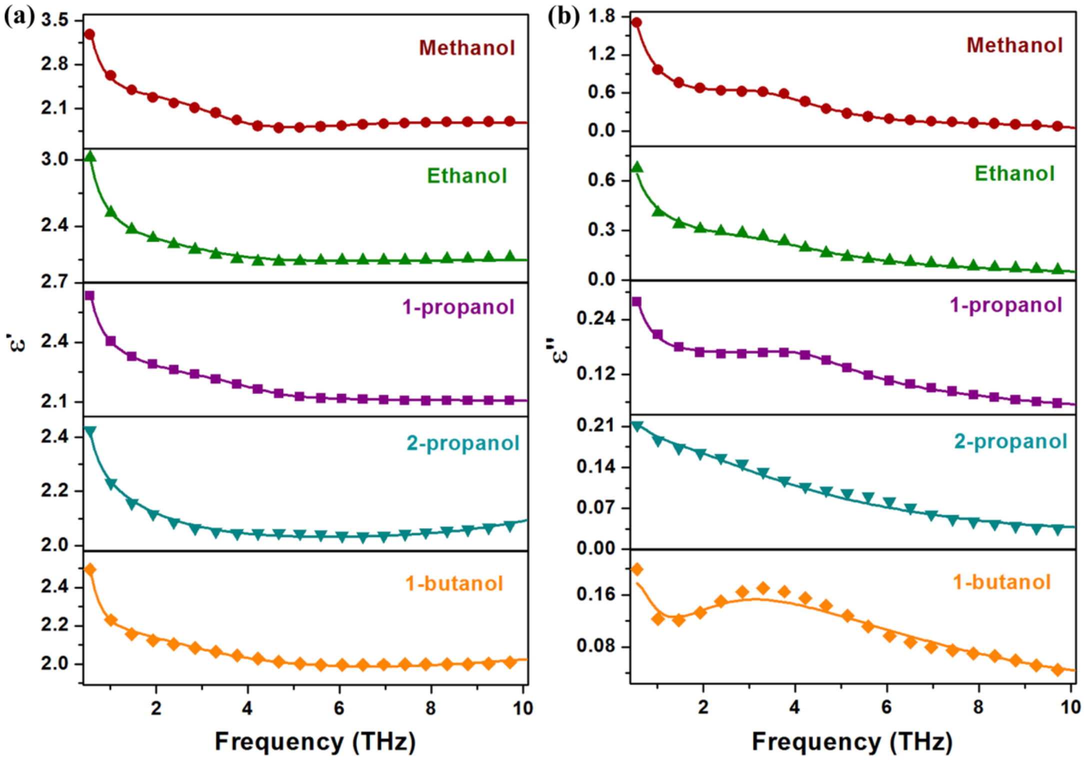

Figure 3.4 Experimental dielectric functions (symbols) of the alcohols and their fits (solid lines) to Debye-oscillator combined model (equation 8). a) portray the real (ε') and b) the imaginary (ε") components of the dielectric functions.

We obtain three peaks from fitting the experimental dielectrics for all the alcohols studied here. The first peak is at a low frequency of 1-2 THz. A major peak for all the alcohols is found in 4-6 THz range. The third peak is obtained at a frequency above 8 THz. The frequency range of our study is limited to 10 THz. Therefore, the reliability associated with the high-frequency peaks obtained from the fits is expected to be less.

Figure 3.5 shows the contributions of the Debye relaxation and the three oscillators to the experimentally observed dielectric loss spectrum for methanol. To understand the origin of these peaks, we have used computational methods to identify the modes corresponding to different frequencies.

Table 3.3. Debye and oscillator model parameters by fitting experimental dielectric loss spectra to Single Debye and triple damped oscillator model.

Sample	ε_0	$A_1/(2\pi)^2$ [THz^2]	$\gamma_1/2\pi$ [THz]	$A_2/(2\pi)^2$ [THz^2]	$\gamma_2/2\pi$ [THz]	$A_3/(2\pi)^2$ [THz^2]	$\gamma_3/2\pi$ [THz]	χ^2	Correlation Coefficient
Methanol	2.03 (.002)	8.86 (.6)	5.9 (.3)	5.5 (.1)	3.66 (.07)	3.08 (.4)	5.01 (0.5)	3.41e-4	0.9995
Ethanol	2.12 (.003)	25.1 (3.8)	32.2 (11.5)	1.45 (.2)	4.3 (.4)	23.7 (9.6)	88.4 (14.6)	2.14e-4	0.9997
1-propanol	2.1 (.002)	13.6 (0)	28.8 (0.2)	0.63 (.06)	3.05 (0.16)	15.9 (3.8)	35.7 (8.5)	3.02e-6	0.9999
2-propanol	1.98 (.003)	7 (1.2)	23.9 (3.2)	3.87 (0.3)	12.43 (0.6)	8.2 (0.3)	0.3 (0.13)	4.41e-5	0.9999
1-butanol	1.92 (.01)	9.73 (1.9)	31.5 (4.3)	5.5 (0.5)	9.8 (0.8)	12.1 (0.9)	2.5 (0.5)	1.12e-4	0.9998

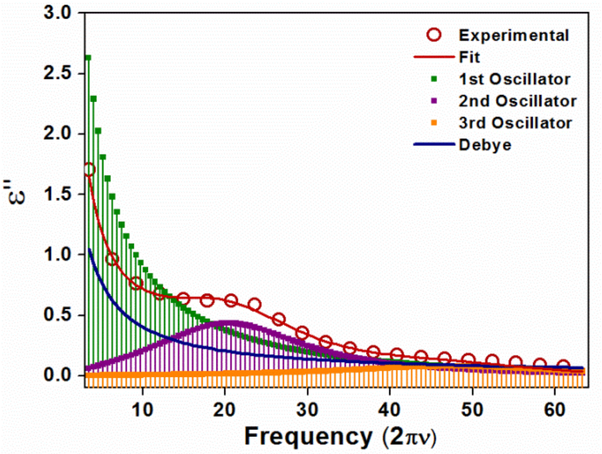

Figure 3.5. Contributions of Debye relaxation and three oscillators to the experimentally observed dielectric loss spectrum for methanol.

3.3.2 Vibrational spectra from classical simulation: Classical simulations enable us to obtain the vibrational spectra for the entire system at a finite temperature using velocity autocorrelation function (VACF). The vibrational spectra calculated using VACF is shown in Figure 3.6a. To compare with experimental results, only the relevant frequency range (1-10 THz) of the spectra is shown. This region of the spectrum primarily involves intermolecular interactions among different molecules.

As observed from the experimental values, here also we find a peak below 2 THz frequency region. However, the broad peak observed at the low-frequency region is known to correspond to intermolecular collision modes, as seen for other systems.[50] Similar to experiment, methanol shows a peak close to 4 THz not seen for other alcohols for which several different peaks are observed in the region above 6 THz. Almost all the alcohols show a peak around 1 THz. The spectral feature within 2 to 6 THz region is similar. Note that, however, the VDOS calculated using VACF, as shown above, involves all Raman and IR active modes whereas the experimental data presented here have contribution only from IR active modes.

To visualize the atomistic motions at a given frequency, we performed normal mode analyses (NMA) of the system collected at 100 ps interval from the simulation and plotted in Figure 3.6b. Vibrational spectra from NMA are similar for all the alcohols. Although the spectral features are similar, it does not show any peak for methanol at 4 THz or at a higher frequency for other alcohols. The difference between both approaches may be the reason for this discrepancy. While VACF has dynamical information at a finite temperature and therefore represent the quasi-harmonic modes, NMA represents the result based on a given local minimum with harmonic approximation.

NMA reveals that the modes at around 2 THz for different alcohols correspond to the collective motions of the whole molecule as shown in Figure 3.7. Woods *et al.* also observed an absorption band around 30 cm^{-1} (0.9 THz) in their FIR spectroscopic study of liquid methanol.[51] However, they assigned the 30 cm^{-1} band to the intermolecular bending.

The other major peak in the experiment was found at around 4-6 THz region. Modes at this frequency range correspond to the vibration of the alkyl groups with smaller movements of OH groups. These motions for the alcohols studied in this work are shown in Figure 3.8. Note here that, in our analysis, we find the movements of the H-atoms more predominant compared to the motions of the heavier atoms. However, from the magnitude of these movements, as shown by the different sized arrows in Figure 3.8, we determine the motions of the atoms responsible for peaks at different frequency ranges.

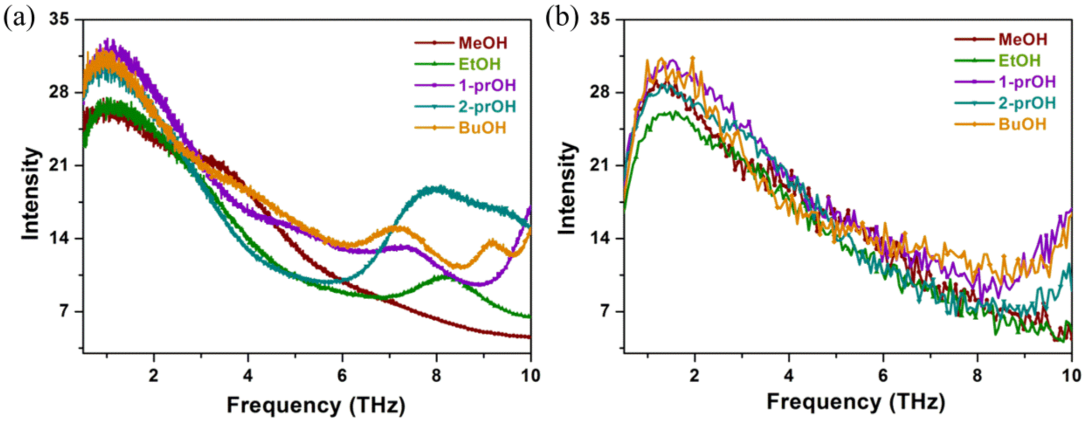

Figure 3.6.a) A specific THz region of the spectra of different alcohols generated using VACF. b) Spectra obtained from normal mode analyses of different alcohols.

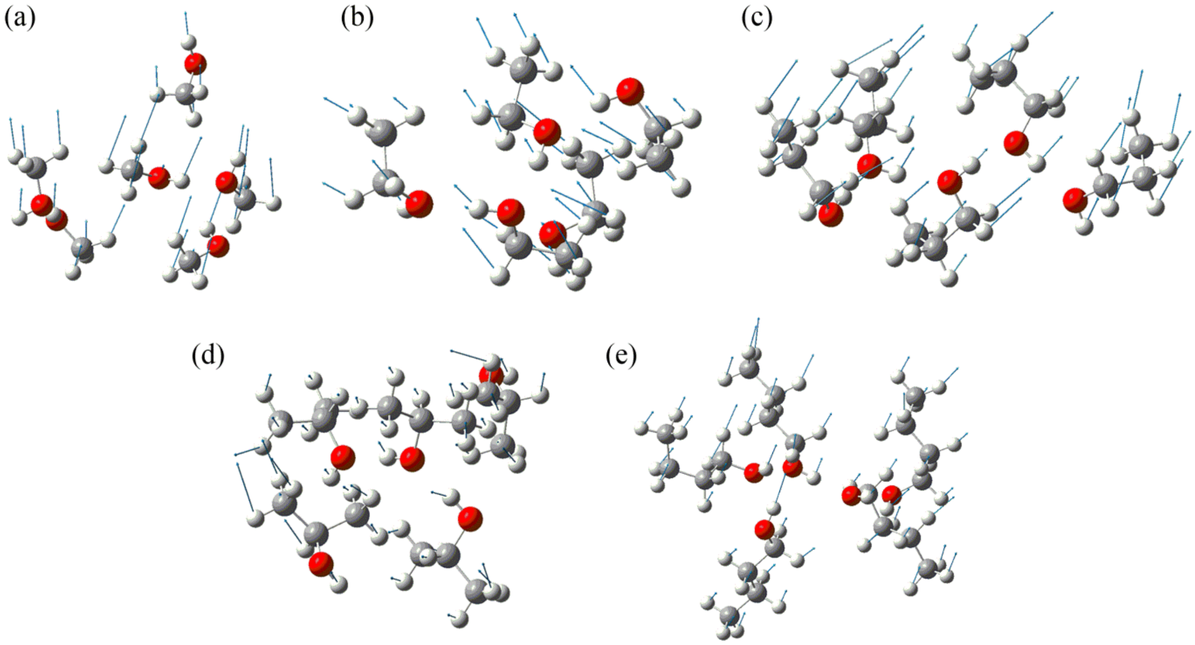

Figure 3.7. The motions of the alcohol molecules below 2 THz region for methanol (a), ethanol (b), 1-propanol (c), 2-propanol (d) and 1-butanol (e). The arrows here indicate the motion of the atoms. The same direction of the arrows for a particular molecule indicates the overall motion of the whole molecule in that direction in this range of frequency.

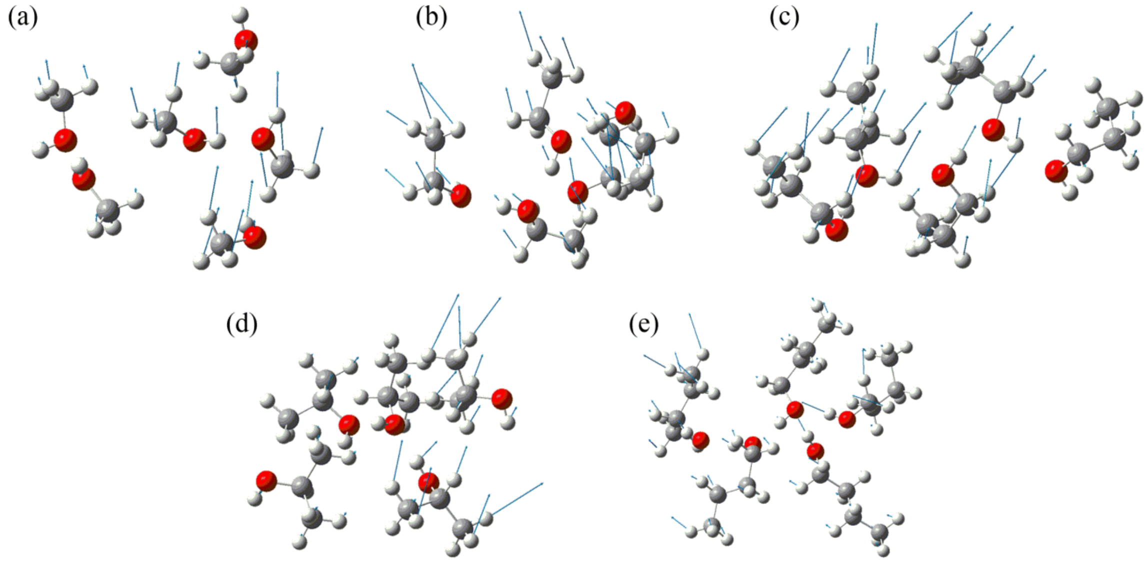

Figure 3.8. The modes of the alcohol molecules around 4-6 THz region for methanol (a), ethanol (b), 1-propanol (c), 2-propanol (d) and 1-butanol (e) using normal mode analyses. The arrows here indicate the movements of atoms in different directions. The larger arrows on H-atoms of the alkyl chains indicate larger movements of these compared to the hydroxyl hydrogen atoms.

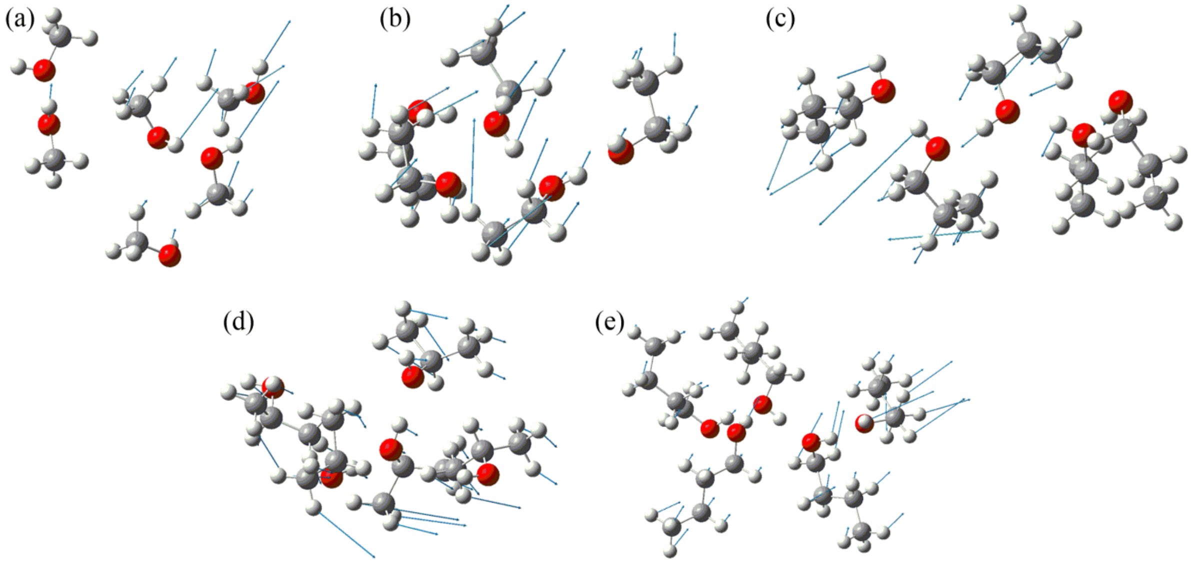

Figure 3.9. The motions of the alcohol molecules above 8 THz region for methanol (a), ethanol (b), 1-propanol (c), 2-propanol (d), and 1-butanol (e). The arrows on different atoms indicate the motions of the atoms. Visualization of these motions show movements of the atoms involved in H-bonding with different molecules.

3.3.3 Frequencies from *ab initio* method: Since NMA suffers from the inaccuracies of classical force-field, we performed *ab initio* calculations to verify and compare different vibrational modes at the frequencies observed in the experiment. However, quantum calculations are extremely computationally expensive. Therefore, only a subset of system representing the first solvation shell of a particular alcohol molecule was considered for the calculation. To capture the effect of temperature and various configurational arrangements of molecules, we collected around 20 snapshots at around 100 ps interval. In case of methanol, five molecules were selected. For the other alcohols, only four were selected to reduce computational cost. Also, we did not consider the configurations where there was no hydrogen bonding amongst the small subset of molecules. We have performed optimization and frequency calculation for all the snapshots for each system to obtain the spectrum. Finally, we averaged the spectra from all the different configurations to obtain the average spectrum for each system as shown in Figure 3.10.

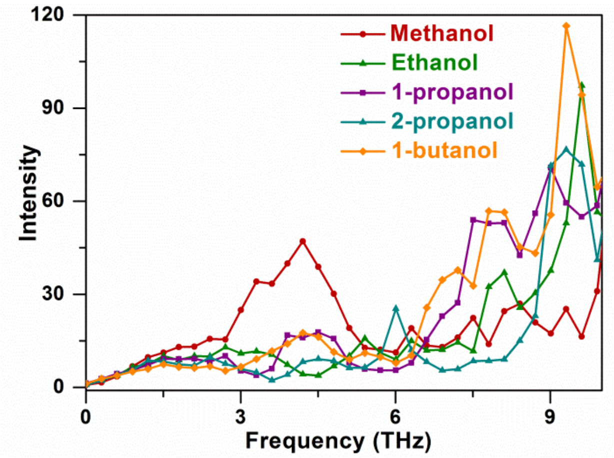

Figure 3.10. The average spectra obtained from frequency calculation of 20 different configurations of each alcohol calculated separately.

Now we can compare the origin of different modes from both classical normal mode analyses and quantum calculations. Both NMA and *ab initio* calculations suggest that the motions below 2 THz region involve the movement of the whole alcohol molecules as shown in Figure 3.7. This observation is consistent with all the alcohol systems studied here.

In the present study, we find that there is a strong absorption in the range of 4-6 THz. The peak position is also found to shift towards higher frequencies as we move from methanol to larger alcohols. Note that the modes in this region (Figure 3.8) do not involve only hydrogen bond motion; rather the motion involves both OH groups and the alkyl chain.

To probe further into the strength of H-bond in different alcohols, we calculated the variation of energy with respect to the H-bond distance as shown in Figure 3.11. We see that methanol requires the highest energy to break the H-bond and also it has higher frequency (from the curvature at the minimum) compared to other alcohols. Therefore, the peak due to the H-bonded motion should appear at the highest frequency for methanol contrary to what is observed in the 4-6 THz range. This ascertains that the frequencies observed in the above region may appear due to the movement of alkyl chains rather than hydrogen bond (O..H) stretching. Interestingly, studies on ionic liquids show that a peak close to 6 THz (200 cm^{-1}) is present only when there is H-bonding present. Also, the frequency above 6 THz has been found to originate from H bonding in different systems.[52,53]

From the above observation and comparison with other systems, we speculate that the H-bonded motions correspond to the experimental peaks above 8 THz. The modes at frequencies above 8 THz obtained from NMA are shown in Figure 3.9. Thus, we can characterize the experimental peaks into the following types: the low-frequency ones (below 2 THz) are likely to originate from the overall motion of the alcohol molecules, while the motion of the alkyl groups gives rise to peaks in 4-6 THz range. Finally, the peaks at higher frequencies involve H-bond movements. However, the reason behind the frequencies of all three oscillators to increase with the size of the alcohols is not understood, and further studies are required.

3.4 Conclusions

We have reported here experimental and theoretical investigations of dielectric response of five mono-hydroxy alcohols in the broad THz frequency range (0.5-10 THz). Earlier experimental reports of similar systems were limited to 2.5 THz. Therefore, this study has widened the scope and understanding of the complex motions involved in these small molecules. Through our extensive experiments, we find that a model combining single Debye and triple damped harmonic oscillators satisfactorily reproduces the experimental complex dielectric spectra. With the help of MD simulations and quantum calculations, we can evaluate the nature of dynamics that respond to our experimental spectral window (0.5-10 THz).

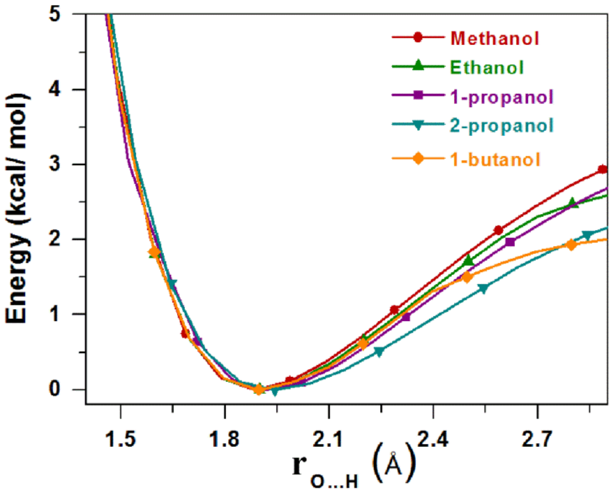

Figure 3.11. The relative energy change as a function of H-bond distance for different systems. The energy values were calculated using constrained optimization using MP2/ aug-cc-pVDZ method.

However, while classical simulations are limited by the choice of the force-field, the quantum calculations suffer from the system size effect. While the qualitative feature of the frequency dependence of the spectrum between 2-6 THz is similar in both theory and experimentation, a quantitative comparison was not possible for all alcohols. We have tried to identify the peaks observed in the dielectric loss spectra and ascribed them to a combination of vibrational modes involving motions of many atoms across several alcohol molecules in the networked structure. Primarily three types of motions were identified: the overall motion of alcohol molecules give rise to peak close to 2 THz, the peaks in intermediate frequency range (4-6 THz) are due to alkyl group oscillations, and the peaks at higher frequency range may be attributed to the signatures of the movement of H-bonded OH groups of the alcohol molecules. Finally, we believe that the study carried out at a broad spectral range in the THz frequency domain will enable researchers to make a judicious choice when selecting these alcohols as a solvent in THz experiments.

3.5 References

(1) Grabowski, S. J. 2006; Vol. 3.
(2) Pimentel, G. C. M., A. L. *Annu. Rev. Phys. Chem.* **1971**, *22*, 347-385.
(3) Pagliai, M.; Cardini, G.; Righini, R.; Schettino, V. *J. Chem. Phys.* **2003**, *119*, 6655-6662.
(4) Kumar Yadav, V.; Chandra, A. *Chem. Phys.* **2013**, *415*, 1-7.
(5) Karmakar, A. K.; Sarkar, S.; Joarder, R. N. *J. Phys. Chem.* **1995**, *99*, 16501-16503.

(6) Kashtanov, S.; Augustson, A.; Rubensson, J.-E.; Nordgren, J.; Ågren, H.; Guo, J.-H.; Luo, Y. *Phys. Rev. B* **2005**, *71*, 104205.
(7) Sarkar, S.; Joarder, R. N. *J. Chem. Phys.* **1993**, *99*, 2032-2039.
(8) Tanaka, Y.; Ohtomo, N.; Arakawa, K. *Bull. Chem. Soc. Jpn.* **1985**, *58*, 270-276.
(9) Ludwig, R. Z., M. D. *Z. Phys. Chem.* **1995**, *189*, 19-27.
(10) Shinokita, K.; Cunha, A. V.; Jansen, T. L. C.; Pshenichnikov, M. S. *J. Chem. Phys.* **2015**, *142*, 212450.
(11) Mazur, K.; Bonn, M.; Hunger, J. *J. Phys. Chem. B* **2015**, *119*, 1558-1566.
(12) Hassion, F. X.; Cole, R. H. *J. Chem. Phys.* **1955**, *23*, 1756-1761.
(13) Hansen, C.; Stickel, F.; Berger, T.; Richert, R.; Fischer, E. W. *J. Chem. Phys.* **1997**, *107*, 1086-1093.
(14) Sato, T.; Buchner, R. *J. Chem. Phys.* **2003**, *118*, 4606-4613.
(15) Sato, T.; Buchner, R. *J. Phys. Chem. A* **2004**, *108*, 5007-5015.
(16) Møller, U.; Cooke, D. G.; Tanaka, K.; Jepsen, P. U. *J. Opt. Soc. Am. B* **2009**, *26*, A113-A125.
(17) Garg, S. K.; Smyth, C. P. *J. Phys. Chem.* **1965**, *69*, 1294-1301.
(18) Barthel, J.; Bachhuber, K.; Buchner, R.; Hetzenauer, H. *Chem. Phys. Lett* **1990**, *165*, 369-373.
(19) Buchner, R.; Barthel, J. *J. Mol. Liq.* **1992**, *52*, 131-144.
(20) Baxter, J. B.; Guglietta, G. W. *Anal. Chem.* **2011**, *83*, 4342-4368.
(21) Schmuttenmaer, C. A. *Chem. Rev.* **2004**, *104*, 1759-1780.
(22) Kindt, J. T.; Schmuttenmaer, C. A. *J. Phys. Chem.* **1996**, *100*, 10373-10379.
(23) Fukasawa, T.; Sato, T.; Watanabe, J.; Hama, Y.; Kunz, W.; Buchner, R. *Phys. Rev. Lett.* **2005**, *95*, 197802.
(24) Yomogida, Y.; Sato, Y.; Nozaki, R.; Mishina, T.; Nakahara, J. i. *J. Mol. Liq.* **2010**, *154*, 31-35.
(25) Yomogida, Y.; Sato, Y.; Nozaki, R.; Mishina, T.; Nakahara, J. i. *J. Mol. Struct.* **2010**, *981*, 173-178.
(26) Xie, X.; Dai, J.; Zhang, X. C. *Phys. Rev. Lett.* **2006**, *96*, 075005.
(27) Kim, K. Y.; Taylor, A. J.; Glownia, J. H.; RodriguezG *Nature Photon* **2008**, *2*, 605-609.
(28) Cook, D. J.; Hochstrasser, R. M. *Opt. Lett.* **2000**, *25*, 1210-1212.
(29) Nashima, S.; Morikawa, O.; Takata, K.; Hangyo, M. *J. Appl. Phys.* **2001**, *90*, 837-842.
(30) Jorgensen, W. L.; Maxwell, D. S.; Tirado-Rives, J. *J. Amer. Chem. Soc.* **1996**, *118*, 11225-11236.
(31) T. Schlick, Molecular modeling and simulation: an interdisciplinary guide (2010).
(32) Berendsen, H. J. C.; Postma, J. P. M.; van Gunsteren, W. F.; DiNola, A.; Haak, J. R. *J. Chem. Phys* **1984**, *81*, 3684-3690.
(33) Nosé, S. *Mol. Phys.* **1984**, *52*, 255-268.
(34) Hoover, W. G. *Phys. Rev. A* **1985**, *31*, 1695-1697.
(35) Parrinello, M.; Rahman, A. *J. Appl.Phys.* **1981**, *52*, 7182-7190.
(36) Darden, T.; York, D.; Pedersen, L. *J. Chem. Phys.* **1993**, *98*, 10089-10092.
(37) (Ed.), D. E. G. *American Institute of Physics Handbook*; McGraw-Hill Book Company, 1963.
(38) Hess, B.; Kutzner, C.; van der Spoel, D.; Lindahl, E. *J. Chem. Theory Comput.* **2008**, *4*, 435-447.
(39) Millam, R. D. a. T. K. a. J. *Semichem Inc. Shawnee Mission KS 2009*.
(40) Yanai, T.; Tew, D. P.; Handy, N. C. *Chem. Phys. Lett* **2004**, *393*, 51-57.
(41) Czarnecki, M. A.; Morisawa, Y.; Futami, Y.; Ozaki, Y. *Chem. Rev.* **2015**, *115*, 9707-9744.

(42) Mitev, P. D.; Bopp, P. A.; Petreska, J.; Coutinho, K.; Ågren, H.; Pejov, L.; Hermansson, K. *J. Chem. Phys.* **2013**, *138*, 064503.
(43) Daub, C. D.; Åstrand, P.-O.; Bresme, F. *J. Phys. Chem. A* **2015**, *119*, 4983-4992.
(44) Dunning, T. H. *J. Chem. Phys.* **1989**, *90*, 1007-1023.
(45) Frisch, M. J.; Trucks, G. W.; Schlegel, H. B.; Scuseria, G. E.; Robb, M. A.; Cheeseman, J. R.; Scalmani, G.; Barone, V.; Mennucci, B.; Petersson, G. A.; Nakatsuji, H.; Caricato, M.; Li, X.; Hratchian, H. P.; Izmaylov, A. F.; Bloino, J.; Zheng, G.; Sonnenberg, J. L.; Hada, M.; Ehara, M.; Toyota, K.; Fukuda, R.; Hasegawa, J.; Ishida, M.; Nakajima, T.; Honda, Y.; Kitao, O.; Nakai, H.; Vreven, T.; Montgomery Jr., J. A.; Peralta, J. E.; Ogliaro, F.; Bearpark, M. J.; Heyd, J.; Brothers, E. N.; Kudin, K. N.; Staroverov, V. N.; Kobayashi, R.; Normand, J.; Raghavachari, K.; Rendell, A. P.; Burant, J. C.; Iyengar, S. S.; Tomasi, J.; Cossi, M.; Rega, N.; Millam, N. J.; Klene, M.; Knox, J. E.; Cross, J. B.; Bakken, V.; Adamo, C.; Jaramillo, J.; Gomperts, R.; Stratmann, R. E.; Yazyev, O.; Austin, A. J.; Cammi, R.; Pomelli, C.; Ochterski, J. W.; Martin, R. L.; Morokuma, K.; Zakrzewski, V. G.; Voth, G. A.; Salvador, P.; Dannenberg, J. J.; Dapprich, S.; Daniels, A. D.; Farkas, Ö.; Foresman, J. B.; Ortiz, J. V.; Cioslowski, J.; Fox, D. J.; Gaussian, Inc.: Wallingford, CT, USA, 2009.
(46) McGregor, J.; Li, R.; Zeitler, J. A.; D'Agostino, C.; Collins, J. H. P.; Mantle, M. D.; Manyar, H.; Holbrey, J. D.; Falkowska, M.; Youngs, T. G. A.; Hardacre, C.; Stitt, E. H.; Gladden, L. F. *Phys. Chem. Chem. Phys* **2015**.
(47) Koeberg, M.; Wu, C.-C.; Kim, D.; Bonn, M. *Chem. Phys. Lett* **2007**, *439*, 60-64.
(48) Tielrooij, K. J.; Paparo, D.; Piatkowski, L.; Bakker, H. J.; Bonn, M. *Biophys. J .* **2009**, *97*, 2484-2492.
(49) Tielrooij, K. J.; Garcia-Araez, N.; Bonn, M.; Bakker, H. J. *Science* **2010**, *328*, 1006-1009.
(50) Sunda, A. P.; Mondal, A.; Balasubramanian, S. *Phys. Chem. Chem. Phys* **2015**, *17*, 4625-4633.
(51) Woods, K. N.; Wiedemann, H. *J. Chem. Phys.* **2005**, *123*, 134506.
(52) Sarangi, S. S.; Reddy, S. K.; Balasubramanian, S. *J. Phys. Chem. B* **2011**, *115*, 1874-1880.
(53) Mondal, A.; Balasubramanian, S. *J. Phys. Chem. B* **2015**, *119*, 1994-2002.

Chapter 4

Hot Electron and Hole Transfer from Colloidal $CsPbBr_3$ Perovskite Nanocrystals

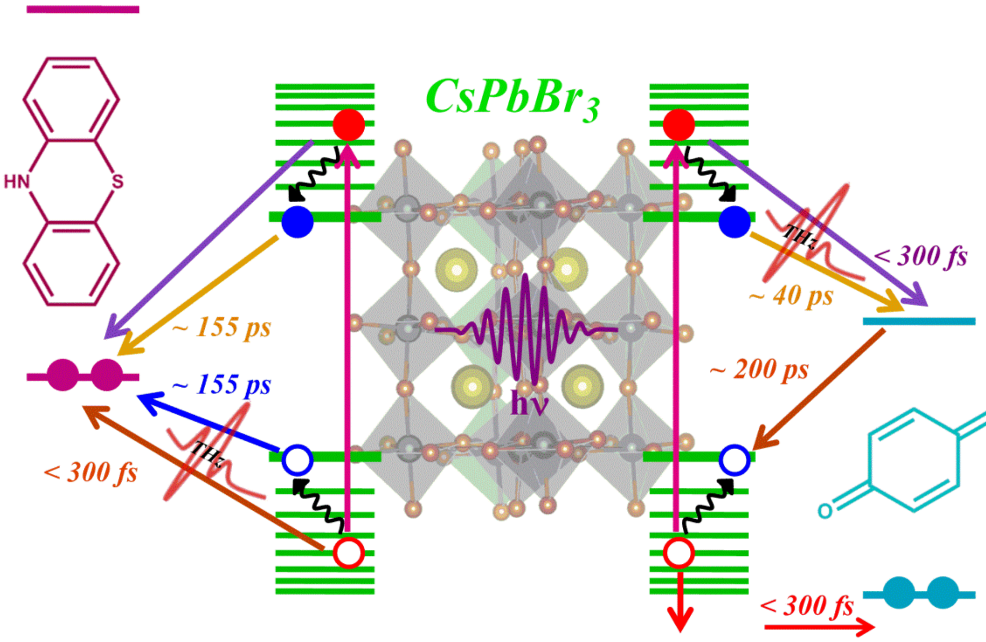

4.1 Introduction

All inorganic $CsPbX_3$ perovskite nanocrystals (NCs) have surfaced as promising materials to be used in optoelectronic devices owing to their amazing properties like high photoluminescence (PL) quantum yield (QY)[1], narrow emission bandwidth,[1] low threshold lasing, [2-4] reduced fluorescence blinking,[5] high carrier mobility,[6] and long diffusion length.[6] Presumably, defect tolerant nature of perovskite NCs give rise to such excellent optical properties. By now the NCs have found applications in light emitting devices,[7-9] photovoltaics,[10,11] and photocatalysis.[12] For better utilization of these NCs it is important to study the charge transfer processes from these NCs since efficient charge transfer is a prerequisite for their successful utilization in photovoltaic and photocatalytic devices. On above band gap excitation, carriers (electrons and holes) with excess energies are created which are commonly called hot carriers. These hot carriers thermalize to band edge within 1 ps[13] by multiphonon emission after which they undergo radiative and non-radiative recombinations. Typical solar cells extract the band edge carriers to produce electrical current. Nevertheless, the excess energy of the carriers gets irreversibly lost due to initial thermalization. Alternatively, if the hot carriers can be extracted, solar cells with power conversion efficiency greater than the Shockley-Queisser limit can be achieved.[14,15] Several recent fs transient absorption (TA) studies on $CsPbBr_3$ NCs have shown that hot carrier relaxation to band edge takes place within 250 – 700 fs. Subsequently, the exciton bleach recovery dynamics which is an outcome of band filling is monitored to probe the electron or hole transfer kinetics from the NCs.[16,17] TA is therefore unable to illustrate the transfer of hot carriers to acceptor molecules since band filling or XB do not have any contribution from hot carriers. TRTS, a noncontact ac probe for conductivity measurement, becomes an appealing tool in this scenario since it measures photoconductivity which is proportional to number of carriers regardless of their occupation states.[18-20] Nevertheless, TRTS is limited by sub-ps temporal resolution. There are not many reports on interfacial charge transfer in $CsPbX_3$ NCs.[21-25] Tim Lian and co-workers reported, for the first time, carrier dynamics within $CsPbBr_3$ NCs and the NCs in presence of electron and hole acceptors using ultrafast TA spectroscopy.[21] Their study was done at quite a low excitation fluence (average electron-hole pairs per NC, $\langle N \rangle = 0.025$) as to not initiate the Auger recombination where they observed an ultrafast exciton dissociation in $CsPbBr_3$ using benzoquinone (BQ) and phenothiazine (PTZ) as molecular electron and hole acceptors, respectively. The efficient electron and hole transfer occurred with half-lives of 65±5 ps and 49±6 ps, respectively, indicating $CsPbBr_3$ NCs as a good choice for solar cell material. In a previous study by our group, we found that at higher excitation fluence (<N>> 1.4) these NCs exhibit efficient nonradiative Auger recombination with a time scale of 20-40 ps that can reduce the efficiency of carrier extraction.[6,26] Though at 1 sun intensity, Auger recombination may not be the prominent decay pathway for solar cells. However, for concentrator photovoltaics, where light intensity is increased by orders of magnitude using optics, Auger recombination will become very significant.[27,28] This will also be relevant in case of multiple exciton generation from absorption of very high energy photons.[29,30] In such a scenario interfacial carrier transfer will have to compete with Auger recombination. Hence, it is very important to study the interfacial carrier transport rates and mechanism in presence of Auger annihilation to reveal the real potential of these NCs as future photovoltaics and photocatalysts.

In this work, we utilized TRTS to understand carrier transfer and recombination dynamics in $CsPbBr_3$ NCs in presence of carrier acceptors at excitation intensities resulting <N> in the range from 0.54 to 1.91. Understanding carrier transfer at NC-molecule interface will provide insight to carrier transfer process at bulk interface.We also chose BQ and PTZ as electron and hole acceptors, respectively, for rational comparison with the TA study done by Wu *et al*. We indeed observed an extremely efficient sub-ps (< 300 fs) hot electron and hole transfer and secondary slower transfer processes of thermalized carriers with a time scales of 20-250 ps in the presence of BQ and PTZ.

4.2 Experimental Section

4.2.1 Synthesis and characterization of colloidal $CsPbBr_3$ nanocrystals:

$CsPbBr_3$ NCs were synthesized and characterized by Vikash Kumar Ravi from Dr. Angshuman Nag's Group. $CsPbBr_3$ NCs were synthesized following a similar procedure reported by Protesescu *et al.*[1]

Preparation of Cs-oleate: Cesium carbonate (0.4 g), oleic acid (1.25 mL) and 1-octadecene (20 mL) were mixed in a 50 mL three neck flask and the mixture was dried at 120^0C for 1 hour under vacuum along with magnetic stirring. Next, the temperature of the reaction mixture was increased to 150°C and kept in the same condition until Cs_2CO_3 completely dissolved.

Synthesis of Colloidal $CsPbBr_3$ NCs: $PbBr_2$ (0.188 mmol) and 5 mL 1-octadecene were mixed in a 50 mL three neck flask and the mixture was dried under vacuum for 1 hour followed by addition of anhydrous oleylamine (0.5mL) and oleic acid (0.5mL) to the mixture at 120°C. Once the solution became clear, the temperature was raised to 190°C and then the prepared Cs-oleate solution (0.1M, 0.4 mL), preheated to 100^{0}C, was swiftly injected to the reaction mixture. The reaction was stopped after 5 sec by dipping the reaction mixture in an ice-water bath. The as synthesized $CsPbBr_3$ NCs were precipitated by adding n-butanol at room temperature and then centrifuged at 10000 rpm for 10 min. Finally, the NC precipitates were redispersed in toluene to form a long-term colloidal stable solution. The NCs were redispersed in 2,2,4,4,6,8,8-heptamethylnonane (HMN) for time-domain and time-resolved THz experiments.

Characterization:

Powder x-ray diffraction (PXRD) data were recorded by a Bruker D8 Advance x-ray diffractometer using Cu Kα radiation (1.54 Å).

Transmission electron microscopy (TEM) studies were carried out using a JEOL JEM 2100 F field emission transmission electron microscope at 200 kV. The sample preparation for TEM was done by putting a drop of the colloidal solution of NCs in hexane on the carbon coated copper grids.

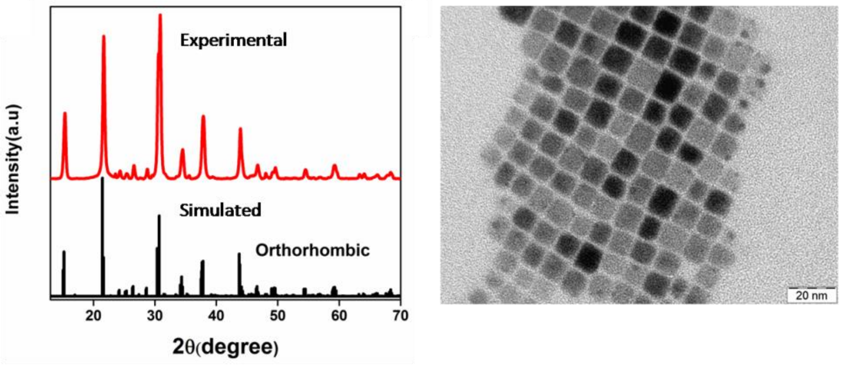

Figure 4.1. a) PXRD confirming orthorhombic crystal structure and b) TEM images of $CsPbBr_3$ NCs.

X-Ray diffraction pattern and TEM images of the synthesized NCs revealed their orthorhombic crystal structure and cube like morphology with edge dimension of ~11±1 nm, respectively.

4.2.2 Preparation of NC-BQ and NC-PTZ complexes

For the preparation of NC-BQ (NC-PTZ) complexes, 2 mg BQ (PTZ) powders were added to 1 ml of $CsPbBr_3$ NCs dispersed in HMN with known concentration.[21] The solutions were sonicated for 10 minutes. We observed no change in UV visible absorption peak position or photoluminescence (PL) peak position of the NCs after they form adsorption complexes with the acceptor molecules (Figure 4.2a).

Normalized UV-visible and PL spectra of $CsPbBr_3$ NCs show that the NCs have their lowest energy exciton absorption at 504 nm (2.46 eV) and excitonic PL at 514 nm (Figure 4.2a). On complex formation with BQ and PTZ, the UV-visible absorption spectrum (Figure 4.2a) of the NCs remained mostly unchanged, but the PL intensity quenches significantly (Figure 4.2b) due to electron and hole transfer. This PL quenching is not due to energy transfer from the NCs to the molecular acceptors as there is no overlap between the emission spectrum of the NCs and the absorption spectra of the molecular acceptors.

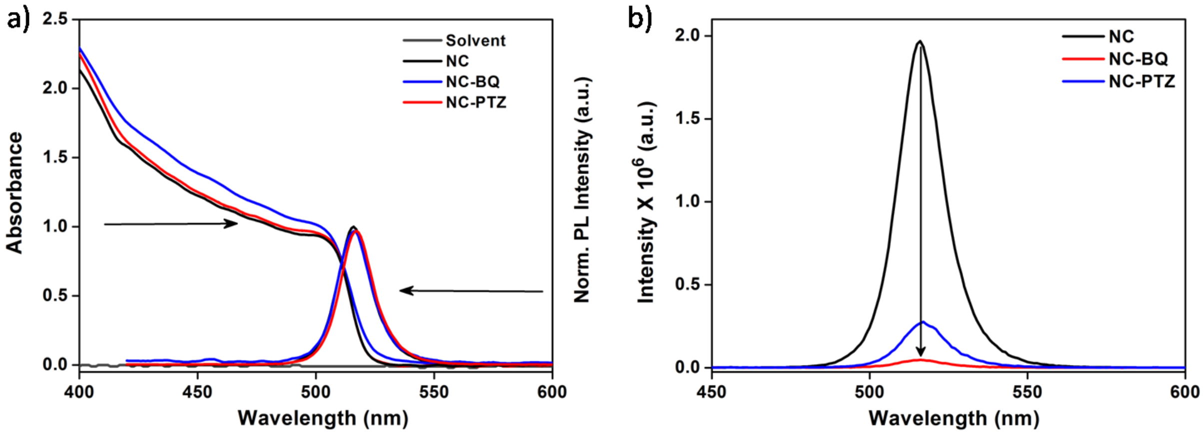

Figure 4.2. a) Normalized UV-visible and PL spectra of $CsPbBr_3$ NCs, NC-BQ, and NC-PTZ complexes. b) Steady state (PL) spectra of $CsPbBr_3$ NCs, NC-BQ, and NC-PTZ complexes. Large steady state PL quenching occurs on addition of BQ and PTZ to the NCs.

4.2.3 Determination of number of acceptor molecules per nanocrystal

We estimated the number of acceptor molecules attached per NC following a previously reported model [21,24,25] which assumes that the NC-acceptor molecule adsorption complex formation is a stochastic process that follows a Poissonian distribution,[21,23,25]

$$P(n) = \frac{e^{-m} m^{n}}{n!} \qquad (1)$$

where P(n) is the probability of finding a NC with n adsorbed molecules and m is the mean number of molecules attached to a NC.

The model also assumes that the complex formation between the acceptors and the NCs is governed by Langmuir adsorption isotherm.[21,24,25]

$$\theta = \frac{m}{N} = \theta_{max} \frac{K_a[A]}{1 + K_a[A]} \qquad (2)$$

where θ is the mean fractional coverage of molecular acceptors on NC surface, N is the number of binding sites on the NC surface, θ_{max} is the maximum fractional coverage of acceptors on NCs, K_a is the binding constant of the acceptors, and [A] is the total concentration of the acceptors.

To determine θ, the acceptor concentration dependent steady state photoluminescence of the NC dispersed in hexane was measured. The emission spectra of the solutions taken in 1 cm path length quartz cuvette were recorded using FLS 980 (Edinburgh Instruments) over 420 -700 nm range. The excitation wavelength used was 400 nm. With increasing concentration of the acceptor molecules, the PL intensity decreased Due to non-radiative carrier transfer.

Now, the probability of finding NCs without any acceptor attached to it is given by the ratio of integrated PL intensity in presence of acceptor (PL) to that in absence of any acceptor(PL_0). The following equation gives the relationship between PL/PL_0 and θ,[23]

$$\frac{PL}{PL_0} = (1 - \theta)^{N} \qquad (3)$$

Assuming that PTZ and BQ preferentially bind to Pb^{2+}, N is estimated to be ~ 12800 according to the following equation:

$$N = \frac{\pi}{4}\left(\frac{6a^{2}}{\pi r_{Pb^{2+}}{}^{2}}\right) \qquad (4)$$

where a = 11 nm is the edge length of cubic $CsPbBr_3$ NCs and $r_{Pb^{2+}}$ = 0.119 nm.

By plotting θ vs. [A] and fitting it to equation (2), $θ_{max}$, and eventually m is calculated. Figure 4.3 shows the integrated PL intensity decay (red) and increasing m (blue) with increasing concentration of the molecular acceptors.

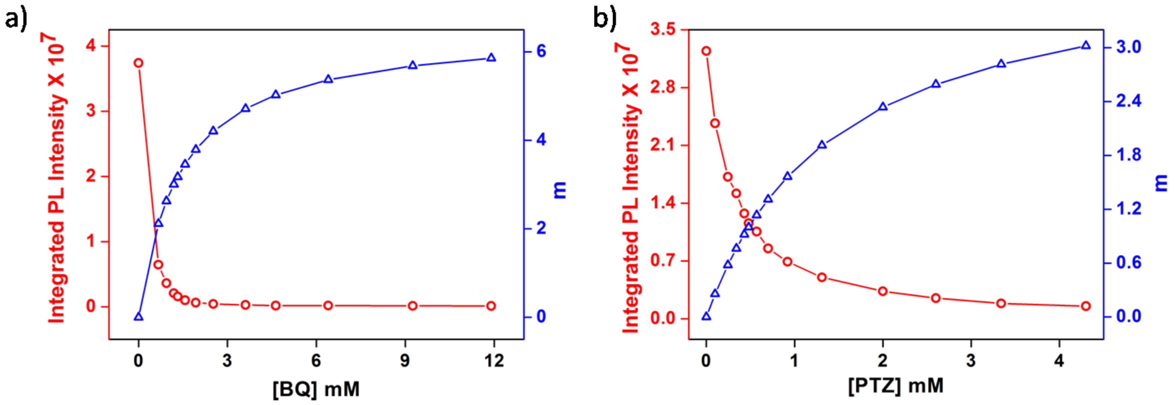

Figure 4.3. a) The integrated PL intensity of $CsPbBr_3$ NCs (red) and the number of BQ molecules attached per NC (blue) with increasing BQ concentration. b) Integrated PL intensity of $CsPbBr_3$ NCs (red) and the number of PTZ molecules attached per NC (blue) with increasing PTZ concentration.

4.2.4 Cyclic Voltammetry Study

To find out the absolute energies of the lowest unoccupied molecular orbital (LUMO) and the highest occupied molecular orbital (HOMO) for BQ and PTZ, respectively, cyclic voltammetry (CV) measurements were performed with the help of PAR Potentiostat/Galvanostat (model PARSTAT 2273). A commercial Pt disk electrode (CHI Instruments, USA, 2-mm diameter), Ag wire, and Pt-wire loop were used as working, quasi-reference, and counter electrodes, respectively. Measurements were carried out under a nitrogen atmosphere, where anhydrous acetonitrile was used as a solvent and 100 mM tetrabutyl ammonium perchlorate was used as supporting electrolyte. Potentials were calibrated with respect to the normal hydrogen electrode (NHE) and vacuum using ferrocene/ferrocenium redox couple as an internal standard.[31]

As shown in figure 4.4 a), oxidation of PTZ gives two reversible peaks which were assigned to two step oxidations of PTZ, and from the onset potential, the HOMO level is calculated to be 5.00 eV.

Reduction of BQ gives one reversible peak (Figure 4.4 a) and the LUMO level is calculated to be 4.16 eV from the peak onset potential. To determine the other energy level (HOMO of BQ and LUMO of PTZ), the optical gap obtained from UV-vis absorption spectra of BQ and PTZ dispersed in hexane (Figure 4.4 b) is used. BQ has a broad absorption peak around 450 nm and considering the $n \rightarrow \pi^*$ transition at 450 nm wavelength, the HOMO for BQ is calculated to be - 6.91 eV. In case of PTZ, the LUMO was calculated to be – 1.19 eV, considering the $\pi \rightarrow \pi^*$ transition at 325 nm. Inset of Figure 4.4b shows the absorption of BQ and PTZ from 350 nm to 550 nm.

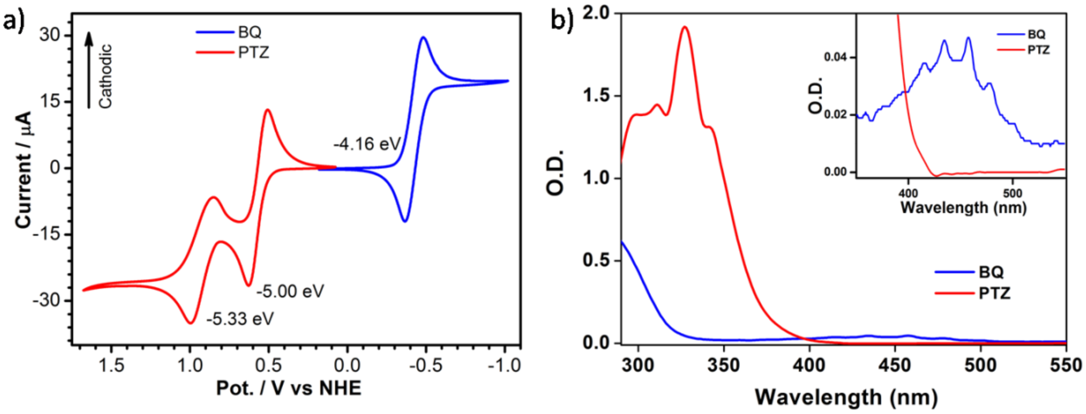

Figure 4.4. a) Cyclic voltammetry redox cycles of Benzoquinone and Phenothiazine recorded in 100 mM tetrabutyl ammonium perchlorate used as supporting electrolyte and anhydrous acetonitrile used as a solvent. b) UV-vis absorption of BQ and PTZ dissolved in hexane used to calculate HOMO for BQ and LUMO for PTZ.

4.2.5 NMR Spectroscopy

To find out the interaction between the NCs and the acceptor molecules, we recorded NMR spectra of the NC-BQ/PTZ complexes and free BQ and PTZ molecules in a solvent. For NMR sample preparation, as synthesized $CsPbBr_3$ NCs were centrifuged for 10 minutes at 7000 rpm. The supernatant was discarded while the precipitates were re-dispersed in $CHCl_3$ followed by re-precipitation on acetonitrile addition and centrifugation at 7000 rpm. The supernatant was discarded and the washing was repeated twice. Finally, the NCs were dispersed in $CDCl_3$ (99.8 atom % D, Sigma-Aldrich) for NMR data acquisition. Benzoquinone (BQ) purchased from Sigma Aldrich ($purity \geq 98\ \%$) and phenothiazine (PTZ) purchased from TCI Chemicals ($purity \geq 98\ \%$) were separately dispersed in $CDCl_3$ for NMR measurements. NC- BQ complex was formed by mixing BQ in NC dispersed in $CDCl_3$. Similarly, NC- PTZ complex was formed by mixing PTZ in NC dispersed in $CDCl_3$. All NMR spectra were recorded using a Bruker Avance III HD spectrometer operating at a ^1H frequency of 400 MHz, at 298 K.

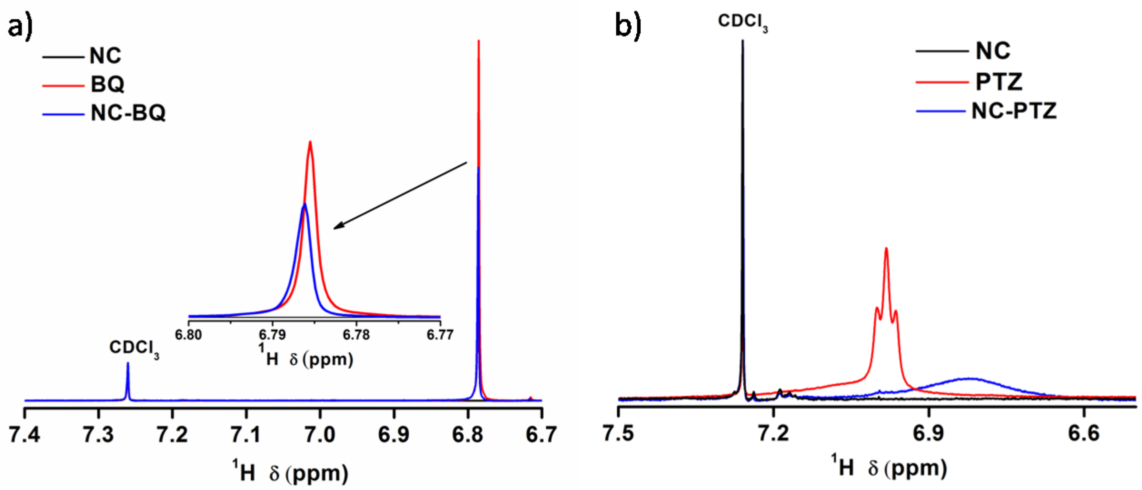

Figure 4.5. ^{1}H NMR of a) BQ and NC- BQ complex and b) PTZ and NC- PTZ complex, dispersed in CDCl$_3$, normalized with respect to solvent peak intensity.
The NCs are capped with oleylamine capping ligands. Since the peak intensity for oleylamine protons is too high, overshadowing the peaks from other protons, peak intensities are normalized with respect to the solvent (CDCl$_3$) peak.

Comparing the normalized aromatic proton peak intensity of BQ and NC- BQ complex, we observe that its intensity in NC-BQ complex has reduced. There is a slight downfield shift in the peak position due to the interaction between BQ and NC. Comparing the aromatic proton peak intensity in PTZ-NC complex and in PTZ normalized with respect to CDCl$_3$ peak (Figure 4.5 b), broadening of the aromatic signals from PTZ and shift towards lower frequency in NC-PTZ complexes is observed indicating binding of PTZ to the NCs. Close proximity of the phenyl rings of PTZ to the NCs and rigidity of the phenyl rings result in constrained rotational motion of PTZ when they are bound to NCs, leading to peak broadening.[32,33]

4.2.6 FTIR Spectroscopy

To find out the interaction between the NCs and the acceptor molecules we recorded the FT-IR spectra of the NCs, NC-BQ/PTZ complexes, and the free BQ and PTZ molecules in a solvent. The FT-IR spectra were obtained using a NICOLET 6700 FT-IR spectrophotometer and are given in Figure 4.6. The NCs and their complexes with BQ and PTZ were dispersed in hexane. The C=O stretching mode shifts to a higher frequency when BQ forms complex with NC indicating loss of conjugation. However, for NC-PTZ complex we do not see appreciable signature in IR spectra.

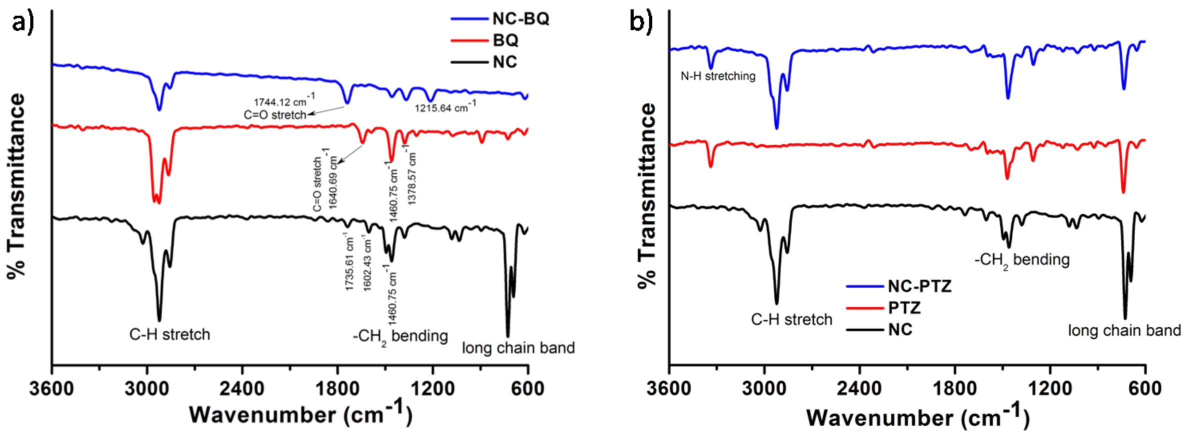

Figure 4.6. FTIR spectra of a) NC, BQ, and NC-BQ and b) NC, PTZ, and NC-PTZ complex dispersed in hexane.

4.2.7 THz-Time Domain (THz-TDS) and THz Time-Resolved Spectroscopy (TRTS)

Details of THz-TDS and TRTS setup and related data analysis procedure are given in Chapter 2. $CsPbBr_3$ NCs, NC-BQ, and NC-PTZ complexes were dispersed in HMN, which is fairly transparent in THz range. THz-TDS and TRTS data for the three samples were recorded in the frequency range of 0.5 – 7 THz, at room temperature. Frequency averaged and frequency resolved THz data were recorded for the samples using the double lock-in technique, in which the pump induced change in THz transmission ($-\Delta E(\tau_p)$) and the corresponding THz transmission through the non-photoexcited NCs ($E_0(\tau_p)$) are simultaneously recorded.[34] This reduces the effect of laser fluctuation in data acquisition. For THz-TDS and TRTS measurements, sample cell comprising two TPX windows of 2 mm thickness separated by a Teflon spacer of 950 μm thickness was filled with the NC and its different complexes dispersed in HMN. Unlike quartz cuvettes where the TRTS study is limited to 2.5 THz, with TPX windows the frequency dependent photoconductivity can be recorded till 15 THz. However, our TRTS study is limited to 7 THz due to unavailability of a suitable filter material which can block the optical pump but, transmit the THz light with a frequency greater than 7 THz. For TRTS measurements the NCs and its complexes with BQ and PTZ were excited using pump wavelengths of 400 nm (3.1 eV) and 480 nm (2.58 eV) which provide 640 meV and 120 meV of excess energy than required for band edge excitation. Uniform probing of the photoexcited sample was guaranteed by keeping the optical pump beam diameter (~ 3.5 mm) three times the size of THz probe beam diameter (~ 1 mm).

THz-TDS: Figure 4.7 shows the THz absorbance spectra of neat NC, NC-BQ and NC-PTZ complexes dispersed in HMN in the frequency range 0.5 to 7 THz. $CsPbBr_3$ NCs show a prominent absorption peak at ~3.4 THz (115 cm^{-1}) and a shoulder close to 1.5 THz. From DFT calculations done on the orthorhombic phase of $CsPbBr_3$ in our previous work,[6] we know that absorption features in the THz-TDS of the NCs arise due to the infrared active (IR) lattice vibrations (optical phonons) within the orthorhombic lattice of the NCs . The THz-TDS spectra for NC-BQ and NC-PTZ complexes are the same as for the neat NCs, which suggest that the complex formation with electron and hole acceptor molecules do not affect the lattice vibrations occurring within the orthorhombic lattice of the NCs in unexcited state.

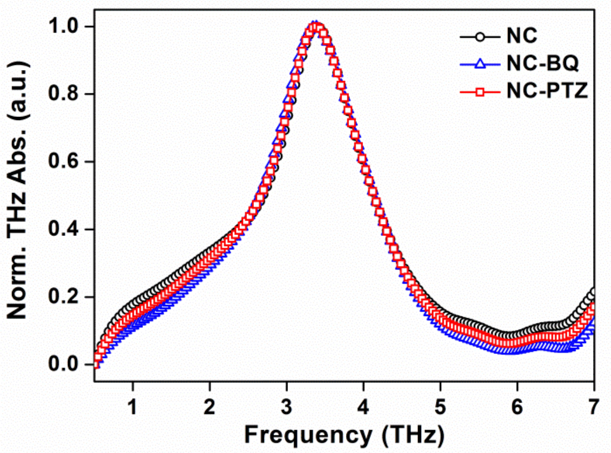

Figure 4.7. Time domain THz absorbance spectra of non-photoexcited $CsPbBr_3$ NCs, NC-BQ, and NC-PTZ complexes.

Frequency Averaged THz Data: Above bandgap excitation of the NCs using optical pump creates hot charge carriers. THz absorption by these carriers results in attenuation of THz transmission. Frequency averaged THz data are collected by varying the delay between the optical pump and THz probe keeping delay stage fixed at peak of the THz field (t_{max}) (Chapter 2).[6] We acquire the temporal evolution of the sample after photoexcitation by collecting the pump induced change in the peak of THz field, $\Delta E(t_{max}, t_p)$, as a function of delay between THz probe and optical pump pulses, t_p. This decreased transmission is $(-\Delta E(t_p)/E_0(t_p))$ proportional to the photoconductivity of the medium. It is essential to highlight that in this study the NCs are dispersed in a non-conducting solvent (HMN) with a volume fraction of the order of 10^{-3}, and thus the photoconductivity measured is within the NCs. Simple effective medium approach (EMA) for dielectric inclusion embedded in a host medium has been employed to estimate the frequency dependent complex dielectric function[35]:

$$\varepsilon_{eff}(\nu) = f\,\varepsilon_i(\nu) + (1-f)\,\varepsilon_h(\nu) \qquad (5)$$

where $\varepsilon_{eff}(\nu)$, $\varepsilon_i(\nu)$ and $\varepsilon_h(\nu)$ are the complex dielectric functions of the NC solution, NCs only and the solvent (HMN) respectively; and f is the volume fraction of the NCs in the solution.

Using the following equation, intrinsic peak photoconductivity values of neat NC, NC-BQ and NC-PTZ complexes can be calculated:[6]

$$\Delta\sigma(t_p) = \frac{\varepsilon_0 c}{d}(n_a + n_b)\frac{-\Delta E(t_p)}{E_0(t_p)} \qquad (6)$$

where ε_0 is the permittivity of free space, c is the speed of light, d is the thickness of the photoexcited sample, n_a and n_b are the refractive indices of the media on either side of the sample.

In this work, we have reported the THz conductivity normalized with respect to the carrier density at different wavelengths and fluences using the following equation:

$$\varphi\mu = \varphi(\mu_e + \mu_{\hbar}) = \frac{\Delta\sigma}{N_0 q} = \frac{\varepsilon_0 c}{q N_0}(n_a + n_b)\frac{-\Delta E(t_p)}{E_0(t_p)} \quad (7)$$

where q is the elementary charge, N_0 is the carrier density, and φ is the photon to free carrier conversion ratio. Here, it is assumed that $\varphi = 1$ and every photon gives rise to an electron hole pair. Therefore, $N_0 = \varphi \times 2\ N_{ph}$ and this sets the upper limit to the carrier concentration and lower limit to the effective mobility ($\varphi\mu$) as the losses due to reflection or scattering are not taken into consideration. Also, for orthorhombic $CsPbBr_3$, theoretical studies predict comparable effective masses for electrons and holes and therefore they should equally contribute to the mobility, $\varphi\mu = \varphi(\mu_e + \mu_h)$.

On addition of acceptor molecules to the NC dispersed in HMN, we do observe a slight increase in the absorbance in the UV-visible absorption spectra of the NC-molecule system (Figure 4.4b). This little difference in absorbance is due to the absorption by the acceptor molecules and has been taken into account while calculating the number of photons absorbed by the NCs. As we compare the conductivity normalized to the density of the absorbed (by the NCs) photons (Figure 4.8), the quenching in conductivity observed should not have any influence due to the absorption by the free molecules.

4.3 Results and Discussions

The driving forces (-ΔG) for electron transfer to BQ and hole transfer to PTZ from $CsPbBr_3$ NCs are 0.81 eV and 0.85 eV, respectively. Driving force can be calculated knowing the value for valence band minimum (VBM) and conduction band maximum (CBM) for these NCs and HOMO and LUMO energy values for the molecular acceptors. The VBM and CBM of these NCs are -5.85 eV and -3.35 eV, respectively as determined by recent cyclic voltammetry (CV) study conducted by Ravi *et al.*[36] Using CV, we determined the LUMO for BQ to be -4.16 eV and HOMO for PTZ to be -5.0 eV.

When the NCs form adsorption complexes with the molecular acceptors additional processes associated with electron and hole transfer occur that may result to an altered transient THz photoconductivity compared to that observed for the neat NCs. We emphasize that only the mobile charges in the NCs couple effectively to the THz probe and give rise to signal observed in TRTS.[19,37] Localized carriers in acceptor molecules do not respond to the low energy THz probe. Above band gap excitation initially creates hot excitons. In neat NCs, in the absence of any acceptor molecule, within sub-ps time scale, all excitons relax to the band edge prior to any recombination processes. On the other hand, in the presence of carrier acceptor molecules, the photo-generated hot excitons have multiple options for losing their energy. The excitons might 1) relax to the band edge, 2) dissociate quickly and get transferred to the acceptor molecules prior to relaxation to the band edge, or both (1) and (2).

Figure 4.8 shows pump-induced conductivity transients of neat NC solution, NC-BQ and NC-PTZ complexes normalized with respect to the density of absorbed photons (initial carrier density N_0) at 400 and 480 nm pump wavelengths. The THz kinetics show remarkably strong quenching (with respect to that in neat NC) of the initial conductivity (at pump-probe delay, t_p=0) in the presence of the molecular carrier acceptors.

The quenching is as high as ~90% in NC-BQ system and ~80% in the case of NC-PTZ complex (Table 4.1). This clearly indicates to a huge reduction in charge carrier density within the NCs at an ultrafast timescale, even faster than our instrument response time (IRF) of ~300 fs, in the presence of the carrier acceptors. This reduction in carrier density is only possible by a sub-300 fs electron (hole) transfer from the photoexcited NCs to BQ

(PTZ) molecules. The carrier transfer process is so fast that it may have occurred even before thermalization of the hot carriers. Recently, Maity *et al.* reported hole transfer from $CsPbBr_3$ NCs to a hole acceptor molecule, 4,5-dibromofluorescein, to occur at 1-1.25 ps time scale.[22] Ponseca *et al.* also reported a sub-200 fs hole transfer from $CH_3NH_3PbI_3$ polycrystalline film to Spiro-OMeTAD, a frequently used organic hole acceptor.[38]

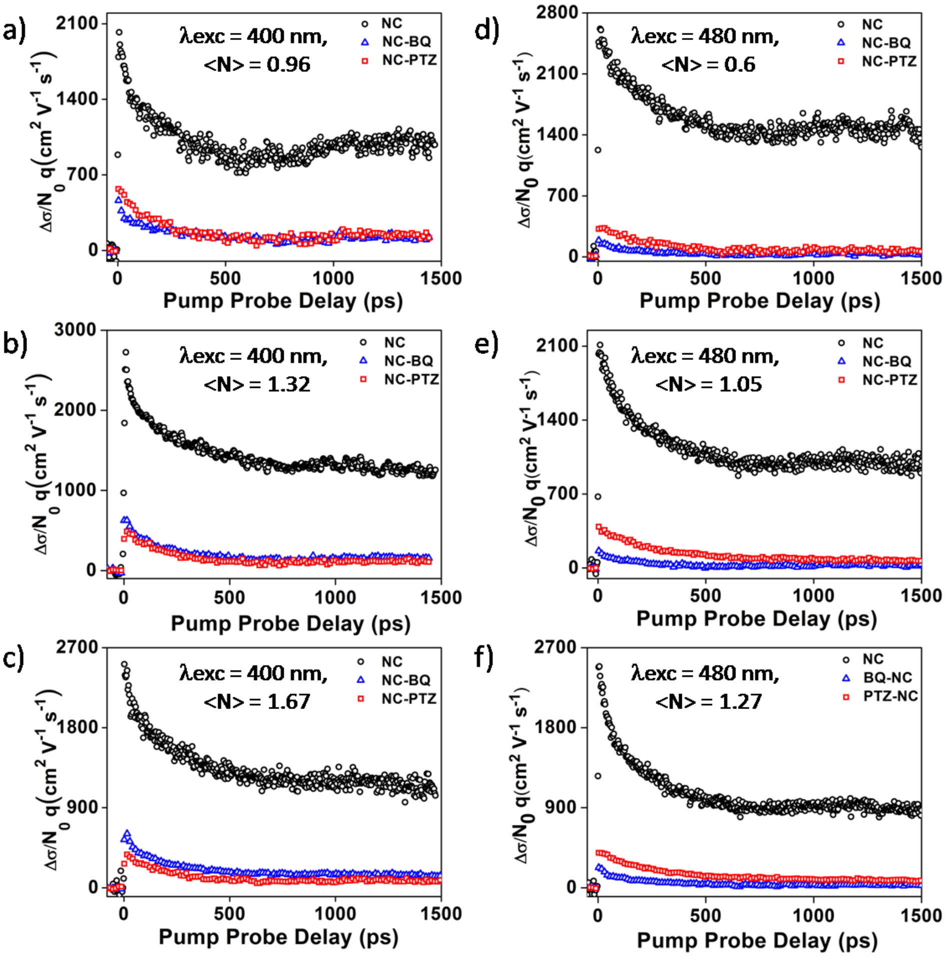

Figure 4.8. THz conductivity of neat NCs, NC-BQ and NC-PTZ complexes normalized with respect to density of absorbed photons when a) λ_{exc} = 400 nm ,<N> = 0.96 b) λ_{exc} = 400 nm ,<N> = 1.32, c) λ_{exc} = 400 nm ,<N> = 1.67, d) λ_{exc} = 480 nm ,<N> = 0.6, e) λ_{exc} = 400 nm ,<N> = 1.05 and f) λ_{exc} = 400 nm ,<N> = 1.27

In this study <N> was varied from 0.54 to 1.91. From previous reports, we know that at <N> ~1.4, $CsPbBr_3$ NCs undergo efficient Auger recombination with a time scale of 20-40 ps.[6,26] This will lead to a competition between Auger recombination and interfacial carrier transfer. But from above results, we can unambiguously prove that in presence of BQ and PTZ as electron and hole acceptor molecules, respectively, the interfacial electron and hole transfer takes place at a time scale much faster than the Auger recombination.

Thus, the photovoltaic and photocatalytic efficiencies should not be affected by the detrimental Auger process.

Table 4.1. The decrease in initial conductivity of NCs normalized with respect to the density of absorbed photons in the presence of BQ and PTZ as electron and hole acceptors, respectively.

λ_{exc}	Fluence ($\mu J/cm^2$)	<N>	Conductivity Quenching (%)	
			BQ	PTZ
400	41	0.96	75	68.5
	57	1.32	69.4	77.7
	72	1.67	73	84.2
480	39.5	0.6	92	87.5
	72.7	1.05	92	81.1
	93.5	1.27	90	83.5

Theoretical calculations predict similar effective masses for electrons and holes (m_e=0.22, m_h=0.24)[6] implying that both electrons and holes should evenly contribute to the observed photoconductivity. Hence, in NC-BQ (NC-PTZ) complex, more than 50 % reduction in initial conductivity (with respect to that in neat NCs), even if all photo-generated hot electrons (holes) are transferred to LUMO (HOMO) of BQ (PTZ) is unanticipated. Several factors might contribute to this unexpected conductivity quenching. An Auger assisted mechanism for electron and hole transfer can partially explain the above observation.[39] As shown schematically in Figure 4.9 (right panel, arrow 2-3-4), in Auger assisted electron/hole transfer process the excess energy (ΔG) released due to the electron (hole) transfer reaction is consumed by the hole (electron). The energized hole (electron) may attain enough energy to be at par with the HOMO (LUMO) of BQ (PTZ), and may as well get transferred to the HOMO (LUMO) of the acceptor molecule. According to the band alignment, this mechanism seems to be feasible in case of NC-BQ complex when photoexcited with 400 nm pump.

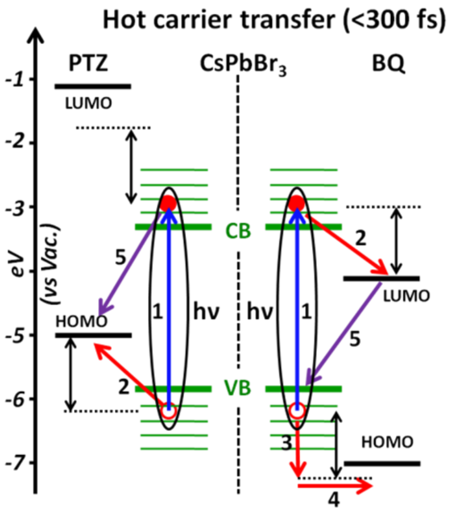

Figure 4.9. Schematic representation of possible mechanism of ultrafast (< 300 fs) carrier transfer and charge recombination processes in $CsPbBr_3$ NC-BQ and NC-PTZ system upon photoexcitation. 1: photoexcitation, 2: hot e/h transfer, 2-3-4: Auger assisted e/h transfer, 5: back transfer

However, in case of NC-PTZ complex, the energy analysis does not support such a mechanism. The second plausible mechanism is an ultrafast interfacial back transfer (process 5 in Figure 4.9) soon after the carrier transfer from NCs to molecular acceptors, thus reducing the carrier density. Both processes essentially lead to interfacial charge recombination (CR) involving slightly different time scales. One should note that such CR should be avoided if these NCs are to be used in photovoltaics. We anticipate that in the simultaneous presence of suitable electron and hole transport layers, CR can be minimized as the initial transfer of both electrons and holes are equally fast.

Frequency resolved data are acquired by measuring the pump induced change in the THz waveform, $\Delta E(t, t_p)$, at a fixed pump probe delay (t_p). A typical ΔE and E_0 signals are shown in Figure 4.10 a. The photoinduced change in complex conductivity ($\Delta\sigma$) is calculated from the observed photoinduced change in THz transmission ($-\Delta E/E_0$). The free carriers generated by photoexcitation mostly show Drude (or Drude Smith) type response. Furthermore, photoexcitation may induce change in the amplitude of IR-active phonon vibrations having frequencies in the range of THz probe light which leads to additional resonant absorption at those particular phonon frequencies. To identify the phonon peaks observed in photoexcited samples, conductivity spectra (real and imaginary) obtained from frequency resolved data were simultaneously fitted to Drude-Smith plus Lorentz model.[40,41] Lorentzians are often used to account for contribution of resonant phonon vibrations to the complex conductivity spectra obtained in TRTS experiments.[42-44]

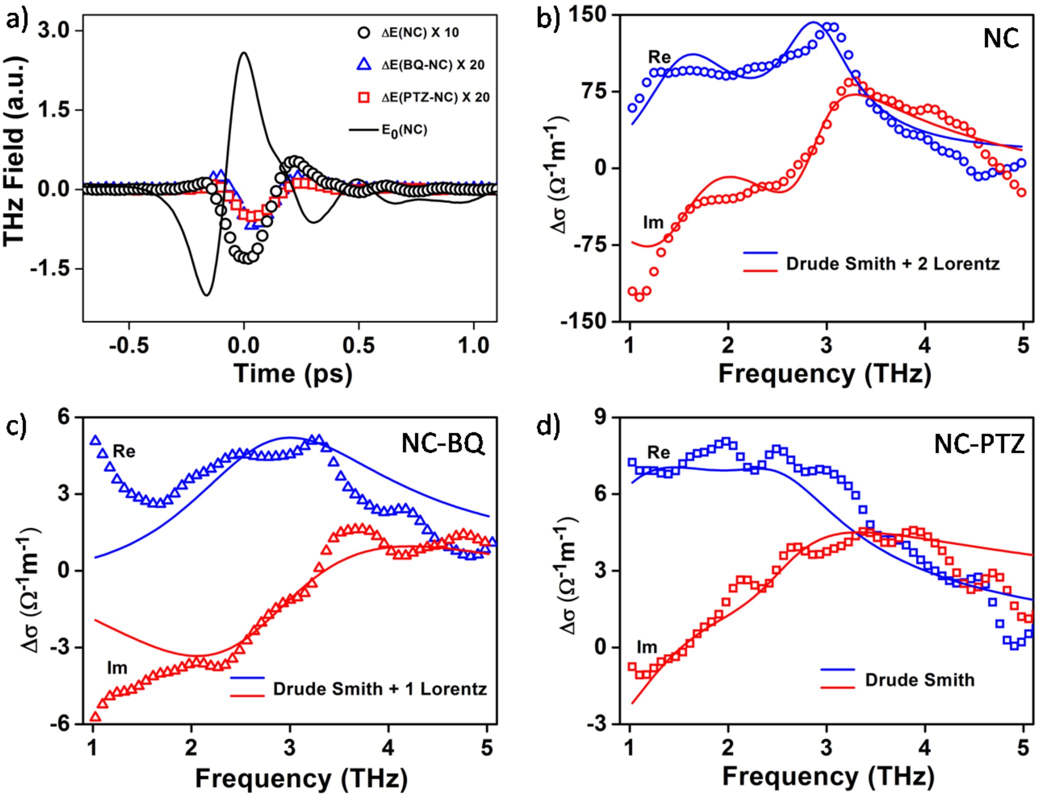

Figure 4.10 a) Typical THz waveforms in TRTS measurements at λ_{exc} = 400 nm. E_0 is the pump-off signal plotted in black solid line. Pump induced change of THz field is plotted as ΔE. Real (red symbols) and imaginary (blue symbols) conductivity spectra at λ_{exc} = 480 nm, ~ 72 μJ/cm^2 fluence (<N> ~ 1.3) for b) neat NCs, c) NC-BQ and d) NC-PTZ complexes. Solid lines are the fits to the Drude-Smith (DS) plus two Lorentz (b), DS plus one Lorentz (c), and only DS (d). The Lorentz oscillator(s) is used to model the contribution of phonon vibrations to the conductivity spectra.

$$\sigma = \frac{\sigma_{DC}}{1-i\omega\tau}\left(1+\frac{C_1}{1-i\omega\tau}\right)+\sum_{j=1}^{2}\frac{iF_j\omega}{\left(\omega^2-\omega_{0j}^2\right)+i\omega\gamma_j} \quad (8)$$

Here $\sigma_{DC} = \omega_p^2\epsilon_0$ and ω_p is plasma frequency. Carrier density can be calculated from ω_p through $n = \epsilon_0\omega_p^2 m^*/e^2$ with $m^* = 0.22m_e$[6,45] being the effective mass of the electron, τ is momentum relaxation time, c_1 represents degree of carrier localization; $c_1 = -1$ represents complete localization and $c_1 = 0$ represents complete delocalization or free carrier response. F_j is the oscillator strength corresponding to the jth oscillator with angular frequency ω_{0j} and lifetime broadening parameter γ_j. We observe that Drude

Smith plus double oscillators model is required to fit the conductivity data of neat NCs whereas Drude Smith plus Single Oscillator model and only Drude Smith model can fit the conductivity data of NC-BQ and NC-PTZ, respectively. Parameters obtained from fitting the complex conductivity of NC, NC-BQ and NC-PTZ complexes using the above discussed models are listed in Table 4.2 and 4.3.

The photoinduced change in phonon amplitude (spectrum) should appear in the complex conductivity spectra (complex dielectric function) obtained from the TRTS measurements. Figures 4.10 b, c and d show the complex conductivity spectra induced by 480 nm excitation (<N> = 1.3) at 0 ps pump-probe delay (at the peak of the THz transients) for neat NCs, NC-BQ and NC-PTZ systems, respectively. In neat NCs strong phonon modes are observed at ~1.8 THz and ~3 THz in the real conductivity spectrum which is an implication of hot carrier relaxation occurring in sub-ps time scale. The appearance of phonon modes on pump induced conductivity spectra is an indication of strong carrier-phonon coupling, and a multiphonon process to be responsible for hot carrier relaxation. Similar observations have also been reported earlier in organo-metal-halide perovskite systems.[37,46-48] Recent TA studies also report the hot carrier relaxation in $CsPbBr_3$ NCs to occur in time scale in the range of 310-700 fs.[21,49-51] On the other hand, only a weak phonon band at ~3 THz is observed in the photoconductivity spectrum of NC-BQ complex whereas the spectrum of NC-PTZ complex is completely devoid of any phonon absorption. This observation strongly indicates that hot carrier relaxation and carrier transfer take place at similar time scale in NC-BQ complex whereas carrier transfer is probably even faster than hot carrier relaxation to the band edge in case of NC-PTZ system. It is expected that the carrier cooling rate may not alter much on complex formation. Hence, it may be inferred that the hot hole transfer process is relatively more efficient compared to hot electron transfer process.

Table 4.2. Parameters obtained by fitting the conductivity of neat NCs, NC-BQ and NC-PTZ complexes using Drude Smith plus two Lorentz oscillators, Drude Smith plus single Lorentz oscillator and Drude Smith model respectively at 0 ps pump probe delay, 480 nm excitation wavelength and at <N> ~ 1 where <N> is average number of electron hole pairs.

	σ_{DC} (Ω^{-1} m^{-1})	τ (fs)	c	f_1 (10^{14})	ω_1 (THz)	γ_1 (THz)	f_2 (10^{14})	ω_2 (THz)	γ_2 (THz)
NC	190 (21.8)	5.44 (2.6)	-0.99 (0.01)	9.5 (0.9)	1.72 (0.03)	9.23 (0.9)	4.3 (0.5)	3 (0.1)	4.25 (0.41)
NC-BQ	6.4 (0.001)	60.5 (4.6)	-0.99 (0.01)	1.76 (0.42)	3.19 (0.045)	6 (1.25)	-	-	-
NC-PTZ	15.05 (0.01)	102 (3.8)	-0.98 (0.04)	-	-	-	-	-	-

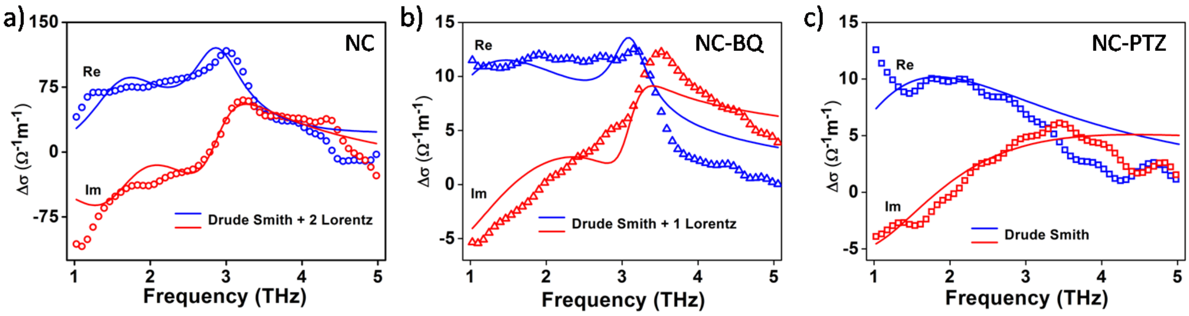

Figure 4.11. Real (red symbols) and imaginary (blue symbols) conductivity spectra at λ_{exc} = 400 nm, <N> ~ 1.3 a) neat NCs, b) NC-BQ and c) NC-PTZ complexes. Solid lines are the fits to the Drude-Smith (DS) plus two Lorentz (a), DS plus one Lorentz (b), and only DS (c). The Lorentz oscillator(s) is used to model the contribution of phonon vibrations to the conductivity spectra.

Table 4.3: Parameters obtained by fitting the conductivity of neat NCs, NC-BQ and NC-PTZ complexes using Drude Smith plus two Lorentz oscillators, Drude Smith plus single Lorentz oscillator and Drude Smith model respectively at 0 ps pump probe delay, 400 nm excitation wavelength and at <N> ~ 1.3 where <N> is average number of electron hole pairs.

	σ_{DC} (Ω^{-1} m^{-1})	τ (fs)	c	f_1 (10^{14})	ω_1 (THz)	γ_1 (THz)	f_2 x (10^{14})	ω_2 (THz)	γ_2 (THz)
NC	199.14 (0.25)	5.76 (2)	-0.99 (0.01)	9.73 (0.92)	2.87 (0.02)	5.2 (0.54)	4.31 (0.52)	1.67 (0.04)	8 (1.4)
NC-BQ	21.1 (0.01)	127 (16)	-1 (0.11)	4.91 (1.0)	2.79 (0.03)	6.67 (0.1)	21.1 (0.01)	-	-
NC-PTZ	17.84 (0.00)	99 (5)	-0.99 (0.05)	-	-	-	-	-	-

Weak phonon mode in NC-BQ and absence of phonon modes in NC-PTZ complexes explains why Wu *et al.* did not observe any sub-ps electron/hole transfer in their TA experiment of the same systems. As mentioned earlier, if hot carriers are transferred to the molecular acceptors prior to thermalization, they will not contribute to the band-filling and related exciton bleaching. Previously, hot electron transfer has been observed from PbSe NCs to TiO_2 surface in sub-50 fs time scale[13], from graphene quantum dots to TiO_2 surface at <15 fs time scale,[52] and also from CdSe NCs to ZnO surface at sub-200 fs time scale.[53]

According to above observation, in the presence of the acceptor molecules, the majority (70-90%) of the hot excitons are dissociated and transferred to the acceptor molecules in sub-300 fs time scale which results into the quenching of the initial conductivity (Figure 4.9a). Rest (10-30%) of the excitons undergo intraband cooling and relax to the band edge. These residual thermalized excitons eventually dissociate to free carriers and show up as the increasing conductivity over a period of several ps in our THz transient data (Figure 4.8 and Figure 4.12). Figures 4.12a and 4.12b show the temporal evolution of photoconductivity normalized to the maximum value of neat NCs as well as the residual photoconductivity of the NC-BQ/PTZ complexes at excitation wavelengths of 400 nm and 480 nm, respectively. At both excitation wavelengths, the overall decay is faster in NC-BQ and NC-PTZ complexes compared to neat NCs.

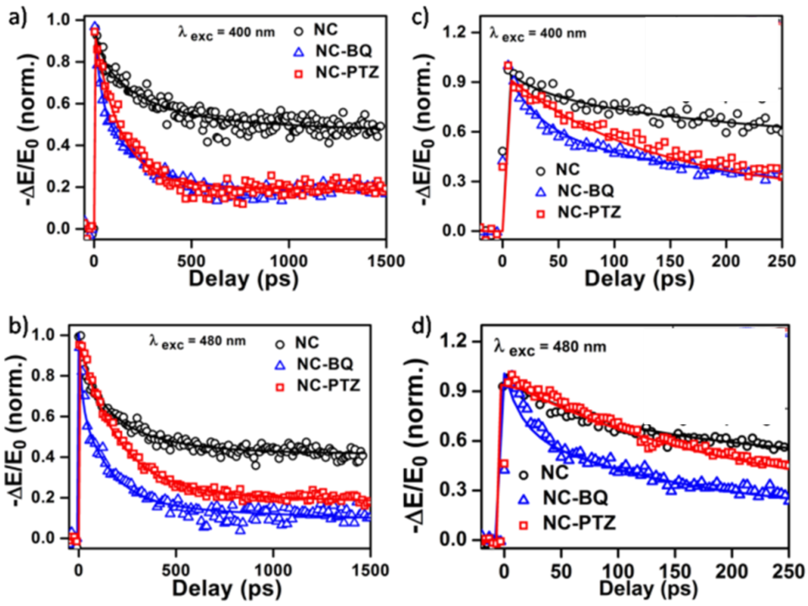

Figure 4.12. Normalized (to the maximum value) transient conductivity of neat NCs and normalized residual conductivity of NC-BQ/PTZ complexes when <N> =1.3 at a) λ_{exc} = 400 nm and b) λ_{exc} = 480 nm. Solid lines are multiexponential fits to the measured THz kinetics. c) and d) show the expanded view of the normalized decay till 250 ps. Insets of Figures c) and d) show the rise time of THz transients for neat NCs and NC-BQ/PTZ complexes at respective excitation wavelengths.

In neat NCs, three different recombination processes, namely inept monomolecular trap assisted recombination, bimolecular electron-hole recombination, and fast Auger recombination result in decrease in charge carrier density and thus conductivity in neat NCs with pump-probe delay.[6] However, in NC-BQ and NC-PTZ complexes the transient conductivity is dictated by any secondary electron/hole transfer (in addition to ultrafast hot carrier transfer discussed before) to the acceptor molecules (BQ/PTZ), back carrier transfer, along with carrier recombination (bimolecular recombination and trapping) within the NCs. We do not expect Auger process to take place as the residual carrier density after initial hot carrier transfer to acceptor molecules is quite small (<N> ~ 0.25 or less). Very weak fluence dependence of the THz kinetics in NC-BQ and NC-PTZ complexes (Figure 4.14) also point to the absence of Auger recombination.

To find out different decay components contributing to the overall kinetics, we have fitted the normalized photoconductivity transients to a multiexponential function convoluted with a Gaussian function of the form[54]:

$$y = G(t - t_0) \otimes \sum_i a_i \exp\left[-\frac{t - t_0}{\tau_i}\right] \qquad (9)$$

where $G(t - t_0)$ is a Gaussian function centered at t_0 with FWHM of ~300 fs which is also the instrument response function of our THz time resolved setup, and a_i is the coefficient of the i^{th} exponential decay channel with time constant τ_i. As mentioned earlier, the BQ and PTZ molecules form adsorption complex with NC surfaces governed by Langmuir adsorption isotherm. The NC-acceptor molecule adsorption complex formation is a stochastic process that follows Poissonian distribution. There should be equilibrium between adsorption and desorption of molecular acceptors on and off the NC surface. Hence, there may be a diffusion component. However, the time scale of the diffusion process is expected to be much slower compared to the dynamics probed in this study and should not affect the dynamics observed.

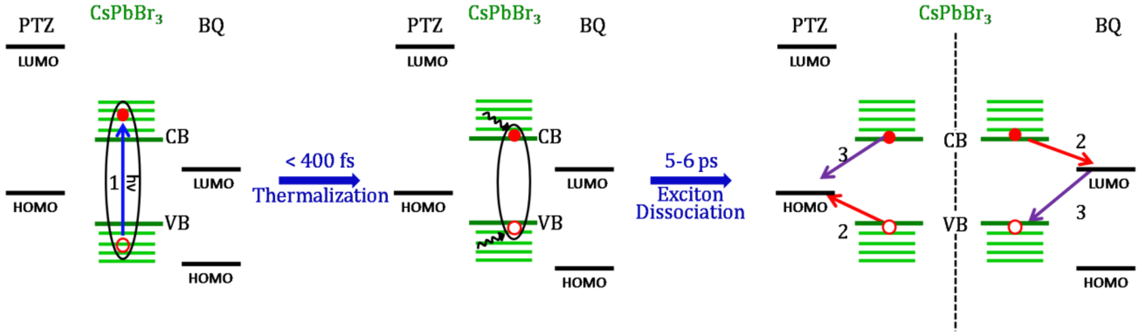

Figure 4.13. Schematic representation of possible mechanism of residual carrier transfer and charge recombination processes in CsPbBr$_3$ NC-BQ and NC-PTZ system upon photoexcitation. Fast (20-250 ps) thermalized carrier transfer. 1: photoexcitation, 2: thermalized e/h transfer, 3: back transfer.

THz transients were fitted using multiexponential decay function. For neat NCs we need biexponential decay function to fit the THz transients till 40 μJ/cm^2 and 90 μJ/cm^2 fluences for excitation at 400 nm and 480 nm, respectively. At fluences greater than 40 μJ/cm^2 for 400 nm excitation and 90 μJ/cm^2 for 480 nm excitation, we require triexponential decay function to fit the photoconductivity decay. Attempts to fit the THz transients varying the time constant for the slowest process from 1.5 ns to 8 ns[5] were unsuccessful. Thus, we kept τ_1 fixed at 15 ns (10 times of our temporal window) for fitting all THz transients in Figure 4.12, which gave reasonably good fit. Though we cannot estimate τ_1 with certainty due to the limitation of our temporal window, it certainly hints at inefficient mono-molecular trap assisted decay which is slower than the radiative PL decay. For NC-BQ complexes we need triexponential decay function while biexponential decay function was sufficient to fit the NC-PTZ decay. The parameters obtained by fitting the THz transients at different excitation wavelengths and different fluences are provided in Tables 4.4-4.9. Similar to the parent NCs, in BQ-NC and PTZ-NC complexes too we kept the monomolecular trapping process τ_1 fixed at 15 ns. This is justified as the slowest kinetics (600 ps and beyond) present in the conductivity transients for NC-BQ and NC-PTZ are very similar (parallel and independent of pump fluence) to that in neat NC. In both complexes, the contribution (a_1) from trap assisted recombination (τ_1) is much less compared to that observed for parent NCs. We presume that the available carriers for trapping get significantly reduced due to alternative transfer pathways in presence of acceptor molecules, thereby, decreasing the contribution of trap assisted recombination. At 400 nm excitation, τ_3 component in BQ-NC complexes is ~ 30-50 ps and the τ_2 component is ~ 200-250 ps. We attribute the τ_3 component to a secondary transfer process of thermalized electrons (process 2 in Figure 4.13). The second component (τ_2) may be a convolution of electron hole recombination within the NCs and recombination of electrons that are back transferred from the BQ to the NCs with the holes in the NCs (process 3 in Figure 4.13). In NC-PTZ complex, the only decay component (τ_2 ~137-166 ps) other than trapping (τ_1) is probably the convolution of thermalized hole transfer from NC to PTZ (process 2 in Figure 4.13), back transfer from PTZ (process 3 in Figure 4.13) and electron-hole recombination within the NCs.

Table 4.4. Parameters obtained from fitting the normalized THz transients of neat NCs to equation 9 when excited using 480 nm pump wavelength.

Fluence (μJ/cm^2)	<N>	a_1	τ_1 (ps)	a_2	τ_2 (ps)	a_3	τ_3 (ps)
24.9	0.34	0.60 (0.001)	15000	0.25 (0.001)	178.2 (1)	..	..

39.5	0.6	0.56 (0.001)	15000	0.37 (0.001)	162.8 (0.4)	..	..
72.7	1.1	0.49 (0.00)	15000	0.46 (0.001)	159.2 (0.2)	..	..
93.5	1.42	0.38 (0.00)	15000	0.44 (0.001)	183.4 (0.3)	0.20 (0.001)	25.3 (0.2)
114.3	1.74	0.28 (0.00)	15000	0.50 (0.001)	153.6 (0.02)	0.21 (0.001)	19.8 (0.2)
135.1	2.04	0.26 (0.00)	15000	0.44 (0.001)	157.7 (0.2)	0.26 (0.001)	23.2 (0.1)
166.3	2.51	0.25 (0.00)	15000	0.44 (0.001)	167.7 (0.2)	0.29 (0.001)	24.1 (0.1)

Table 4.5. Parameters obtained by fitting the THz transients of NC-BQ complexes to equation 9 when excited using 480 nm pump wavelength.

Fluence (μJ/cm^2)	<N>	a_1	τ_1 (ps)	a_2	τ_2 (ps)	a_3	τ_3 (ps)
51.5	0.72	0.17 (0.00)	15000	0.64 (0.001)	145.36 (0.43)	0.109 (0.002)	15.98 (0.82)
74.7	1.05	0.142 (0.00)	15000	0.66 (0.002)	130.14 (0.50)	0.126 (0.003)	18.774 (0.91)
90.9	1.27	0.126 (0.00)	15000	0.518 (0.001)	185.56 (0.45)	0.359 (0.001)	25.84 (0.20)
111.22	1.56	0.14 (0.00)	15000	0.56 (0.001)	168.68 (0.25)	0.3 (0.00)	26.42 (0.21)

Table 4.6. Parameters obtained by fitting the THz transients of NC-PTZ complexes to equation 9 when excited using 480 nm pump wavelength.

Fluence (μJ/cm^2)	<N>	a_1	τ_1(ps)	a_2	τ_2(ps)
38.1	0.54	0.22 (0.00)	15000	0.77 (0.00)	196 (0.31)
66.1	0.93	0.218 (0.00)	15000	0.74 (0.00)	225 (0.20)
78.2	1.1	0.19 (0.00)	15000	0.77 (0.001)	236.25 (0.16)
90.2	1.27	0.21 (0.00)	15000	0.78 (0.00)	202.86 (0.20)

Table 4.7. Parameters obtained by fitting the THz transients of neat NCs to equation 9 when excited using 400 nm pump wavelength.

Fluence (μJ/cm^2)	<N>	a_1	τ_1 (ps)	a_2	τ_2 (ps)	a_3	τ_3 (ps)
41	1.03	0.62 (0.001)	15000	0.27 (0.001)	209.7 (0.9)		
57	1.42	0.53 (0.00)	15000	0.32 (0.001)	234.8 (0.9)	0.13 (0.001)	32.9 (0.7)
72	1.8	0.49 (0.00)	15000	0.36 (0.001)	214.0 (0.5)	0.14 (0.001)	22.9 (0.3)
94	2.34	0.46 (0.00)	15000	0.37 (0.001)	214.4 (0.5)	0.18 (0.001)	32.2 (0.3)

Table 4.8. Parameters obtained by fitting the THz transients of NC-BQ to equation 9 when excited using 400 nm pump wavelength.

Fluence (μJ/cm^2)	<N>	a_1	τ_1(ps)	a_2	τ_2(ps)	a_3	τ_3(ps)
41.5	0.96	0.25 (0.00)	15000	0.38 (0.002)	220 (1.35)	0.3 (0.002)	40 (0.56)
56.9	1.3	0.19 (0.00)	15000	0.41 (0.001)	204.7 (0.60)	0.32 (0.001)	29.42 (0.23)
71.9	1.67	0.22 (0.00)	15000	0.35 (0.001)	239.03 (0.77)	0.36 (0.001)	48.62 (0.26)
83.1	1.9	0.23 (0.00)	15000	0.43 (0.00)	250 (0.00)	0.30 (0.001)	28.7 (0.12)

Table 4.9. Parameters obtained by fitting the THz transients of NC-PTZ to equation 8 when excited using 400 nm pump wavelength.

Fluence (μJ/cm^2)	<N>	a_1	τ_1 (ps)	a_2	τ_2 (ps)
41.5	0.96	0.21 (0.00)	15000	0.73 (0.001)	137.27 (0.22)
56.9	1.32	0.19 (0.00)	15000	0.72 (0.00)	156.31 (0.15)
71.9	1.67	0.206 (0.00)	15000	0.75 (0.00)	166.27 (0.17)

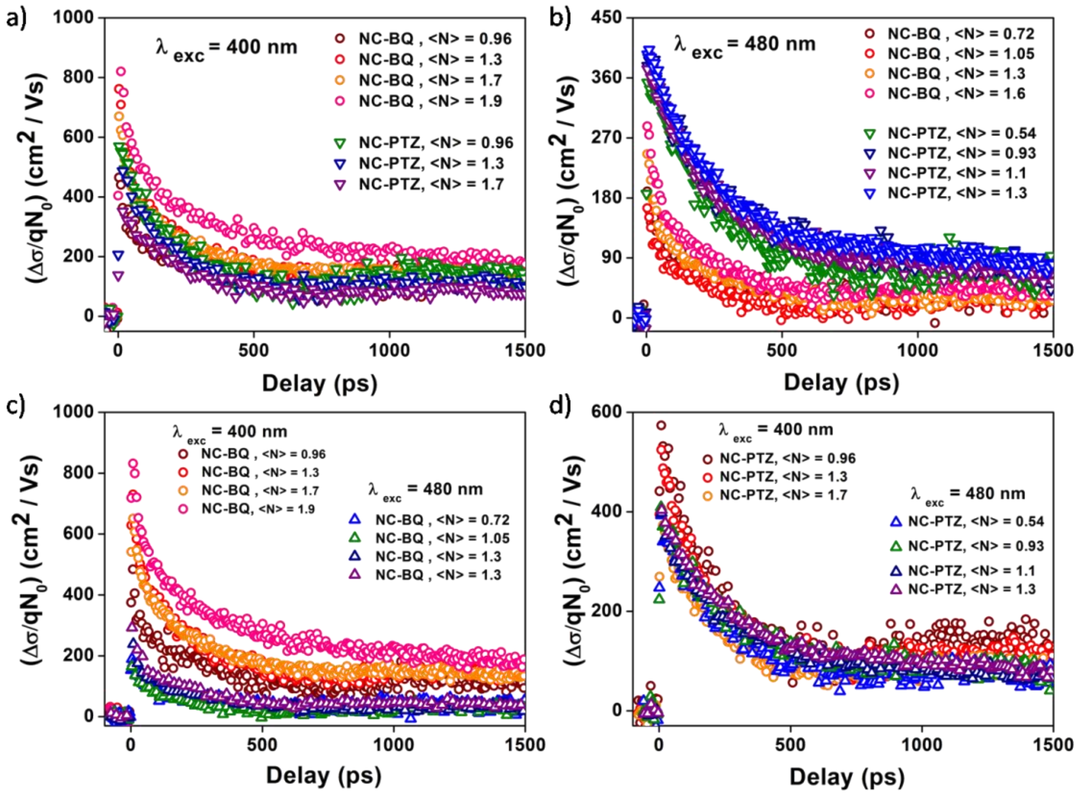

Figure 4.14. a) Conductivity normalized with respect to initial carrier density (N$_0$) at different <N> for NC-BQ and NC-PTZ complexes when a) λ_{exc} = 400 nm and b) λ_{exc} = 480 nm. Normalized conductivity with respect to N$_0$ for c) NC-BQ and d) NC-PTZ complexes.

At λ_{exc} = 480 nm, for NC-BQ complex, the decay becomes faster with τ_2 and τ_3 values of ~130-185 and ~16-26 ps respectively. However, in case of NC-PTZ complex, τ_2 (~196-236) becomes slower at 480 nm pump. We do not observe any strong fluence dependence of the THz kinetics in NC-BQ/PTZ complexes (see Figure 4.14 a,b). However, the initial THz photoconductivity appears to be dependent on pump wavelength (Figure 4.14 c,d). The initial signal size for NC-BQ complex is more than that of NC-PTZ complex when excited using 400 nm pump. In case of 480 nm excitation, NC-PTZ complex shows greater initial signal than NC-BQ complex. Overall, the quenching in conductivity is higher for 480 nm excitation which indicates more efficient initial carrier transfer (also, see Table 4.1). A possible reason for this observation could be a better coupling between the resulting hot states and the molecular wave functions at 480 nm excitation.

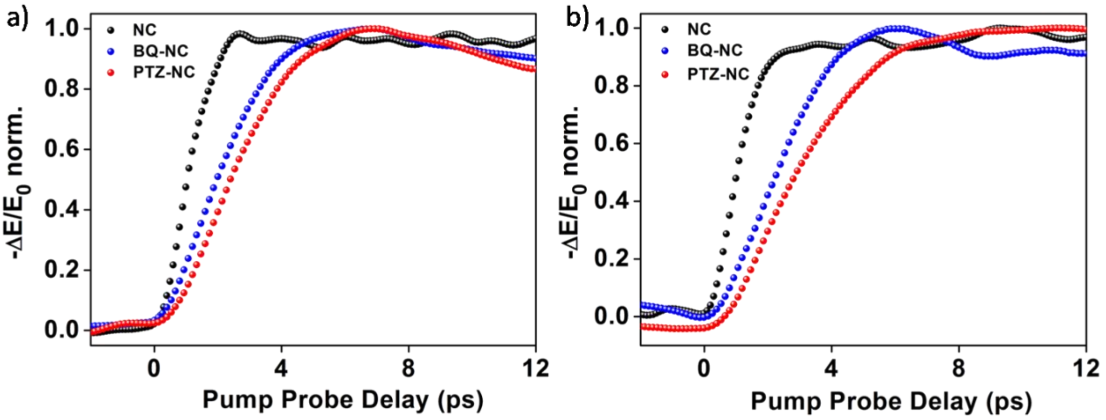

Figure 4.15. Initial THz kinetics for neat NC, NC-BQ and NC-PTZ complexes at a) λ_{exc} = 400 nm and b) λ_{exc} = 480 nm when <N> ~ 1.3.

An expanded view of very early initial dynamics is shown in Figures 4.15a and 4.15b. Initial THz kinetics reveals a rise time of ~3.5 ps in neat NCs and slower rise time of ~ 6-7 ps in both NC-BQ and NC-PTZ complexes. This rise time is indicative of dissociation of the remaining excitons into mobile charge carriers after initial ultrafast transfer of carriers in the presence of acceptor molecules. A longer exciton dissociation time in the presence of molecular acceptors may seem to be counterintuitive. In the presence of an ultrafast electron/hole transfer process, one would expect faster exciton dissociation. Here those excitons are involved that did not undergo ultrafast (sub-300 fs) transfer to the acceptor molecules. These (~ 10-30 %) are responsible for the residual conductivity observed in NC-BQ and NC-PTZ complexes. These excitons thermalize to the band edge in 300-700 fs prior to dissociation (6-7 ps) to produce free carriers that contribute to the photoinduced real conductivity in our time-resolved THz experiments. We propose two plausible mechanisms to explain the observation of slower exciton dissociation time in NC-BQ/PTZ complexes. 1) There may be a major difference in exciton binding energy in NC-BQ/PTZ complex compared to exciton binding energy in neat NCs. The dielectric constant of the photoexcited NCs may alter significantly in the presence of the acceptor molecules. The exciton binding energy is inversely proportional to the dielectric constant as a higher dielectric constant will screen the Coulombic attraction between electron and hole. Previously Juarez-Perez *et al.* reported photoinduced giant dielectric constant (GDC) of $CH_3NH_3PbX_3$ perovskites.[55] The enhancement in low frequency real dielectric constant (DC) upon photoexcitation is as high as ~1000 times under one sun intensity. The photoinduced DC shows a nearly linear dependence on the photo injected carrier density (intensity of photoexcitation). We anticipate that $CsPbBr_3$ NCs may also have similar photoinduced dielectric properties. In the presence of BQ/PTZ, 70-90% of photo generated carriers are transferred to the molecular acceptors at a sub-300 fs time scale, reducing the effective carrier density significantly. This reduction in carrier density should significantly decrease the DC in the NC-molecule complexes compared to that in photoexcited neat NCs. Thus, the remaining excitons (which eventually give rise to the residual photoconductivity) experience less dielectric screening and exhibit higher exciton binding energy. 2) Secondly, the presence of the acceptor molecules (BQ/PTZ) may reduce the lattice temperature compared to that in neat NCs which might contribute to slower exciton dissociation in NC-BQ/PTZ complexes. In neat NCs every photogenerated hot exciton eventually relaxes to the band edge through a multi-phonon absorption. The excess energy dumped on to the lattice increases the lattice temperature significantly. However, in the presence of BQ and PTZ, the majority (70-90%) of the hot carriers are transferred to the molecular acceptors prior to thermalization. Only a small fraction (10-30%) of the carriers is thermalized. Hence, the lattice temperature should be lower than that in case of the neat NCs.

We observe hot carrier transfer in $CsPbBr_3$ NCs in presence of acceptors which is not the outcome of phonon bottleneck as observed by Yang *et al.* in thin films of $CH_3NH_3PbI_3$ at high carrier density.[56] This is indeed encouraging news for realizing high-efficiency photovoltaics using these materials. Very recently solar cell fabricated using $CsPbBr_3$ NCs showed a high open-circuit voltage of ~ 1.5 V.[10]This might be an indication of hot carrier extraction from these NCs. We anticipate that similar carrier transfer kinetics will prevail in $CsPbI_3$ and $CsPb(Br/I)_3$ NCs that have more suitable band gap for solar cell application. The overall nature of the carrier transfer and recombination processes in a device architecture employing NC thin film interface is expected to remain similar. One needs to perform such time resolved THz measurements at the interface of NC film-bulk carrier transport layer material to gain more realistic insight. In such scenario, the THz measurements will have a contribution from carriers in both NC film and the transport material. Deconvolution of the individual contribution may not be trivial unless they are studied separately. Studying TRTS of NC-molecule interface reveal the response from the NCs eliminating the contribution from the molecule. Having understood this system one would be in better position to understand the dynamics in bulk NC/interface that is used in a photovoltaic function.

4.4 Conclusion

Utilizing time resolved THz spectroscopy, we studied the photogenerated interfacial electron and hole transfer from $CsPbBr_3$ perovskite NCs to BQ and PTZ molecules at excitation conditions leading to average electron-hole pairs per NC in the range of 0.54 - 1.91. We observe two different types of carrier transfer processes. Hot carriers are transferred to the molecular acceptors in sub-300 fs time scale, which is limited by our IRF. These carrier transfer rates are orders of magnitude faster than the Auger recombination (20-40 ps), an aggressive loss mechanism for photovoltaics. However, an equally fast charge recombination accompanies the carrier transfer events. A secondary transfer of thermalized electrons and holes is also observed with characteristic time constants of 30-50 ps and 196-250 ps, respectively. A suitable method of reducing the ultrafast charge recombination due to back transfer process would allow extracting the hot carriers, thus improving the photovoltaic and photocatalytic efficiencies. We also propose that the exciton binding energies in NC-BQ/PTZ complexes are different from the exciton binding energy in neat NCs which is responsible for a slower exciton dissociation time in NC-BQ/PTZ complex compared to exciton binding energy in neat NCs.

4.5 References

(1) Protesescu, L.; Yakunin, S.; Bodnarchuk, M. I.; Krieg, F.; Caputo, R.; Hendon, C. H.; Yang,R. X.; Walsh, A.; Kovalenko, M. V. *Nano Lett.* **2015**, *15*, 3692-3696.
(2) Protesescu, L.; Yakunin, S.; Bodnarchuk, M. I.; Krieg, F.; Caputo, R.; Hendon, C. H.; Yang,R. X.; Walsh, A.; Kovalenko, M. V. *Nano Lett.* **2015**, *15*, 3692-3696.
(3) Wang, Y.; Li, X.; Zhao, X.; Xiao, L.; Zeng, H.; Sun, H. *Nano Lett.* **2016**, *16*, 448-453.
(4) Wang, Y.; Li, X.; Song, J.; Xiao, L.; Zeng, H.; Sun, H. *Adv. Mater.* **2015**, *27*, 7101-7108
(5) Swarnkar, A.; Chulliyil, R.; Ravi, V. K.; Irfanullah, M.; Chowdhury, A.; Nag, A. *Angew.Chem., Int. Ed.* **2015**, *54*, 15424-15428.
(6) Yettapu, G. R.; Talukdar, D.; Sarkar, S.; Swarnkar, A.; Nag, A.; Ghosh, P.; Mandal, P. *NanoLett.* **2016**, *16*, 4838-4848.
(7) Zhang, X.; Lin, H.; Huang, H.; Reckmeier, C.; Zhang, Y.; Choy, W. C. H.; Rogach, A. L. *Nano Lett.* **2016**, *16*, 1415-1420.
(8) Li, G.; Rivarola, F. W. R.; Davis, N. J. L. K.; Bai, S.; Jellicoe, T. C.; de la Pena, F.; Hou, S.;Ducati, C.; Gao, F.; Friend, R. H.; Greenham, N. C.; Tan, Z.-K. *Adv. Mater.* **2016**, *28*, 35283534.
(9) Song, J.; Li, J.; Li, X.; Xu, L.; Dong, Y.; Zeng, H. *Adv. Mater.* **2015**, *27*, 7162-7167.

(10) Akkerman, Q. A.; Gandini, M.; Di Stasio, F.; Rastogi, P.; Palazon, F.; Bertoni, G.; Ball, J.M.; Prato, M.; Petrozza, A.; Manna, L. *Nat. Energy* **2016**, *2*, 16194.
(11) Swarnkar, A.; Marshall, A. R.; Sanehira, E. M.; Chernomordik, B. D.; Moore, D. T.;Christians, J. A.; Chakrabarti, T.; Luther, J. M. *Science* **2016**, *354*, 92-95.
(12) Xu, Y.-F.; Yang, M.-Z.; Chen, B.-X.; Wang, X.-D.; Chen, H.-Y.; Kuang, D.-B.; Su, C.-Y. *J.Am. Chem. Soc.* **2017**, *139*, 5660-5663.
(13) Tisdale, W. A.; Williams, K. J.; Timp, B. A.; Norris, D. J.; Aydil, E. S.; Zhu, X.-Y. *Science***2010**, *328*, 1543-1547.
(14) Nozik, A. J. *Annu. Rev. Phys. Chem.* **2001**, *52*, 193-231.
(15) Pandey, A.; Guyot-Sionnest, P. *Science***2008**, *322*, 929-932.
(16) Zhu, H.; Yang, Y.; Wu, K.; Lian, T. *Annu. Rev. Phys. Chem.* **2016**, *67*, 259-281.
(17) Manser, J. S.; Kamat, P. V. *Nat Photon* **2014**, *8*, 737-743.
(18) Beard, M. C.; Turner, G. M.; Schmuttenmaer, C. A. *J. Phys. Chem. B* **2002**, *106*, 7146-7159.
(19) Ulbricht, R.; Hendry, E.; Shan, J.; Heinz, T. F.; Bonn, M. *Rev. Mod. Phys* **2011**, *83*, 543-586.
(20) Schmuttenmaer, C. A. *Chem. Rev.***2004**, *104*, 1759-1780.
(21) Wu, K.; Liang, G.; Shang, Q.; Ren, Y.; Kong, D.; Lian, T. *J. Am. Chem. Soc.* **2015**, *137*,12792-12795.
(22) Maity, P.; Dana, J.; Ghosh, H. N. *J. Phys. Chem. C* **2016**, *120*, 18348-18354.
(23) Morris-Cohen, A. J.; Vasilenko, V.; Amin, V. A.; Reuter, M. G.; Weiss, E. A. *ACS Nano* **2012**, *6*, 557-565.
(24) Wu, K.; Du, Y.; Tang, H.; Chen, Z.; Lian, T. *J. Am. Chem. Soc.* **2015**, *137*, 10224-10230.
(25) Morris-Cohen, A. J.; Frederick, M. T.; Cass, L. C.; Weiss, E. A. *J. Am. Chem. Soc.* **2011**,*133*, 10146-10154.
(26) Makarov, N. S.; Guo, S.; Isaienko, O.; Liu, W.; Robel, I.; Klimov, V. I. *Nano Lett.* **2016**, *16*,2349-2362.
(27) Khamooshi, M.; Salati, H.; Egelioglu, F.; Hooshyar Faghiri, A.; Tarabishi, J.; Babadi, S. *Int.J. Photoenergy* **2014**, *2014*, 17.
(28) Perez-Higueras, P.; Munoz, E.; Almonacid, G.; Vidal, P. G. *Renew. Sustainable Energy Rev.* **2011**, *15*, 1810-1815.
(29) Beard, M. C. *J. Phys. Chem. Lett.* **2011**, *2*, 1282-1288.
(30) Beard, M. C.; Luther, J. M.; Semonin, O. E.; Nozik, A. J. *Acc. Chem. Res* **2013**, *46*, 1252-1260.
(31) G.Zoski, C. *Handbook of Electrochemistry*, 2007.
(32) Harris, R. D.; Amin, V. A.; Lau, B.; Weiss, E. A. *ACS Nano***2016**, *10*, 1395-1403.
(33) Hens, Z.; Martins, J. C. Chem. Mater.**2013**, *25*, 1211-1221.
(34) Iwaszczuk, K.; Cooke, D. G.; Fujiwara, M.; Hashimoto, H.; Jepsen, P. U. *Opt. Express***2009**, *17*, 21969-21976.
(35) Mandal, P. K.; Chikan, V. *Nano Lett.***2007**, *7*, 2521-2528.
(36) Ravi, V. K.; Markad, G. B.; Nag, A. *ACS Energy Lett.* **2016**, *1*, 665-671.
(37) Wehrenfennig, C.; Liu, M.; Snaith, H. J.; Johnston, M. B.; Herz, L. M. *Energy Environ Sci.***2014**, *7*, 2269-2275.
(38) Ponseca, C. S.; Hutter, E. M.; Piatkowski, P.; Cohen, B.; Pascher, T.; Douhal, A.; Yartsev,A.; Sundstrom, V.; Savenije, T. J. *J. Am. Chem. Soc.* **2015**, *137*, 16043-16048.
(39) Zhu, H.; Yang, Y.; Hyeon-Deuk, K.; Califano, M.; Song, N.; Wang, Y.; Zhang, W.;Prezhdo, O. V.; Lian, T. *Nano Lett.* **2014**, *14*, 1263-1269.
(40) Smith, N. V. *Phys. Rev. B,***2001**, *64*, 155106.
(41) Kar, S.; Jayanthi, S.; Freysz, E.; Sood, A. K. *Carbon* **2014**, *80*, 762-770.

(42) Lloyd-Hughes, J.; Jeon, T.-I. *J. Infrared Millim. Terahertz Waves* **2012**, *33*, 871-925.
(43) La-o-vorakiat, C.; Xia, H.; Kadro, J.; Salim, T.; Zhao, D.; Ahmed, T.; Lam, Y. M.; Zhu, J.-X.; Marcus, R. A.; Michel-Beyerle, M.-E.; Chia, E. E. M. *J. Phys. Chem. Lett.* **2016**, *7*, 1-6.

(44) Butler, K. T.; Dringoli, B. J.; Zhou, L.; Rao, P. M.; Walsh, A.; Titova, L. V. *J. Mater. Chem. A* **2016**, *4*, 18516-18523.

(45) Stoumpos, C. C.; Malliakas, C. D.; Peters, J. A.; Liu, Z.; Sebastian, M.; Im, J.; Chasapis, T. C.; Wibowo, A. C.; Chung, D. Y.; Freeman, A. J.; Wessels, B. W.; Kanatzidis, M. G. *Cryst. Growth Des.***2013**, *13*, 2722-2727.

(46) Wehrenfennig, C.; Eperon, G. E.; Johnston, M. B.; Snaith, H. J.; Herz, L. M. *Adv. Mater.***2014**, *26*, 1584-1589.
(47) Karakus, M.; Jensen, S. A.; D'Angelo, F.; Turchinovich, D.; Bonn, M.; Cánovas, E. *J. Phys. Chem. Lett.* **2015**, *6*, 4991-4996.
(48) Milot, R. L.; Eperon, G. E.; Snaith, H. J.; Johnston, M. B.; Herz, L. M. *Adv. Funct. Mater.***2015**, *25*, 6218-6227.
(49) Mondal, N.; Samanta, A. *Nanoscale* **2017**, *9*, 1878-1885.
(50) Chung, H.; Jung, S. I.; Kim, H. J.; Cha, W.; Sim, E.; Kim, D.; Koh, W.-K.; Kim, J. *Angew.Chem., Int. Ed.* **2017**, *56*, 4160-4164.
(51) Aneesh, J.; Swarnkar, A.; Kumar Ravi, V.; Sharma, R.; Nag, A.; Adarsh, K. V. *J. Phys.Chem. C* **2017**, *121*, 4734-4739.
(52) Williams, K. J.; Nelson, C. A.; Yan, X.; Li, L.-S.; Zhu, X. *ACS Nano***2013**, *7*, 1388-1394.
(53) Žídek, K.; Zheng, K.; Ponseca, C. S.; Messing, M. E.; Wallenberg, L. R.; Chabera, P.;Abdellah, M.; Sundstrom, V.; Pullerits, T. *J. Am. Chem. Soc.* **2012**, *134*, 12110-12117.
(54) Beard, M. C.; Turner, G. M.; Schmuttenmaer, C. A. *Nano Lett.***2002**, *2*, 983-987.
(55) Juarez-Perez, E. J.; Sanchez, R. S.; Badia, L.; Garcia-Belmonte, G.; Kang, Y. S.; Mora-Sero, I.; Bisquert, J. *J. Phys. Chem. Lett.***2014**, *5*, 2390-2394.
(56) Park, Y.-S.; Bae, W. K.; Baker, T.; Lim, J.; Klimov, V. I. *Nano Lett.***2015**, *15*, 7319-7328.

Chapter 5

Effect of Capping Ligand Engineering on Carrier Dynamics in CsPbI$_3$ Nanocrystals

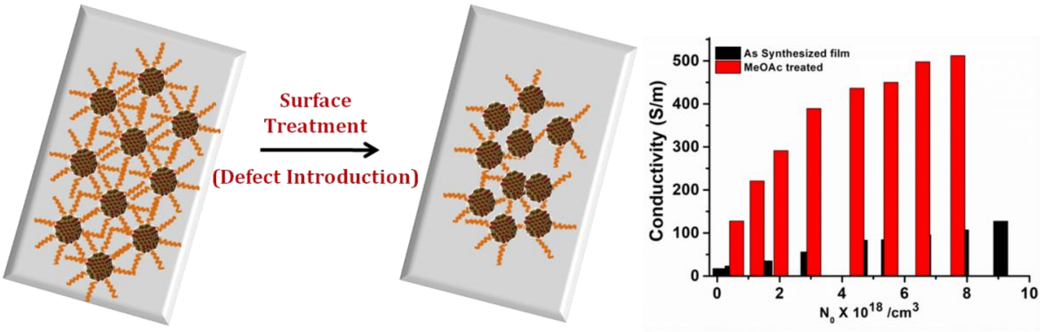

5.1 Introduction:

Hybrid organic inorganic perovskites with the general formula ABX_3 where A is an organic cation, B is usually Pb^{2+} and X is a halide have garnered tremendous interest from the scientific community due to their magnificent optoelectronic properties,[1-7] the most significant one being the photovoltaic power conversion efficiency of more than 20%,[8-10] using methylammonium-lead-triiodide as the photoactive material.[11] However, under environmental stress, the volatile organic component tends to dissociate producing CH_3NH_3I and PbI_2, which jeopardize the robustness of the devices made out of them.[12] All inorganic $CsPbX_3$ show promising features to be used in optoelectronic devices and are prospective alternatives of their forerunner hybrid organic inorganic perovskites, since they are more temperature and moisture resistant.[13,14]

Prompted by an electron mobility of ~ 1000 cm^2/(V·s) and a lifetime of 2.5 μs of a single crystal of $CsPbBr_3$,[15] Kulbak *et al.* fabricated solar cell using $CsPbBr_3$ that showed performance equivalent to $CH_3NH_3PbI_3$.[13] Nevertheless, $CsPbBr_3$ yields lower photocurrent due to a higher bandgap of $\sim$ 2.36 eV.[13] Although cubic (α) $CsPbI_3$ has a more suitable band gap of 1.73 eV for solar radiation absorption, the photoactive cubic perovskite phase is stable only at temperatures above 315^{0}C. At lower temperature, it forms the orthorhombic (δ) phase, which has a much higher bandgap of 2.83 eV.[16] Snaith and co-workers reported, for the first time, working solar cell made of all inorganic α-$CsPbI_3$ at room temperature displaying a power conversion efficiency of 1.7 %.[14] Yet the cubic phase instability of $CsPbI_3$ at room temperature is a bottleneck to using it for solar cell fabrication. Subsequently, much endeavour has been put to fabricate solar cells with mixed cations (Cs and formamidinium) or mixed halides (Br/I) or both that will retain the photoactive cubic phase at room temperature and show greater moisture and temperature durability.[17-23] In a very recent study, Hutter *et al.* employed time resolved microwave conductivity (TRMC) technique to study the carrier mobilities and lifetimes of vapour deposited and spin coated cubic phase polycrystalline $CsPbI_3$ thin films. They reported the charge carrier mobilities up to 25 cm^2/(Vs) and long carrier lifetimes, greater than 10 μs, for vapour deposited $CsPbI_3$. On the contrary, the carrier lifetime measured for the spin coated sample was less than 0.2 μs. A device fabricated using $CsPbI_3$ showed power conversion efficiency close to 9 %.[24] However, to prevent the conversion of black coloured cubic $CsPbI_3$ to yellow orthorhombic phase, they conducted the optoelectronic characterization in an inert atmosphere.

Kovalenko and co-workers[25] pioneered the synthesis of colloidal $CsPbX_3$ NCs which display enhanced cubic phase stability at room temperature and find applications in light emitting diodes,[26-28] photovoltaics (PV),[29,30] and photocatalysis[31] due to their alluring optical properties.[25] But preceding studies could not accomplish reasonably stable α-$CsPbI_3$ NCs to be used in photovoltaics. Swarnkar *et al*. improvised the synthetic method and isolation procedure of $CsPbI_3$ NCs that helped the NCs retain their cubic phase under ambient condition for months and could be used for PV characterization.[30] Already a promising power conversion efficiency of 10 % has been shown by device fabricated using these cubic $CsPbI_3$ NCs. They further treated the NC films with methyl acetate (MeOAc) and lead acetate ($Pb(OAc)_2$) dissolved in methyl acetate to remove the insulating oleylamine capping ligand and produce electronically conductive films.[30]

Understanding the photophysics of α-phase $CsPbI_3$ NCs is yet evolving and various time resolved spectroscopic techniques are being employed for this. Makarov *et al.* did a thorough study of $CsPbX_3$ NCs utilizing transient absorption (TA) and photoluminescence (PL) spectroscopy and reported fast Auger recombination occurring within ~ 20- 200 ps time scale.[32] Hu *et al.* showed nonblinking PL in single $CsPbI_3$ NCs at room and cryogenic temperatures, which they ascribed to missing defect states for band edge carriers to form charged excitons. They further reported reduced Auger recombination of trions but could not pin point the reason behind it.[33] From TA and PL study of $CsPbI_3$ NCs dispersed in toluene, Mondal *et al*. assigned 0.56 ps, ~ 250 ps and > 2000 ps to hot exciton relaxation, trapping and recombination mechanisms, respectively.[34] They rule out the possibility of any Auger recombination due to low excitation density used for TA experiments. Yet in another TA study of $CsPbI_3$ NCs by Liu *et al*., a 23 ps time scale has been assigned to Auger recombination.[35]

Time resolved Terahertz Spectroscopy (TRTS) is a non-contact technique with subpicosecond temporal resolution for measuring transient local ac photoconductivity and provides insights into carrier dynamics.[36] In this work, we have utilized time-domain THz spectroscopy (THz-TDS) and TRTS, for the first time, to study the α phase stable $CsPbI_3$ NC film under ambient condition. As already mentioned above, for efficient use of the NC films in optoelectronic devices, they need to be made electronically conductive which is achieved by removal of the insulating capping agents. Using TRTS we want to understand, how removal of the capping ligands affect the conductivities and mobilities of these NCs. Hence, we have studied the films of NCs after treating them with MeOAc and $Pb(OAc)_2$. We certainly observe an increased conductivity of the films when treated with MeOAc and $Pb(OAc)_2$. We reckon that washing the NC surface lead to ligand removal that enhances dot-to-dot conduction along with increasing the number of dangling bonds paving a pathway for fast trapping, which is manifested as a faster recombination pathway occurring in the time scales of ~ 20-40 ps.

5.2 Synthesis and characterization of colloidal $CsPbI_3$ nanocrystals (NCs):

5.2.1 Preparation of Colloidal $CsPbI_3$ NCs: Cubic $CsPbI_3$ NCs were synthesized and characterized by Abhishek Swarnkar from Dr. Angshuman Nag's Group. $CsPbI_3$ NCs were synthesized following a similar procedure reported by Protesescu *et al.*[25] with some improvisations. He prepared the thin films of $CsPbI_3$ NCs and treated them with MeOAc and $Pb(OAc)_2$.

5.2.2 Preparation of Cs-oleate: Cesium carbonate (0.5 g), oleic acid (2 mL), and 1-octadecene (20 mL) were loaded in a 100 mL three necked flask and the mixture was heated at 120^0C for 30 minutes under vacuum along with magnetic stirring, followed by purging with nitrogen for 10 min. This process of alternately applying vacuum and N_2 purging was repeated thrice to remove moisture and oxygen from the reaction mixture. When Cs_2CO_3 dissolved completely to give a clear solution, the reaction was considered complete. Cs-oleate in 1-octadecene was stored in N_2 atmosphere until required for NC synthesis.

5.2.3 Synthesis of Colloidal $CsPbI_3$ NCs: PbI_2 (1 g) and 50 ml 1-octadecene were stirred in a 500 mL round bottomed flask and degassed at 120^0 C under vacuum for 1 hour. Then the flask was kept under continuous N_2 flow. 5 ml of oleic acid and oleylamine, pre-heated at ~ 70^0 C, were injected into the flask. The flask was again placed under vacuum till complete dissolution of PbI_2. Once the solution became clear, the temperature was raised to 180 °C for 9 nm NCs. Separately prepared Cs-oleate solution (~0.0625 M, 8 mL), preheated to 70^0C under inert atmosphere, was swiftly injected into the reaction mixture. The reaction mixture turned dark red and was quenched after 5 sec by dipping the reaction mixture in ice bath.

5.2.4 Isolation of colloidal $CsPbI_3$ NCs: $CsPbI_3$ NCs are ionic in nature and is a soft base while oleylammonium ligand is a hard acid. This leads to a weaker acid base interaction and consequently extraction of $CsPbI_3$ NCs become difficult. Thus, conventional polar non-solvents like 1-butanol, acetone, and ethyl acetate used to wash NCs from reaction solutions could not be used since they caused phase reversal to the orthorhombic phase due to agglomeration or simply re-dissolution of the $CsPbI_3$ NCs. MeOAc could successfully extract cubic phase $CsPbI_3$ NCs. By adding 200 mL of MeOAc to reaction mixture, the synthesized $CsPbI_3$ NCs were precipitated (ratio of NC reaction mixture:MeOAc is 1:3) and then centrifuged at 8000 RPM for 5 min. The centrifuged NCs were redispersed in 3 mL hexane, precipitated again with an equal volume of MeOAc and centrifuged at 8000 RPM for 2 min. The amount of MeOAc added is very crucial since excess addition leads to surface ligand removal and agglomeration to orthorhombic phase. Excess PbI_2 and Cs-oleate were removed by dispersing the NCs in 20 mL of hexane and centrifuging again at 4000 RPM for 5 min. By keeping the solution of colloidal $CsPbI_3$ NCs in the dark at 4 °C for 48 hours, the excess Cs-oleate and Pb-oleate, which solidify at low temperatures, were precipitated out. Before using, the NC solution was decanted and centrifuged again at 4000 RPM for 5 min. To use the NC solution for making films, the hexane was dried and the NCs were dissolved in octane at a concentration of ~50 mg/ml.

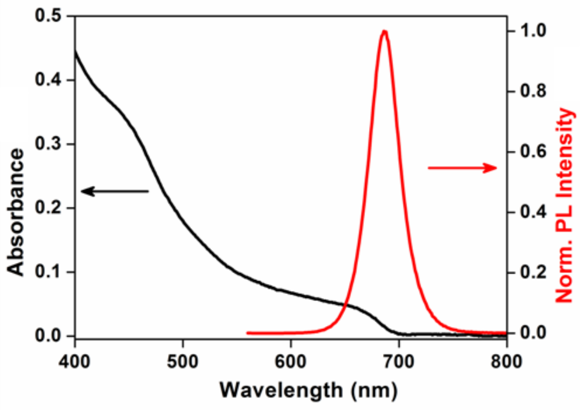

Figure 5.1 UV-visible absorption and photoluminescence (PL) spectra of colloidal $CsPbI_3$ NCs.

5.2.5 Powder x-ray diffraction (PXRD) data were recorded by a Bruker D8 Advance x-ray diffractometer using Cu Kα radiation (1.54 Å).

5.2.6 Transmission electron microscopy (TEM) studies were carried out using a JEOL JEM 2100 F field emission transmission electron microscope at 200 kV. The sample preparation for TEM was done by putting a drop of the colloidal solution of NCs in hexane on the carbon coated copper grids. Powder X-ray diffraction pattern confirming that cubic phase $CsPbI_3$ NCs are formed and their TEM image are shown in Figure 5.2.

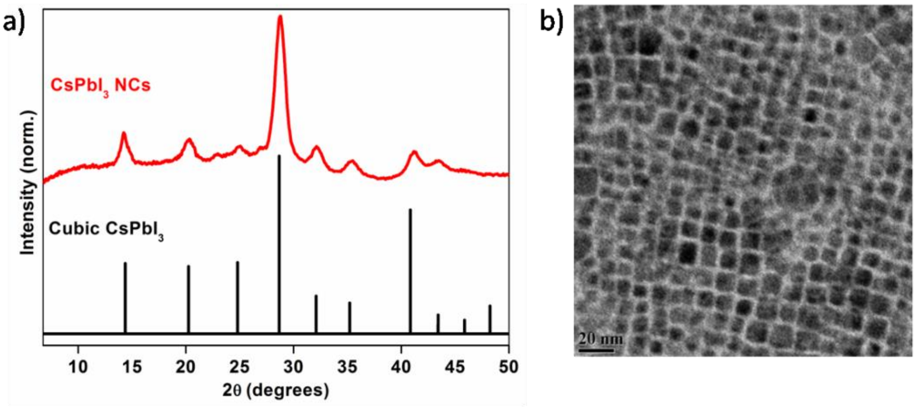

Figure 5.2 a) Powder XRD pattern of $CsPbI_3$ NC with reference to XRD peaks of cubic phase $CsPbI_3$. b) TEM image of $CsPbI_3$ NCs of size 9 ± 1.5 nm synthesized at 180 °C.

5.2.7 Film Fabrication: For TRTS experiments, we fabricated thin films of the NCs on high density polyethylene (HDPE) substrate. The NCs (~50 mg/mL in octane) were spin-cast on HDPE substrate at 1000 RPM for 20 sec followed by 2000 RPM for 5 sec. Three similar films were made. One film was kept without any treatment. Another film was dipped in MeOAc. For preparing $Pb(OAc)_2$ treated films, $Pb(OAc)_2$ (10-20 mg) was added to 20 mL of anhydrous MeOAc and sonicated for 10 min. Then, the third NC film was swiftly dipped into the ligand solution followed by rinsing using neat, anhydrous MeOAc, and drying with a stream of air. The process of spin coating and ligand treatment was repeated multiple (3-5) times.

On treating the NC film with MeOAc and $Pb(OAc)_2$ we did not notice any change in UV visible absorption peak position (Figure 5.3a), indicating retention of electronic properties. However, a shift of 5 nm towards longer wavelength is observed in the PL peak position (Figure 5.3b), on treating the film with MeOAc. Presently, we don’t know the reason for this shift.

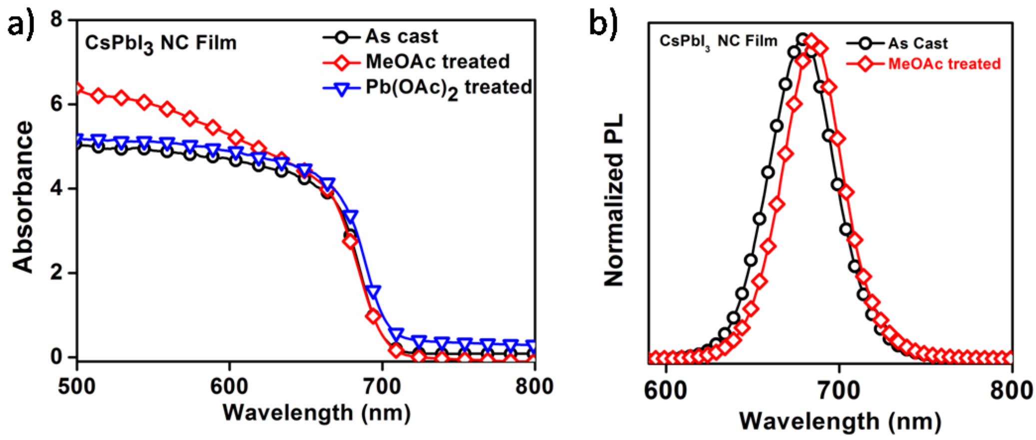

Figure 5.3 a) UV-vis and b) PL spectra of as cast and MeOAc treated films.

5.2.8 Sample Thickness: Scanning electron microscopy (SEM) imaging was performed by using Zeiss Ultra Plus SEM instrument for measuring film thickness. The thickness of the $CsPbI_3$ NC as cast, MeOAc and $Pb(OAc)_2$ treated films are ~ 5 μm, ~ 5.1 μm and ~ 2.5 μm, respectively (Figure 5.4) as measured from scanning electron microscope (SEM) images of the cross section of the films.

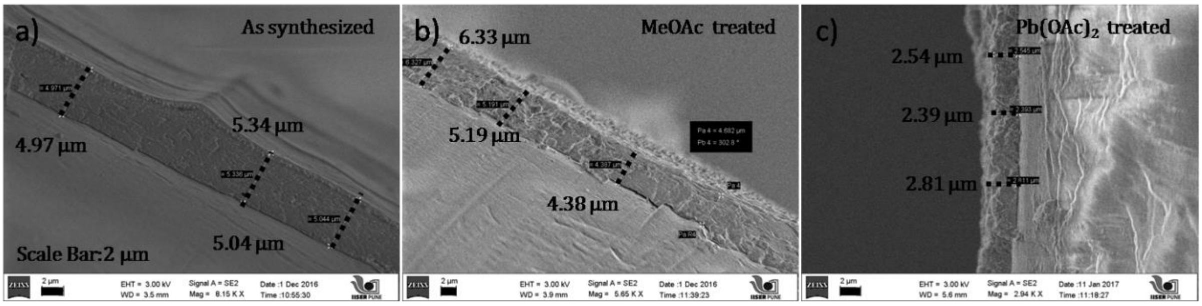

Figure 5.4 SEM images of $CsPbI_3$ NC films a) as cast, b) MeOAc treated and c) $Pb(OAc)_2$ treated.

5.3 Results and Discussion

5.3.1 Time domain THz spectroscopy of non-photoexcited films

The setup for performing THz-TDS study is elaborately described in Chapter 2. In the broad range of 0.5-7 THz, we collected time domain THz waveforms transmitted through $CsPbI_3$ NC, MeOAc and $Pb(OAc)_2$ treated films on HDPE from which absorbance, refractive index, real and imaginary dielectric function of the films are calculated (Figure 2). For all the three samples there is a shoulder close to 1 THz (~ 30 cm^{-1}) and a prominent absorption peak at ~ 2.5 THz (~ 83 cm^{-1}). The IR active lattice vibrations (optical phonons) in cubic $CsPbI_3$ give rise to the absorption features in the THz region. From previous THz-TDS of $CsPbBr_3$, we know that it has a strong absorption band with a peak at ~3.4 THz.[37] Pb-Br bond stretching and Br-Pb-Br bond angle bending in $PbBr_6$ octahedron are responsible for the observed THz absorbance in $CsPbBr_3$. Probably similar Pb-I stretching and I-Pb-I bond angle bending modes are also present in $CsPbI_3$. The THz absorption peak for $CsPbI_3$ is at a lower frequency compared to $CsPbBr_3$ which is expected due to weaker Pb-I bond strength compared to Pb-Br bond strength. From real dielectric function plot, we see that at the higher frequency limit the ε' value becomes around 5.5 for $CsPbI_3$ NCs. This value is comparable to that reported by Kovalenko and co-workers for cubic $CsPbI_3$. On the contrary, at the lower frequency limit, the real dielectric function of $Pb(OAc)_2$ treated film is unusually high, and we are trying to understand the reason for this.

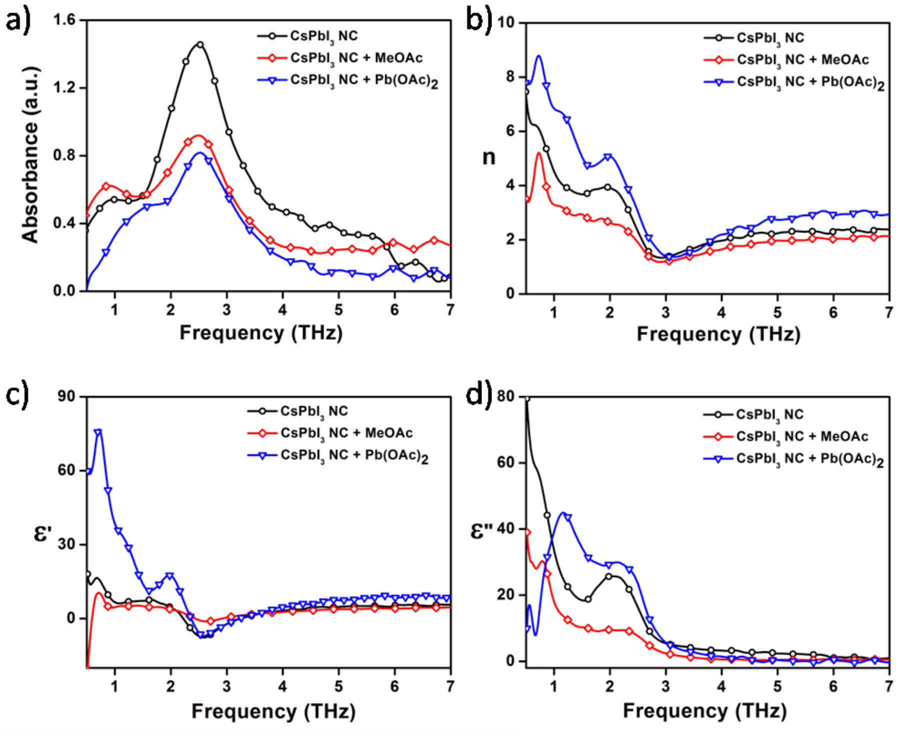

Figure 5.5 THz-TDS results showing a) absorbance, b) refractive index, c) real and d) imaginary dielectric function of as cast, MeOAc and $Pb(OAc)_2$ treated films.

5.3.2 Time-Resolved THz Spectroscopy: Photoconductivity and Carrier Dynamics:

5.3.2.1 Photoconductivity

TRTS, also known as optical pump THz probe (OPTP), has been utilized to study the carrier dynamics of as-cast, MeOAc and $Pb(OAc)_2$ treated $CsPbI_3$ NC films on non-conducting HDPE substrate. Pump wavelengths of 650 nm, 620 nm, and 550 nm are used to excite the samples. The first excitonic peak of $CsPbI_3$ NCs is ~660 nm. Therefore, exciting with 650 nm pump light creates carriers with a small excess energy (~29 meV) while exciting with 620 nm and 550 nm pump wavelengths create carriers with ~120 meV and ~375 meV excess energies, respectively. Carriers formed due to photoexcitation absorb THz radiation and a reduction in THz transmission ($-\Delta E(t_p)/E_0(t_p)$), proportional to the photoconductivity of the carriers, is collected by varying the pump-probe delay. In TRTS experiments of thin films, photoconductivity across the photoexcited film is measured. Hence, the measured conductivity will have a contribution from both intra and inter nanoparticle conductivity. This is because the NCs are capped by insulating ligands but again inter NC coupling will also be present in NC films. Thus, the THz response will come from both, free carriers within the NCs and carriers that can move between NCs connected to each other. Here we make a legitimate assumption that the observed THz response is due to the free carriers and not the excitons. This assumption is justified because we observe positive real conductivities for all three films in the complex conductivity spectra (Figure 5.6b, 5.7b and 5.8 b). The exciton binding energy for cubic $CsPbI_3$ is ~ 15 meV which is even less than thermal energy (k_BT) at room temperature (~26 meV) and therefore free carriers will dominate after photoexcitation.[38] The pump induced change in THz transmissions was recorded by measuring the evolution of peak THz amplitude (shown by the arrow in Figure 5.6a, 5.7a, 5.8a) as the pump-probe delay was varied up to 1.5 ns (Figure 5.6c, 5.7c, 5.8c). The photoconductivity $\Delta\sigma(t_p)$, which is proportional to the photo-induced change in THz transmission ($\frac{-\Delta E(t_p)}{E_0(t_p)}$), of the films is given by:

$$\Delta\sigma(t_p) = \frac{\varepsilon_0 c}{d}(n_a + n_b)\frac{-\Delta E(t_p)}{E_0(t_p)} \qquad (1)$$

where ε_0 is the permittivity of free space, c is the speed of light, d is the thickness of the photoexcited sample, and n_a and n_b are the refractive indices of the media on either side of the photoexcited sample. Here, $n_a = 1$ for air and $n_b = 1.54$ for HDPE substrate.

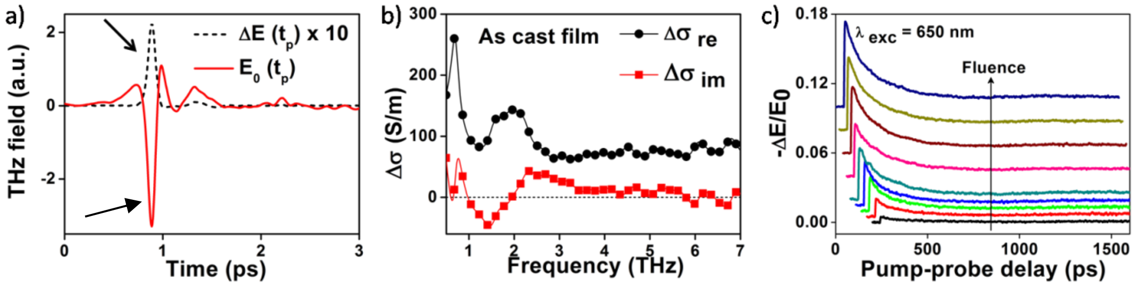

Figure 5.6. At zero pump-probe delay, ~ 300 μJ/cm^2 fluence and λ $_{exc}$ = 650 nm, a) Pump off (red) and pump-induced change in THz transmission, b) real (black) and imaginary (red) conductivity spectra of as-cast film. c) Fluence dependent (~20 -600 μJ/ cm^2) pump induced THz transients for the as-cast film.

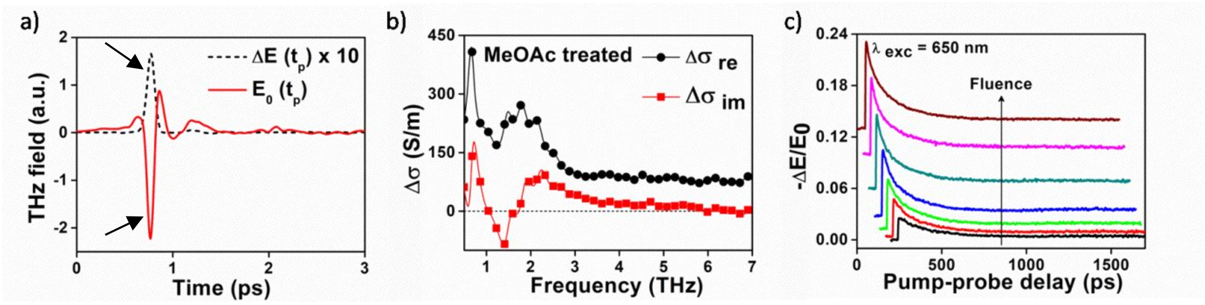

Figure 5.7. At zero pump-probe delay, ~ 300 μJ/cm^2 fluence and λ $_{exc}$ = 650 nm, a) Pump off (red) and pump-induced change in THz transmission, b) real (black) and imaginary (red) conductivity spectra of MeOAc treated film. c) Fluence dependent (~20 -400 μJ/ cm^2) pump induced THz transients for as MeOAc treated film.

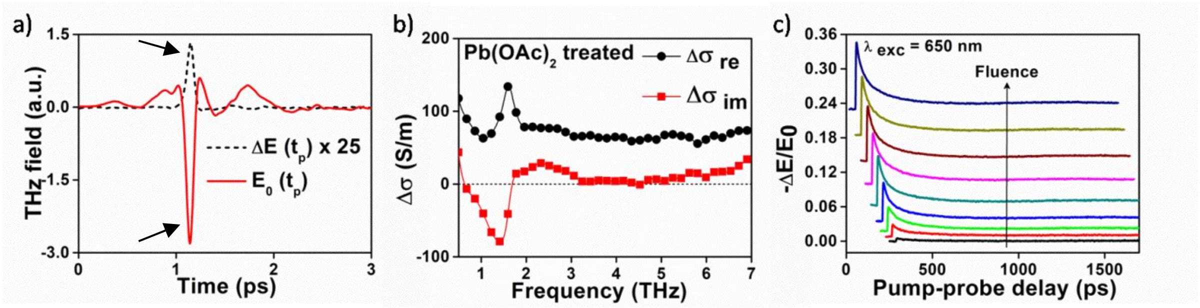

Figure 5.8. At zero pump-probe delay, ~ 300 μJ/cm^2 fluence and λ $_{exc}$ = 650 nm, a) Pump off (red) and pump-induced change in THz transmission, b) real (black) and imaginary (red) conductivity spectra of Pb(OAc)$_2$ treated film. c) Fluence dependent (~5 -200 μJ/ cm^2) pump induced THz transients for as Pb(OAc)$_2$ treated film.

The fluence dependent peak photoconductivity values calculated using above equation range from ~7 S/m to ~140 S/m for as-cast $CsPbI_3$ NC film (Figure 5.6). Using the equation, $\varphi\mu \cong \frac{\Delta\sigma}{qN_0}$, effective carrier mobility at the peak of THz transients are calculated, where q is the elementary charge, N_0 is the total carrier density and φ is the photon to free carrier conversion ratio. Since the effective masses for holes and electrons are similar for cubic $CsPbI_3$ ($m_h^* = 0.13$ and $m_e^* = 0.11$) as reported by Kovalenko and co-workers, they should contribute nearly equally to photoconductivity and have comparable mobilities ($\mu_e \approx \mu_h$).[25] Supposedly each photon gives rise to two carriers, an electron and a hole, and we assume φ = 1. The carrier density varies from 0.3 – 8 X $10^{18}/cm^3$ for the as-cast $CsPbI_3$ NC film and the mobility spans from ~0.7 – 4 $cm^2\ V^{-1}\ s^{-1}$ (Figure 5.9).

The photoconductivity and mobility values show modest wavelength dependence with the values being slightly higher when excited using 550 nm excitation wavelength (Figure 5.9).

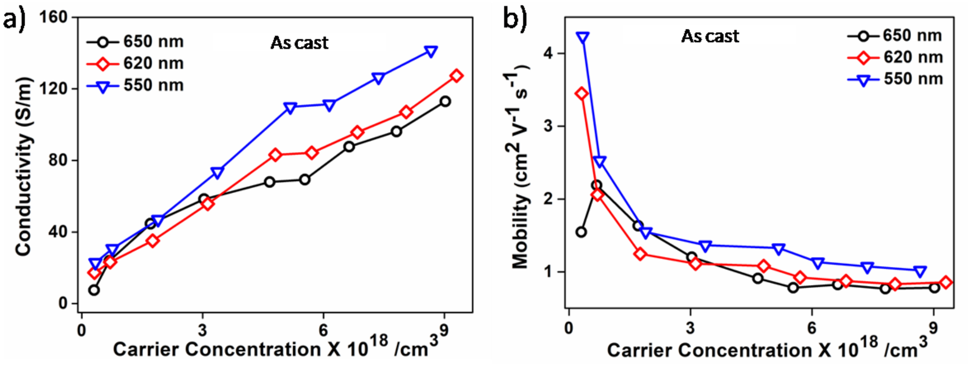

Figure 5.9. Wavelength and carrier concentration dependent a) peak photoconductivity and b) mobility of as cast $CsPbI_3$ NC film.

The $CsPbI_3$ NCs are capped with insulating oleylammonium surface ligands. Thus, lower connectivity between adjoining NCs and hence, a reduced mobility is expected. Yet the mobility values obtained for $CsPbI_3$ NC film are comparable to the mobility values reported for solution processed $CH_3NH_3PbI_3$ thin film measured using different techniques (1-10 $cm^2\ V^{-1}\ s^{-1}$).[4]

Subsequently, we measured the peak photoconductivity and effective mobility of NC films treated with MeOAc and $Pb(OAc)_2$. On treating the NC film with MeOAc and $Pb(OAc)_2$, we did not notice any change in UV visible absorption peak position indicating retention of electronic properties. Also, from the FTIR spectra reported by Swarnkar *et al.*,[30] it is known that washing the NC film with MeOAc displaces the oleylammonium, oleate or octadecene as confirmed by the absence of C-H modes close to 3000 cm^{-1} or below 2000 cm^{-1}.

At similar fluence, the peak photoconductivity values for NC film treated with MeOAc and $Pb(OAc)_2$ are higher compared to the values calculated for as-cast $CsPbI_3$ NC film. In the case of MeOAc treated film, the peak photoconductivity values range from ~ 25 S/m to ~ 600 S/m and show strong wavelength dependence (Figure 5.10). At comparable carrier density for λ_{exc} = 650 nm, the photoconductivity values are double compared to when excited with 550 nm wavelength. The mobility values at the peak of THz transients for MeOAc treated film span from ~1.5 - 20 $cm^2 V^{-1} s^{-1}$ depending on excitation wavelength and carrier concentration (Figure 5.10). Fluence dependent peak photoconductivity values calculated for $Pb(OAc)_2$ treated film vary from ~20 S/m to 400 S/m and mobility values span from ~1 – 6.5 $cm^2 V^{-1} s^{-1}$. $Pb(OAc)_2$ treated film also exhibits wavelength dependent conductivity and mobility (Figure 5.10). Hence treating the NC film with MeOAc and $Pb(OAc)_2$ is altering the transport properties of the NC films.

Enhanced photoconductivity is a direct measure of inter NC coupling in ligand treated films. Higher peak photoconductivity for ligand treated films is expected since treating with MeOAc or saturated solution of $Pb(OAc)_2$ in MeOAc displaces a fraction of the long chain insulating capping ligands around NCs and enhances dot-to-dot carrier conduction across the NC film.

Another crucial point to note, when comparing the photoconductivity of the neat NC film with that of the ligand treated film, is that at similar carrier concentration, greater photoconductivity is indicative of higher carrier mobility in ligand treated films since photoconductivity is the product of carrier concentration and mobility. Mobility values calculated at the onset of recombination processes reflect the improved connection between adjacent NCs by ligand removal.

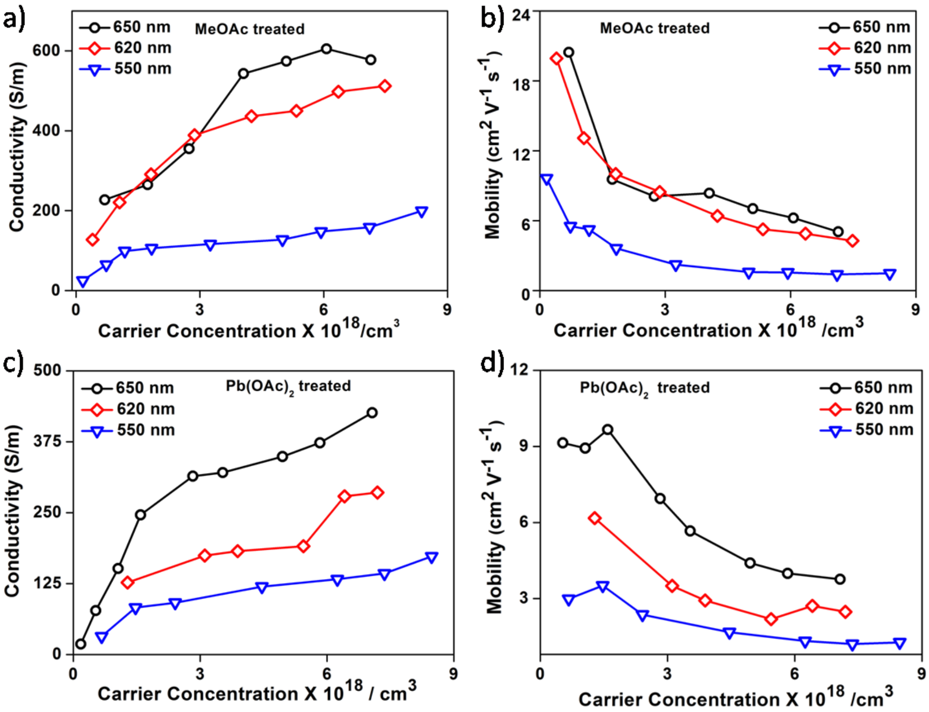

Figure 5.10. Wavelength and carrier concentration dependent a) peak photoconductivity and b) mobility of MeOAc treated film, c) peak photoconductivity and d) mobility of Pb(OAc)$_2$ treated film.

When carriers, formed by above bandgap excitation, have a high kinetic energy (K.E), greater conductivity and mobility is expected. However greater K.E of the carriers also leads to a higher rate of collisions that result in an enhanced carrier-carrier scattering and a reduced mobility.[6] This scenario is common for the as-cast, MeOAc and Pb(OAc)$_2$ treated films. Yet, we observe a prominent wavelength dependence of peak photoconductivity and hence mobility exhibited by ligand treated films. But, the photoconductivity and mobility values of the as-cast film is somewhat independent of wavelength variation.

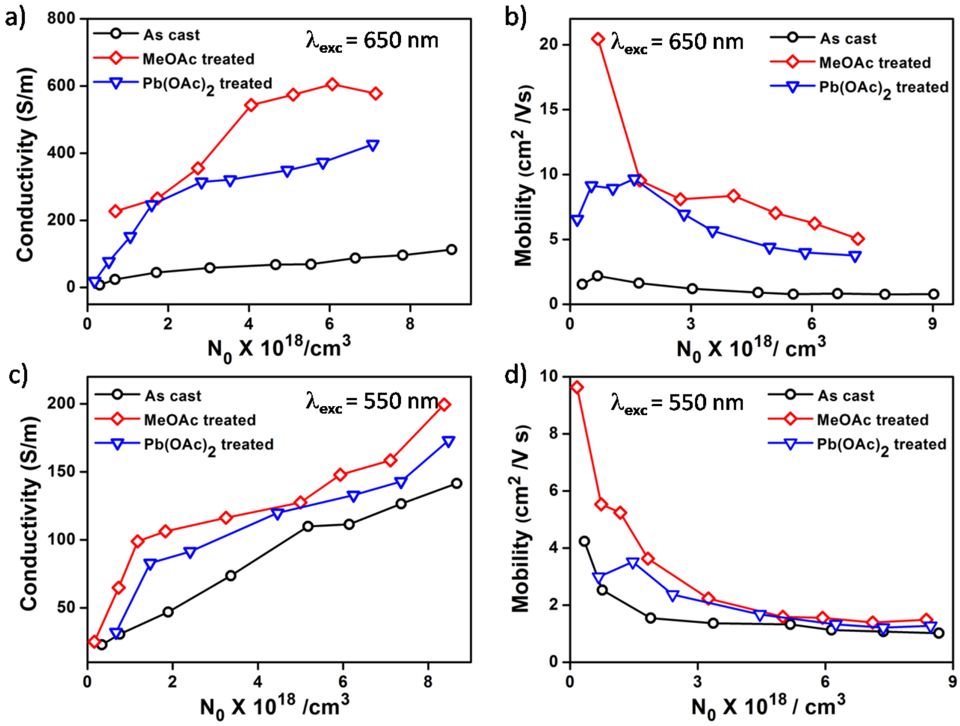

Figure 5.11. Comparing conductivity, a) and c), and mobility b) and d) of all three films when excited with 650 nm and 550 nm pump wavelength respectively.

There are theoretical studies suggesting the presence of halide vacancies above the conduction band edges in $CsPbX_3$.[39,40] The bromine vacancy (V_{Br}) in $CsPbBr_3$ has been reported to be 0.1 eV higher than the conduction band edge.[41] In case of $CsPbI_3$ since the Pb-Pb distance is longer than that in $CsPbBr_3$, insubstantial hybridization of Pb-6p orbitals at iodine vacancy (V_I) will be insufficient to lower the energy of the defect states below the conduction band to a localized state. Thus, we presume the V_I will be positioned even higher than 0.1 eV above the CB edge. The iodine vacancies will be present in as cast and the treated films.

From the above figure (Figure 5.11), we can see that the increase in photoconductivity and mobility of MeOAc and $Pb(OAc)_2$ treated films are much higher compared to those in as-cast film when excited using 650 nm, whereas photoconductivity and mobility values are similar for all the three films when excited using 550 nm of pump wavelength. Two competing processes that affect the transport properties of the ligand treated films are: a) increase in dot-to-dot connection and b) introduction of additional defect states by ligand removal. In as cast film of $CsPbI_3$ NCs, weak acid base interaction between I^- (soft base) and oleylammonium ligand (hard acid) is present. Washing with MeOAc readily displaces the oleylammonium ligands leaving free iodide. These might act as trap states for holes in the MeOAc treated films. Further washing with $Pb(OAc)_2$ is intended to passivate these dangling bonds. Supposedly the trap states formed due to free I^- are also within the valence band. We further hypothesize that trap densities near the band edge and at higher excitonic levels are different and follow a distribution. The darker colour in the band (Figure 5.12) represents greater density of trap states that can be easily accessed by 550 nm excitation while lighter colour is indicative of lesser density of trap states close to band edge excitation. In ligand treated film greater proximity of V_I in adjacent nanocrystals further destabilizes the vacancy sites pushing them to higher energy in the bands. So, when 550 nm that imparts 375 meV of excess energy than required for band edge excitation, is used as pump wavelength the electrons get trapped at V_I and holes get trapped by excess I^-. Thus, a reduced photoconductivity and mobility is shown by the MeOAc treated film at 550 nm compared to 620 nm and 650 nm excitations, that create carriers with 120 meV and 29 meV of excess energy respectively (Figure 5.11).

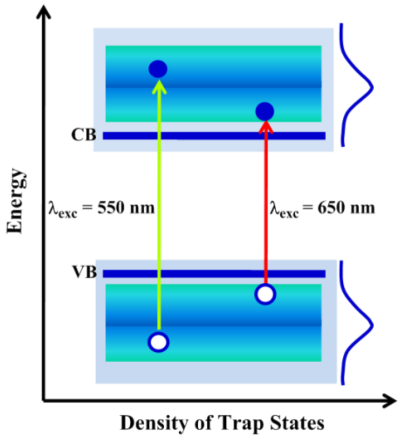

Figure 5.12. Schematic showing trap states that can be accessed by carriers with higher kinetic energy. The darkly shaded region corresponds to higher density of trap states while the lighter shaded region corresponds to lower density of trap states.

Passivation of I^- by treating with $Pb(OAc)_2$ should further increase photoconductivity and mobility of the carriers. But carriers in MeOAc treated film exhibit maximum photoconductivity and mobility. While we think the presence of three water molecules in lead salt (PbOAc)$_2$.3H$_2$O) may interfere with the desired outcome, this assumption is not conclusive.

Another observation further supports our conjecture discussed above. For the as-cast film of CsPbI$_3$ NCs, we observe a linear dependence of peak THz signal ($-\Delta E/E_0$) with the pump fluence (Figure 5.13 a). Interestingly, the peak THz transient for MeOAc and Pb(OAc)$_2$ treated films show an initial non-linear dependence on the pump fluence. The dependence becomes somewhat linear above ~1.8 x 10^{18}/cm^3 carrier density (Figure 5.13 b and c). This may be due to initial filling of the trap states created by MeOAc and Pb(OAc)$_2$ treatment of the films.

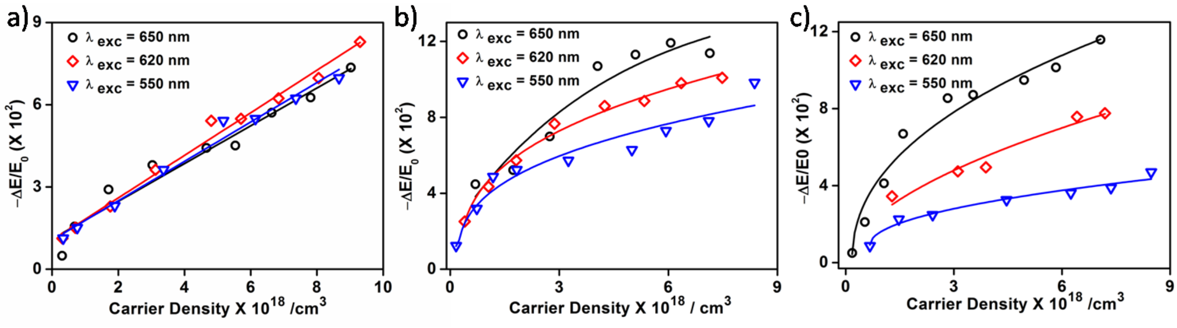

Figure 5.13. a) Peak THz transient of as-cast film at different excitation wavelengths with increasing carrier density. Solid lines are linear fits to the data points. b) and c) peak THz transients at different excitation wavelengths for MeOAc and Pb(OAc)$_2$ treated films respectively. Solid lines are non-linear fits to the data points.

5.3.2.2 Carrier Dynamics

Now, we would like to find out the effect of ligand treatment on temporal evolution of the carriers after their genesis by above band gap excitation of the NCs. We assume here that the carrier mobilities are roughly constant over the temporal window of our experiment (1.5 ns) and the THz transients are dominated by the decrease in carrier density with time due to recombination. To resolve the different carrier recombination pathways, we have fitted the THz transients to a multiexponential function convoluted with a Gaussian function of the form:

$$y = G(t - t_0)\otimes \sum_i a_i \exp\left[-\frac{t - t_0}{\tau_i}\right] \qquad (2)$$

where $G(t - t_0)$ is a Gaussian function centered at t_0 with FWHM of ~300 fs (the instrument response time of our TRTS experiment), and a_i is the contribution of the i^{th}

exponential decay channel with time constant τ_i towards the entire decay process, we fit the normalized THz transients to resolve the carrier recombination pathways.

First, we consider the recombination mechanisms occurring in the as-cast film of $CsPbI_3$ NCs. A biexponential decay function adequately fits the normalized decay kinetics at 620 nm and 650 nm excitation wavelengths and all fluences. When 550 nm pump is used, only at higher fluences, a triexponential function is required to fit the THz transients. The parameters obtained from the multiexponential fits to the photoconductivity decay profiles are listed in Table 5.1-5.3. For all fluences and wavelength, the relaxation dynamics of the as-cast film beyond 600 ps becomes almost flat and independent of pump fluence (Figure 5.14). We assign this slowest decay to the monomolecular carrier trapping mechanism. Since THz responds merely to free carriers, geminate electron-hole recombination though monomolecular will not show up in our data. The average lifetime from PL decay of as-cast film was reported to be 3.8 ns by Swarnkar *et al.*[30] Keeping the slowest process as 3.8 ns for fitting the THz transients did not yield a good fit. We kept the time for the slowest process to be 15 ns, ten times of our temporal window, and this yielded a reasonably good fit. Though the time scale for trap assisted recombination has some uncertainty as the temporal window of our experiments are not long enough, it is certainly more than the radiative recombination time. Beyond the temporal window of our experiment i.e. 1.5 ns, moderate photoconductivity still persists. The contribution from trap assisted recombination is only ~ 10 % of the total recombination mechanism which further establishes the defect tolerant nature of these NCs.

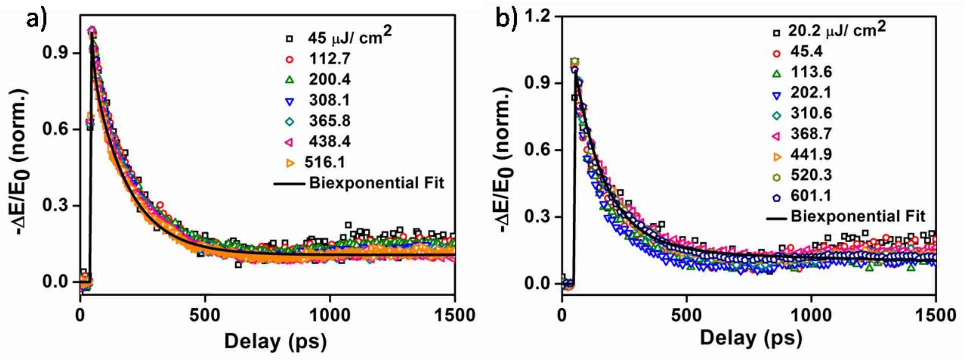

Figure 5.14. Normalized transient photoconductivity of as-cast film at different fluences for (a) 550 nm, and (b) 650 nm excitation.

The average lifetimes (<τ>) are calculated as $< \tau > = \sum f_i \tau_i$, where, f_i ($f_i = a_i \tau_i / \sum a_j \tau_j$) gives the contribution of the ith process towards recombination dynamics. The average lifetime of the carriers slightly declines with increasing fluence. The second exponential has a mean time constant (τ_2) of ~140 ps at λ_{exc} = 550 nm, ~180 ps at λ_{exc} = 620 nm, and ~125 ps at λ_{exc} = 650 nm (Table 5.1-5.3). We attribute this time scale to the bimolecular electron-hole recombination process. The contribution from the fastest process appears only for 550 nm pumping at fluences greater than 300 μJ/cm^2 and do not show much of a trend. Auger recombination is absent even at higher fluences when excited using 650 nm and 620 nm pump wavelengths which impart ~ 29 meV and ~ 120 meV of above band gap excess energy to the carriers. Also, the linear dependence of peak photoconductivity to carrier density (Figure 5.13 a) hint at absence of non-linear processes occurring in the NC film. Auger recombination may be absent because the carriers may not have sufficient energy for three body collision to take place. Again since these are defect tolerant, defect assisted Auger recombination is also improbable.[33] Only, when pumped using 550 nm wavelength which confers 375 meV of excess energy to the carriers and at fluences > 300 μJ/cm^2, a triexponential function is required to fit the THz transients. The fastest process has a mean time constant (τ_1) of ~ 20 ps. In a previous study on $CsPbI_3$ NCs, Liu *et al.* ascribed a 23 ps time scale to Auger recombination. We also assign this time scale to Auger recombination. Maybe at very high carrier density when carriers have 375 meV of excess kinetic energy, three body collisions between charge carriers become possible.

On treating the films with MeOAc and $Pb(OAc)_2$, the photoconductivity decay is mostly dominated by tri-exponential function. Only at low fluences, a bi-exponential function can fit the decay reasonably well (Figure 5.15 and 5.16). The average time scale of the faster process is 20-40 ps (τ_3, Table 5.4 and 5.5). The contribution from intermediate decay shows wavelength dependence. At 650 nm excitation wavelength, the intermediate process (τ_2) for all the three films occur at a similar time scale and the overall trend is that it becomes slower with increasing carrier density. At 620 nm and 550 nm excitation wavelength, the contribution from intermediate process decreases (faster decay) for samples treated with MeOAc and $Pb(OAc)_2$ compared to the as-cast film. From normalized spectra at all fluences and at each wavelength for the three samples, we observe that the decays look quite similar for all of them after 600 ps. So, we kept the time scale of the slowest process as 1.5 ns, which is ten times of the temporal window of our experiments. We presume that on ligand treatment the removal of oleylamine ligands leads to the formation of new defect states in the NCs. The fastest decay component (τ_3) observed for the ligand treated films corresponds to filling of these new trap states. From the tables listed below, we see that with increasing fluence the τ_3 component becomes slower. This further substantiates our hypothesis discussed earlier that with increasing fluence the trap states are getting filled and once the trap states are filled the decay becomes slower.

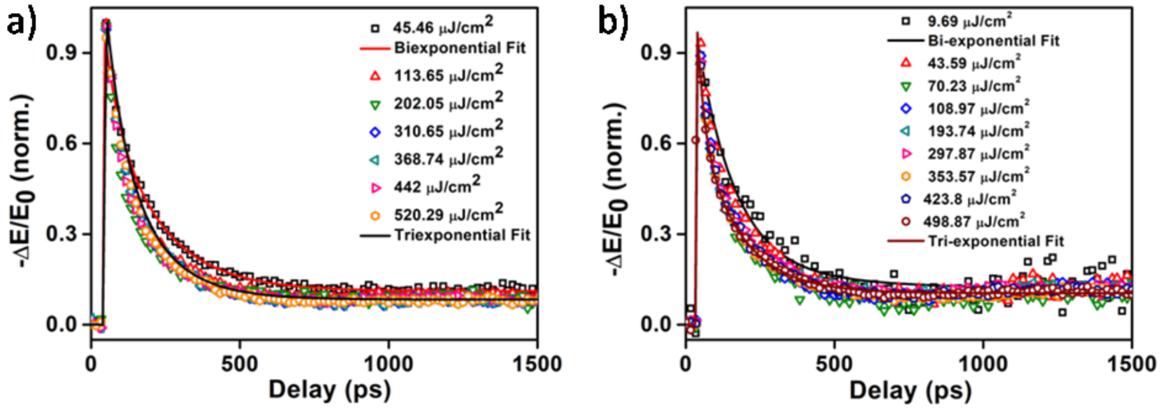

Figure 5.15. Normalized transient photoconductivity of film treated with MeOAc at different fluences for (a) 650 nm, and (b) 550 nm excitation.

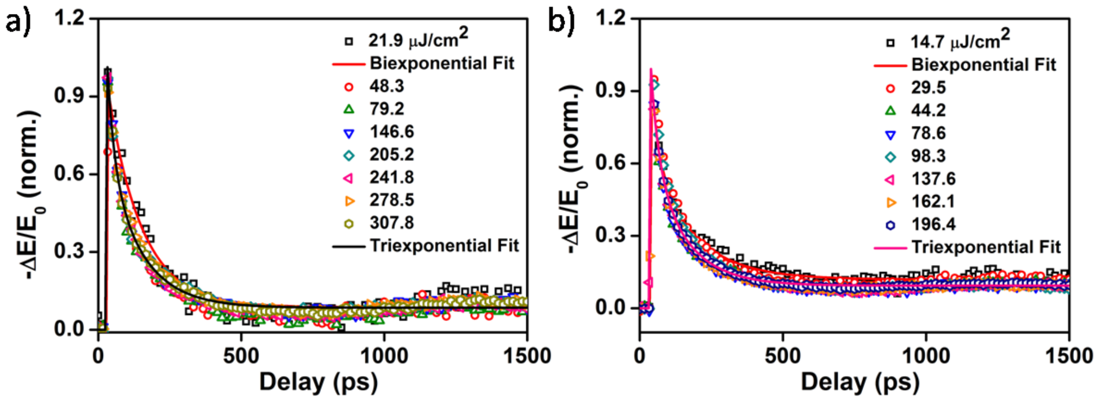

Figure 5.16. Normalized transient photoconductivity of film treated with $Pb(OAc)_2$ at different fluences for (a) 650 nm, and (b) 550 nm excitation.

In figure 5.17, we have plotted the normalized THz transients of the as-cast, MeOAc, and $Pb(OAc)_2$ treated films excited at 620 nm excitation wavelength and at a fluence of ~ 160 μJ/cm². The ligand treated films show a faster decay compared to the as-cast film. The initial decay for the treated films is dominated by the fast filling of the trap states. Although the bimolecular recombination time scales (τ_2, Table 5.1-5.9) are similar for all three films, the overall conductivity decay is much faster for the treated films till 600 ps.

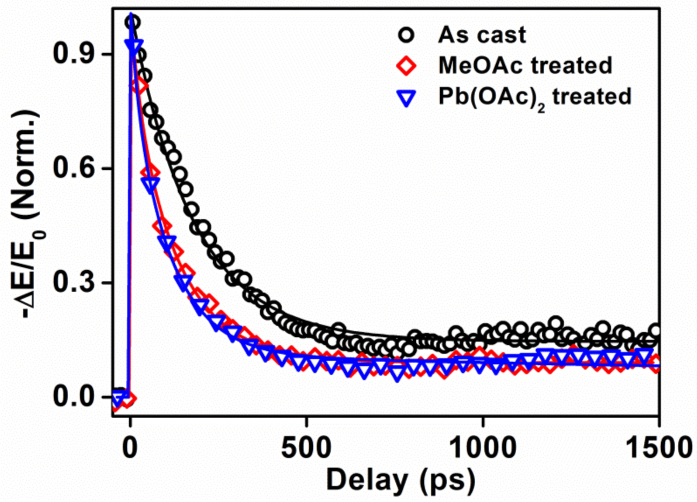

Figure 5.17. Normalized THz transients of as cast, MeOAc, and $Pb(OAc)_2$ treated films at λ_{exc} = 620 nm and 160 μJ/ cm² fluence.

Table 5.1: Parameters obtained by fitting the THz transients of the as-cast $CsPbI_3$ NC film to equation 2 when excited using 650 nm pump wavelength.

N_0 ($10^{18}/cm^3$)	Fluence (μJ/cm²)	a_1	τ_1(ps)	a_2	τ_2 (ps)	τ_{avg} (ps)
0.3	20.2	0.163 (0.00)	15000	0.73 (0.001)	120.71 (0.273)	14474
0.68	45.46	0.134 (0.00)	15000	0.82 (0.001)	109.03 (0.13)	14365
1.71	113.65	0.108 (0.00)	15000	0.84 (0.00)	108.61 (0.083)	14206
3.03	202.05	0.1 (0.00)	15000	0.836 (0.00)	104 (0.07)	14183
4.66	310.65	0.13 (0.00)	15000	0.864 (0.00)	131.15 (0.08)	14183
5.53	368.74	0.15 (0.00)	15000	0.857 (0.00)	132 (0.07)	14288
6.64	441.99	0.127 (0.00)	15000	0.876 (0.00)	132.71 (0.065)	14144

7.81	520.28	0.126 (0.00)	15000	0.856 (0.00)	135.73 (0.06)	14139
9.02	601.1	0.126 (0.00)	15000	0.856 (0.00)	134.4 (0.07)	14147

Table 5.2: Parameters obtained by fitting the THz transients of the as-cast CsPbI$_3$ NC film to equation 2 when excited using 620 nm pump wavelength.

N_0 (10^{18}/cm^3)	Fluence (μJ/cm^2)	a_1	τ_1(ps)	a_2	τ_2(ps)	τ_{avg} (ps)
0.31	21.83	0.22 (0.00)	15000	0.85 (0.00)	176.92 (0.187)	14292
0.7	49.13	0.23 (0.00)	15000	0.83 (0.00)	181.9 (0.2)	14299
1.75	122.82	0.2 (0.00)	15000	0.84 (0.004)	176.75 (0.155)	14300
3.13	218.34	0.15 (0.00)	15000	0.86 (0.003)	172.38 (0.12)	14083
4.81	335.71	0.15 (0.00)	15000	0.86 (0.00)	180.61 (0.125)	14043
5.71	398.48	0.14 (0.00)	15000	0.85 (0.00)	182.02 (0.09)	14046
6.84	477.63	0.147 (0.00)	15000	0.86 (0.00)	175.13 (0.08)	14062
8.05	562.24	0.14 (0.00)	15000	0.83 (0.00)	180.95 (0.07)	14010
9.3	649.57	0.125 (0.00)	15000	0.826 (0.00)	177.63 (0.08)	13924

Table 5.3: Parameters obtained by fitting the THz transients of the as-cast CsPbI$_3$ NC film to equation 2 when excited using 550 nm pump wavelength.

N_0 (10^{18}/cm^3)	Fluence (μJ/cm^2)	a_1	τ_1(ps)	a_2	τ_2(ps)	a_3	τ_3(ps)	τ_{avg} (ps)
0.34	20.04	0.14 (0.00)	15000	0.84 (0.00)	123.61 (0.13)			14259
0.76	45.09	0.144 (0.00)	15000	0.84 (0.00)	129.72 (0.13)			14259
1.89	112.74	0.135 (0.00)	15000	0.88 (0.00)	139.44 (3.2)			14150
3.37	200.43	0.14 (0.00)	15000	0.83 (0.00)	138.19 (2.5)			14230

5.17	308.15	0.12 (0.00)	15000	0.84 (0.00)	141.54 (0.07)			14079
6.14	365.78	0.1 (0.00)	15000	0.8 (0.001)	147.68 (0.21)	0.11 (0.002)	14.7 (0.44)	14006
7.36	438.43	0.11 (0.00)	15000	0.81 (0.001)	146.68 (0.11)	0.1 (0.00)	14.52 (0.26)	13979
8.67	516.09	0.11 (0.00)	15000	0.78 (0.001)	139.43 (0.125)	0.09 (0.001)	18 (0.35)	14068

Table 5.4: Parameters obtained by fitting the THz transients of MeOAc treated NC film to equation 2 when excited using 650 nm pump wavelength.

N_0 (10^{18}/cm^3)	Fluence (μJ/cm^2)	a_1	τ_1 (ps)	a_2	τ_2 (ps)	a_3	τ_3 (ps)	τ_{avg} (ps)
0.69	45.46	0.13 (0.00)	15000	0.85 (0.00)	120 (0.077)			14260
1.73	113.65	0.11 (0.00)	15000	0.86 (0.00)	108.36 (0.081)			14203
2.73	202.05	0.095 (0.00)	15000	0.6 (0.00)	122.14 (0.07)	0.3 (0.001)	24.97 (0.074)	14202
4.05	310.65	0.084 (0.00)	15000	0.73 (0.002)	126.37 (0.22)	0.17 (0.002)	33.52 (0.47)	13924
5.09	368.74	0.084 (0.00)	15000	0.64 (0.002)	124.9 (0.26)	0.29 (0.002)	37.49 (0.29)	14003
6.06	442	0.09 (0.00)	15000	0.6 (0.00)	129.44 (0.075)	0.31 (0.00)	39.04 (0.09)	14072

Table 5.5: Parameters obtained by fitting the THz transients of MeOAc treated NC film to equation 2 when excited using 620 nm pump wavelength.

N_0 (10^{18}/cm^3)	Fluence (μJ/cm^2)	a_1	τ_1(ps)	a_2	τ_2 (ps)	a_3	τ_3 (ps)	τ_{avg} (ps)
0.4	23.23	0.18 (0.00)	15000	0.87 (0.00)	160.7 (0.112)			14253
1.05	61.24	0.13 (0.00)	15000	0.84 (0.00)	140.44 (0.073)			14170
1.81	105.58	0.12 (0.00)	15000	0.85 (0.00)	130.51 (0.067)			14115
2.87	166.83	0.09 (0.00)	15000	0.731 (0.00)	133.78 (1.87)	0.2 (0.007)	33.23 (0.93)	14006
4.25	247.07	0.11 (0.00)	15000	0.565 (0.001)	149.63 (0.26)	0.3 (0.001)	37.46 (0.21)	14269

5.34	310.43	0.11 (0.00)	15000	0.647 (0.002)	164.7 (0.27)	0.22 (0.001)	46.00 (0.37)	14100
6.35	369.56	0.11 (0.00)	15000	0.568 (0.002)	166 (0.3)	0.31 (0.001)	47.11 (0.25)	14198
7.48	435.03	0.11 (0.00)	15000	0.585 (0.002)	161.63 (0.32)	0.29 (0.002)	47.21 (0.29)	14188

Table 5.6: Parameters obtained by fitting the THz transients of MeOAc treated NC film to equation 2 when excited using 550 nm pump wavelength.

N_0 (10^{18}/cm^3)	Fluence (μJ/cm^2)	a_1	τ_1 (ps)	a_2	τ_2 (ps)	a_3	τ_3 (ps)	τ_{avg} (ps)
0.73	43.59	0.1 (0.00)	15000	0.67 (0.003)	112.6 (0.35)	0.19 (0.003)	30 (0.56)	14228
1.18	70.23	0.12 (0.00)	15000	0.69 (0.003)	115.13 (0.28)	0.18 (0.002)	32.5 (0.52)	14321
1.83	108.98	0.12 (0.00)	15000	0.62 (0.002)	121.33 (0.22)	0.25 (0.001)	29.5 (0.25)	14341
3.25	193.74	0.12 (0.00)	15000	0.57 (0.002)	134.74 (0.24)	0.3 (0.001)	34.47 (0.22)	14307
4.99	297.87	0.11 (0.00)	15000	0.56 (0.001)	133.52 (0.25)	0.33 (0.001)	30.9 (0.18)	14239
5.93	353.57	0.11 (0.00)	15000	0.61 (0.002)	126.68 (0.28)	0.28 (0.002)	30 (0.23)	14278
7.11	423.8	0.12 (0.00)	15000	0.56 (0.001)	137.87 (0.24)	0.33 (0.001)	31.69 (0.18)	14274
8.37	498.87	0.11 (0.00)	15000	0.56 (0.001)	136.41 (0.25)	0.325 (0.001)	31.35 (0.18)	14258

Table 5.7: Parameters obtained by fitting the THz transients of Pb(OAc)$_2$ treated NC film to equation 2 when excited using 650 nm pump wavelength.

N_0 (10^{18}/cm^3)	Fluence (μJ/cm^2)	a_1	τ_1 (ps)	a_2	τ_2 (ps)	a_3	τ_3 (ps)	τ_{avg} (ps)
0.5	14.74	0.13 (0.00)	15000	0.53 (0.002)	140.36 (0.34)	0.33 (0.002)	29.1 (0.224)	14375
1.59	44.22	0.1 (0.00)	15000	0.49 (0.00)	119.66 (1.7)	0.43 (0.005)	29.12 (0.83)	14303
2.83	78.62	0.09 (0.00)	15000	0.52 (0.002)	114.28 (0.26)	0.41 (0.002)	27.93 (0.15)	14276
3.53	98.27	0.09 (0.00)	15000	0.63 (0.002)	113.33 (0.23)	0.273 (0.002)	32.26 (0.26)	14187
4.95	137.58	0.09 (0.00)	15000	0.54 (0.002)	116.83 91.63)	0.39 (0.005)	31.3 (0.84)	14217

5.83	162.15	0.09 (0.00)	15000	0.54 (0.00)	113.3 (1.5)	0.369 (0.005)	32.1 (0.37)	14270
7.07	196.54	0.1 (0.00)	15000	0.53 (0.002)	109.56 (0.33)	0.367 (0.002)	33.8 (0.24)	14302

Table 5.8: Parameters obtained by fitting the THz transients of $Pb(OAc)_2$ treated NC film to equation 2 when excited using 620 nm pump wavelength.

N_0 (10^{18}/cm^3)	Fluence (μJ/cm^2)	a_1	τ_1 (ps)	a_2	τ_2 (ps)	a_3	τ_3 (ps)	τ_{avg}
1.28	67.23	0.11 (0.00)	15000	0.88 (0.00)	99.53 (2.6)			14244
3.11	162.97	0.09 (0.00)	15000	0.86 (0.00)	110.87 (1.9)			14007
3.89	203.72	0.1 (0.00)	15000	0.763 (0.001)	113.87 (0.14)	0.13 (0.001)	20.1 (0.32)	14137
5.44	285.21	0.1 (0.00)	15000	0.82 (0.01)	89.63 (0.59)	0.1 (0.008)	29.6 (0.9)	14283
6.41	336.13	0.076 (0.00)	15000	0.64 (0.003)	105.69 (0.27)	0.27 (0.002)	28 (0.3)	14077
7.19	376.88	0.067 (0.00)	15000	0.57 (0.002)	110.11 (0.33)	0.35 (0.002)	30 (0.3)	13987

Table 5.9: Parameters obtained by fitting the THz transients of $Pb(OAc)_2$ treated NC film to equation 2 when excited using 550 nm pump wavelength.

N_0 (10^{18}/cm^3)	Fluence (μJ/cm^2)	a_1	τ_1 (ps)	a_2	τ_2 (ps)	a_3	τ_3 (ps)	τ_{avg} (ps)
0.67	21.98	0.09 (0.00)	15000	0.87 (0.1)	116.16 (4.02)			13984
1.478	48.37	0.074 (0.004)	15000	0.642 (0.00)	104.01 (4.0)	0.243 (0.02)	19.361 (2)	14154
2.41	79.14	0.08 (0.00)	15000	0.64 (0.002)	106 (0.245)	0.29 (0.002)	22 (0.225)	14154
4.46	146.56	0.09 (0.00)	15000	0.69 (0.004)	101.13 (0.42)	0.21 (0.004)	28.21 (0.5)	14304
6.24	205.19	0.09 (0.00)	15000	0.56 (0.003)	116.7 (0.45)	0.35 (0.002)	29 (0.245)	14327
7.36	241.83	0.08 (0.00)	15000	0.67 (0.003)	105.6 (0.27)	0.22 (0.002)	29 (0.41)	14199
8.47	278.47	0.09 (0.00)	15000	0.62 (0.002)	113.1 (0.27)	0.26 (0.002)	29.53 (0.31)	14294
9.36	307.79	0.09 (0.00)	15000	0.57 (0.002)	115.98 (0.27)	0.33 (0.002)	27 (0.21)	14301

5.3.2.3. Diffusion Length

The diffusion length (L_D) of carriers is a very crucial parameter that determines whether a semiconductor material can be used in PVs and other electro-optic devices. Carrier diffusion length can be calculated from an average lifetime according to the equation:

$$L_D = \sqrt{(\langle\tau\rangle \mu k_B T/q)} \qquad (3)$$

where $\langle\tau\rangle$ is the average life time, μ is the mobility, k_B is Boltzmann constant, T is temperature and q is the elementary charge. The average lifetime $\langle\tau\rangle$ is calculated as $\langle\tau\rangle = \sum f_i\tau_i$, where f_i is the steady state population fraction of the i^{th} decay channel.[42], [43] Considering τ_3 to be 15 ns (used for fitting all our THz transients), we calculate an average L_D of 0.2 μm for the as-cast film, 0.4 μm for $Pb(OAc)_2$ treated film, and 0.5 μm for MeOAc treated film. At the carrier concentration at which our experiments were performed, the diffusion lengths are comparable to that reported for vapour deposited $CH_3NH_3PbI_{3\_x}Cl_x$ polycrystalline film.[44]

There are reports where initially poorly conducting PbSe quantum dots capped with oleic acid could be used in field effect transistors after treating the PbSe quantum dot using hydrazine[45] and EDT[46] which enhanced their conductivity by reducing interparticle spacing, enhanced electronic coupling and trap states passivation. In a more recent study, Baxter and co-workers have reported the effect of five ligand exchange reagents NH_4SCN, Na_2S, EDA, EDT, and TBAI on conductivity and lifetime of PbSe NC film initially capped with insulting oleic acid.[43] The performance of the NC thin-film device depends on the choice of the ligands used. With NH_4SCN (ammonium thiocyanate) and Na_2S (sodium sulphide) ligand replacements, the film showed enhanced mobility but faster decay while replacement with EDA (ethylenediamine), EDT (1,2-ethanedithiol), and TBAI (tetrabutylammonium iodide) showed lower mobility but slower photoconductivity decay and thus longer diffusion length. In this study where $CsPbI_3$ NC films capped with oleylamine are treated with MeOAc and $Pb(OAc)_2$, the insulating ligands are displaced and not replaced by the MeOAc or $Pb(OAc)_2$ as confirmed from IR data.[30] Though we observe a faster initial decay of the THz transients for the treated films (Figure 5.17), the diffusion length values for the treated films are higher than the as-cast film. Thus, we can comment that on treating $CsPbI_3$ NC films with MeOAc and $Pb(OAc)_2$, the increase in mobility due to better inter NC coupling dominates which is an encouraging news for using $CsPbI_3$ NCs for device fabrication.

5.4 Conclusion

We have utilized time-resolved THz spectroscopy to study the semiconductor properties and carrier dynamics of cubic $CsPbI_3$ NC thin film under ambient condition for the first time. We further studied the effect of ligand treatment on the semiconductor properties and recombination dynamics. Treating the as-cast film lead to displacement of the insulating oleylamine ligands that enhances inter NC coupling. We indeed observe an increase in peak photoconductivity and mobility of the ligand treated films compared to the as-cast film. But ligand treatment also leads to the formation of new defect states which is evident from the wavelength dependent peak photoconductivity and introduction of a new faster decay pathway (~ 20-40 ps) for the ligand treated films. Nevertheless, the resultant effect of ligand treatment leads to enhancement of photoconductivity and mobility.

5.5 References:

(1) Johnston, M. B.; Herz, L. M. *Acc. Chem. Res.* **2015**.

(2) Stranks, S. D.; Eperon, G. E.; Grancini, G.; Menelaou, C.; Alcocer, M. J. P.; Leijtens, T.; Herz, L. M.; Petrozza, A.; Snaith, H. J. *Science* **2013**, *342*, 341-344.

(3) Stranks, S. D.; Snaith, H. J. *Nat Nano* **2015**, *10*, 391-402.

(4)Brenner, T. M.; Egger, D. A.; Kronik, L.; Hodes, G.; Cahen, D. *Nat. Rev. Mater.***2016**, *1*, 15007.

(5) Stoumpos, C. C.; Kanatzidis, M. G. *Acc. Chem. Res.* **2015**, *48*, 2791-2802.

(6) Shi, D.; Adinolfi, V.; Comin, R.; Yuan, M.; Alarousu, E.; Buin, A.; Chen, Y.; Hoogland, S.; Rothenberger, A.; Katsiev, K.; Losovyj, Y.; Zhang, X.; Dowben, P. A.; Mohammed, O. F.; Sargent, E. H.; Bakr, O. M. *Science* **2015**, *347*, 519-522.

(7) Yang, W. S.; Noh, J. H.; Jeon, N. J.; Kim, Y. C.; Ryu, S.; Seo, J.; Seok, S. I. *Science* **2015**, *348*, 1234-1237.

(8) Green, M. A.; Emery, K.; Hishikawa, Y.; Warta, W.; Dunlop, E. D. *Prog. Photovolt.* **2016**, *24*, 905-913.

(9) Ahn, N.; Son, D.-Y.; Jang, I.-H.; Kang, S. M.; Choi, M.; Park, N.-G. *J. Am. Chem. Soc.* **2015**, *137*, 8696-8699.

(10) http://www.nrel.gov/ncpv/images/efficiency_chart.jpg, N. E. C.

(11) Kojima, A.; Teshima, K.; Shirai, Y.; Miyasaka, T. *J. Am. Chem. Soc.* **2009**, *131*, 6050-6051.

(12) Conings, B.; Drijkoningen, J.; Gauquelin, N.; Babayigit, A.; D'Haen, J.; D'Olieslaeger, L.; Ethirajan, A.; Verbeeck, J.; Manca, J.; Mosconi, E.; Angelis, F. D.; Boyen, H.-G. *Adv. Energy Mater.* **2015**, *5*, 1500477.

(13) Kulbak, M.; Cahen, D.; Hodes, G. *J. Phys. Chem. Lett.* **2015**, *6*, 2452-2456.

(14) Eperon, G. E.; Paterno, G. M.; Sutton, R. J.; Zampetti, A.; Haghighirad, A. A.; Cacialli, F.; Snaith, H. J. *J. Mater. Chem. A* **2015**, *3*, 19688-19695.

(15) Stoumpos, C. C.; Malliakas, C. D.; Peters, J. A.; Liu, Z.; Sebastian, M.; Im, J.; Chasapis, T. C.; Wibowo, A. C.; Chung, D. Y.; Freeman, A. J.; Wessels, B. W.; Kanatzidis, M. G. *Cryst. Growth Des.* **2013**, *13*, 2722-2727.

(16) Trots, D. M.; Myagkota, S. V. *J. Phys. Chem. Solids* **2008**, *69*, 2520-2526.

(17) Beal, R. E.; Slotcavage, D. J.; Leijtens, T.; Bowring, A. R.; Belisle, R. A.; Nguyen, W. H.; Burkhard, G. F.; Hoke, E. T.; McGehee, M. D. *J. Phys. Chem. Lett.* **2016**, *7*, 746-751.
(18) Sutton, R. J.; Eperon, G. E.; Miranda, L.; Parrott, E. S.; Kamino, B. A.; Patel, J. B.; Hörantner, M. T.; Johnston, M. B.; Haghighirad, A. A.; Moore, D. T.; Snaith, H. J. *Adv. Energy Mater.* **2016**, *6*, 1502458.
(19) Lee, J.-W.; Kim, D.-H.; Kim, H.-S.; Seo, S.-W.; Cho, S. M.; Park, N.-G. *Adv. Energy Mater.* **2015**, *5*, 1501310.
(20) Yi, C.; Luo, J.; Meloni, S.; Boziki, A.; Ashari-Astani, N.; Gratzel, C.; Zakeeruddin, S. M.; Rothlisberger, U.; Gratzel, M. *Energy. Environ. Sci.* **2016**, *9*, 656-662.
(21) Saliba, M.; Matsui, T.; Seo, J.-Y.; Domanski, K.; Correa-Baena, J.-P.; Nazeeruddin, M. K.; Zakeeruddin, S. M.; Tress, W.; Abate, A.; Hagfeldt, A.; Gratzel, M. *Energy. Environ. Sci.* **2016**, *9*, 1989-1997.
(22) McMeekin, D. P.; Sadoughi, G.; Rehman, W.; Eperon, G. E.; Saliba, M.; Hörantner, M. T.; Haghighirad, A.; Sakai, N.; Korte, L.; Rech, B.; Johnston, M. B.; Herz, L. M.; Snaith, H. J. *Science* **2016**, *351*, 151-155.
(23) Saliba, M.; Matsui, T.; Domanski, K.; Seo, J.-Y.; Ummadisingu, A.; Zakeeruddin, S. M.; Correa-Baena, J.-P.; Tress, W. R.; Abate, A.; Hagfeldt, A.; Grätzel, M. *Science* **2016**, *354*, 206-209.
(24) Hutter, E. M.; Sutton, R. J.; Chandrashekar, S.; Abdi-Jalebi, M.; Stranks, S. D.; Snaith, H. J.; Savenije, T. J. *ACS Energy Lett.* **2017**, *2*, 1901-1908.
(25) Protesescu, L.; Yakunin, S.; Bodnarchuk, M. I.; Krieg, F.; Caputo, R.; Hendon, C. H.; Yang, R. X.; Walsh, A.; Kovalenko, M. V. *Nano Lett.* **2015**, *15*, 3692-3696.
(26) Zhang, X.; Lin, H.; Huang, H.; Reckmeier, C.; Zhang, Y.; Choy, W. C. H.; Rogach, A. L. *Nano Lett.* **2016**, *16*, 1415-1420.
(27) Li, G.; Rivarola, F. W. R.; Davis, N. J. L. K.; Bai, S.; Jellicoe, T. C.; de la Peña, F.; Hou, S.; Ducati, C.; Gao, F.; Friend, R. H.; Greenham, N. C.; Tan, Z.-K. *Adv. Mater.* **2016**, *28*, 3528-3534.
(28) Song, J.; Li, J.; Li, X.; Xu, L.; Dong, Y.; Zeng, H. *Adv. Mater.* **2015**, *27*, 7162-7167.
(29) Akkerman, Q. A.; Gandini, M.; Di Stasio, F.; Rastogi, P.; Palazon, F.; Bertoni, G.; Ball, J. M.; Prato, M.; Petrozza, A.; Manna, L. *Nature Energy* **2016**, *2*, 16194.
(30) Swarnkar, A.; Marshall, A. R.; Sanehira, E. M.; Chernomordik, B. D.; Moore, D. T.; Christians, J. A.; Chakrabarti, T.; Luther, J. M. *Science* **2016**, *354*, 92-95.
(31) Xu, Y.-F.; Yang, M.-Z.; Chen, B.-X.; Wang, X.-D.; Chen, H.-Y.; Kuang, D.-B.; Su, C.-Y. *J. Am. Chem. Soc.* **2017**, *139*, 5660-5663.
(32) Makarov, N. S.; Guo, S.; Isaienko, O.; Liu, W.; Robel, I.; Klimov, V. I. *Nano Lett.* **2016**, *16*, 2349-2362.
(33) Hu, F.; Yin, C.; Zhang, H.; Sun, C.; Yu, W. W.; Zhang, C.; Wang, X.; Zhang, Y.; Xiao, M. *Nano Lett.* **2016**, *16*, 6425-6430.
(34) Mondal, N.; Samanta, A. *Nanoscale* **2017**, *9*, 1878-1885.
(35) Liu, Q.; Wang, Y.; Sui, N.; Wang, Y.; Chi, X.; Wang, Q.; Chen, Y.; Ji, W.; Zou, L.; Zhang, H. *Sci. Rep.* **2016**, *6*, 29442.
(36) Baxter, J. B.; Guglietta, G. W. *Anal. Chem.* **2011**, *83*, 4342-4368.
(37) Yettapu, G. R.; Talukdar, D.; Sarkar, S.; Swarnkar, A.; Nag, A.; Ghosh, P.; Mandal, P. *Nano Lett.* **2016**, *16*, 4838-4848.
(38) Yang, Z.; Surrente, A.; Galkowski, K.; Miyata, A.; Portugall, O.; Sutton, R. J.; Haghighirad, A. A.; Snaith, H. J.; Maude, D. K.; Plochocka, P.; Nicholas, R. J. *ACS Energy Lett.* **2017**, *2*, 1621-1627.
(39) Sebastian, M.; Peters, J. A.; Stoumpos, C. C.; Im, J.; Kostina, S. S.; Liu, Z.; Kanatzidis, M. G.; Freeman, A. J.; Wessels, B. W. *Phys. Rev. B* **2015**, *92*, 235210.

(40) Shi, H. a. D., Mao-Hua *Phys. Rev. B* **2014**, *90*, 174103.
(41) Saouma, F. O.; Stoumpos, C. C.; Kanatzidis, M. G.; Kim, Y. S.; Jang, J. I. *J. Phys. Chem. Lett.* **2017**, *8*, 4912-4917.
(42) Lakowicz, J. *Principles of Fluorescence Spectroscopy*; 3rd Edition ed.; Springer: New York, 2006.
(43) Guglietta, G. W.; Diroll, B. T.; Gaulding, E. A.; Fordham, J. L.; Li, S.; Murray, C. B.; Baxter, J. B. *ACS Nano* **2015**, *9*, 1820-1828.
(44) Wehrenfennig, C.; Eperon, G. E.; Johnston, M. B.; Snaith, H. J.; Herz, L. M. *Adv. Mater.* **2014**, *26*, 1584-1589.
(45) Talapin, D. V.; Murray, C. B. *Science* **2005**, *310*, 86-89.
(46) Luther, J. M.; Law, M.; Song, Q.; Perkins, C. L.; Beard, M. C.; Nozik, A. J. *ACS Nano* **2008**, *2*, 271-280.

Chapter 6

Understanding Carrier Dynamics in Reduced Graphene Oxide Film

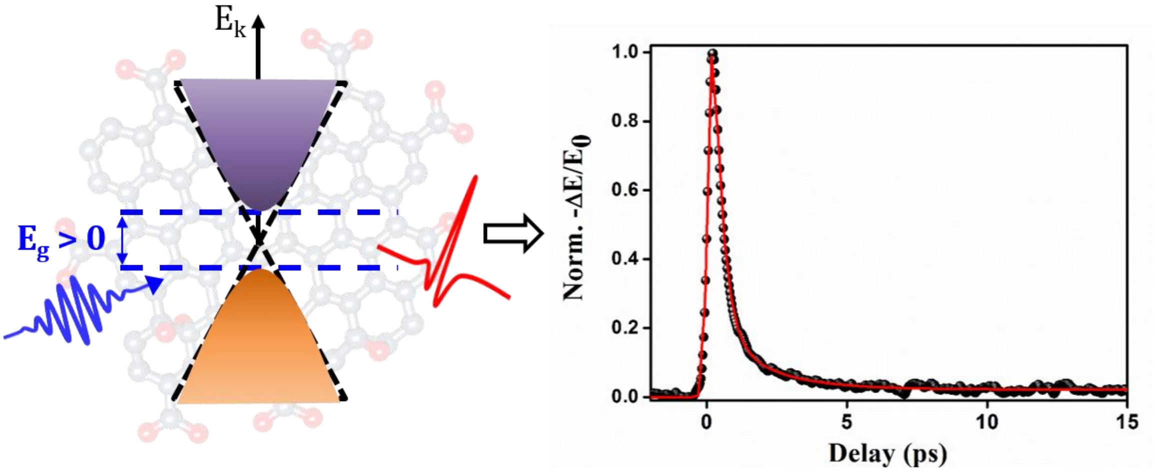

6.1 Introduction

Graphene, an allotrope of carbon is a single atomic layer of graphite. It is made up of tightly packed sp^2 hybridized carbon atoms organized in a two-dimensional honey comb lattice. It has a unique band structure with a zero band gap that is responsible for its remarkable optical and electronic properties.[1-5] Nevertheless, a zero band gap material may not be very useful for device fabrication as this means the device will never switch off. Therefore, to use graphene in optoelectronic devices band gap engineering needs to be done. Graphene has shown potential applications in photovoltaic cells,[6,7] mode-locked lasers,[8] supercapacitors, photodetectors,[9] etc. A cost effective way of manufacturing large scale graphene is by reduction of graphene oxide (GO), obtained by chemical exfoliation of graphite.[10,11] GO has sp^3 C atoms and is insulating. Reduction of GO by different processes like thermal annealing, chemical or electrochemical reduction gives reduced graphene oxide (rGO) which has sp^2 domains separated by sp^3 C atoms, that make rGO conductive.[12] The process of reduction is very crucial as it affects the quality of the rGO produced and determines how close the rGO properties are to pristine graphene. Also, rGO of desired band gap can be made by reducing GO in different processes. rGO can be described as a semimetal which is comparable to disordered multilayer graphene.[13]

Recently, Jha *et al.* have synthesized rGO using a novel technique where a moderate reducing agent has been used to reduce GO.[14] The rGO synthesized by this method exhibits a remarkable all-solid-state supercapacitor performance without any further treatment. Motivated by the quality of as synthesized rGO, we wanted to explore the carrier dynamics in this material. In this work, we utilized time resolved THz spectroscopy (TRTS) to measure the photoconductivity and study the relaxation dynamics of photoinduced free carriers in rGO film cast on high-density polyethylene (HDPE) substrate. The ac conductivity of the rGO film measured using the noncontact TRTS technique is comparable to the dc conductivity value determined by four probe I-V measurements. The overall carrier dynamics is very similar to that reported for single layer graphene.[15] We further reckon that rGO with sp^2 domains separated by sp^3 domains will have adequate optical anisotropy to be used as metamaterials.[16]

6.2 Synthesis and characterization of rGO

The GO and rGO preparations and characterizations were done by Plawan working with Dr. Nirmalya Ballav. The GO and rGO were synthesized by wet chemical methods. In short, graphite flake was stirred with concentrated H_2SO_4 at low temperature and $KMnO_4$ was added in portions. The mixture was further stirred at room-temperature (RT), followed by the slow addition of MQ water. Finally, water-hydrogen peroxide solution was added to the mixture. The collected brown colored material was washed with H_2O, HCl solution and finally with acetone and dried. The graphite oxide was further exfoliated in MQ water to make GO solution. To synthesize the rGO, iron(II) chloride was mixed with GO solution and stirred overnight at 94^oC. The black precipitate was filtered, washed with H_2O and a small amount of methanol and finally dried.

Preparation of Film: rGO was drop cast on high-density polyethylene (HDPE) substrate and dried overnight.

Characterization: Raman spectrum of the rGO was recorded using LabRAM HR, Horiba Jobin Yvon at 633 nm excitation wavelength. The powder X-ray diffraction (PXRD) data were recorded at room temperature using Bruker D8 Advance diffractometer, using Cu Kα radiation (λ = 1.5406 Å). The morphology of the rGO film and thickness of the film on HDPE substrate was recorded with Zeiss Ultra Plus field-emission scanning electron microscopy (FESEM). TEM images were obtained in a Philips CM200 machine.

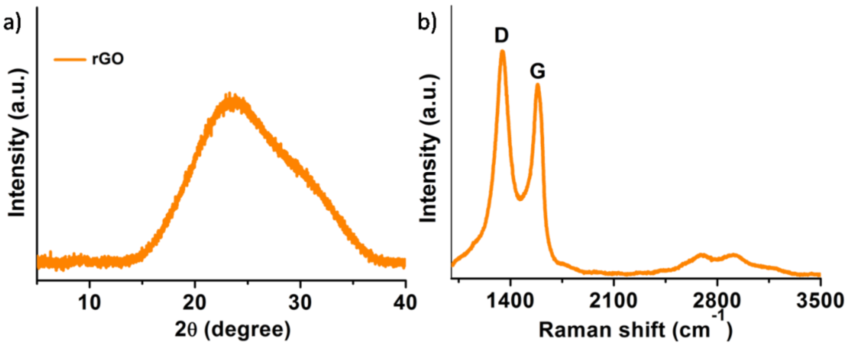

Figure 6.1. a) X-ray diffraction pattern and b) Raman spectrum of rGO.

From the X-ray diffraction pattern of rGO (Figure 6.1a), we can see that rGO has a peak at $2\theta \sim 23.4^0$ which corresponds to a d-spacing of 0.39 nm. Raman bands are observed at

1584.3 cm^{-1} (G band), 1345 cm^{-1} (D band) and 2685 cm^{-1} (2D band) as shown in Figure 6.1b. Bond stretching of the sp^2 C atoms gives rise to G band and breathing modes of sp^2 atoms in rings give rise to D band.[17] D band gives an estimate of the disorder in the lattice. From the intensity ratios of the D and G bands, the size of defect free domain, L_D, can be estimated from the equation.[17]

$$L_D^2(nm^2) = (1.8 \pm 0.5) \times 10^{-9} \lambda^4 ({}^{I_D}/_{I_G})^{-1}$$

The L_D for the rGO studied in this work is 10.9 ± 1.5 nm. This L_D is comparable to L_D of rGO synthesized by other methods.[18,19]

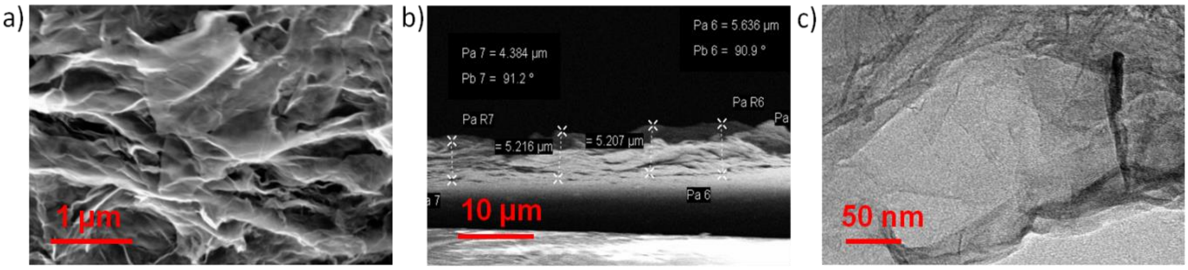

Figure 6.2. a) Morphology of rGO film coated on glass, b) thickness of rGO film on HDPE measured using SEM image, C) TEM image of rGO.

The average thickness of the rGO film on HDPE is ~5 µm as seen in SEM image (Figure 6.2b) of the cross-section of the film.

Using four probe I-V measurements (Figure 6.3a) technique, the DC conductivity of this material has been measured to be 5 S/cm. From UV-visible absorbance of the rGO film (Figure 6.3b), we can see that it has absorbance over the entire wavelength range with significant absorbance even at 1800 nm.

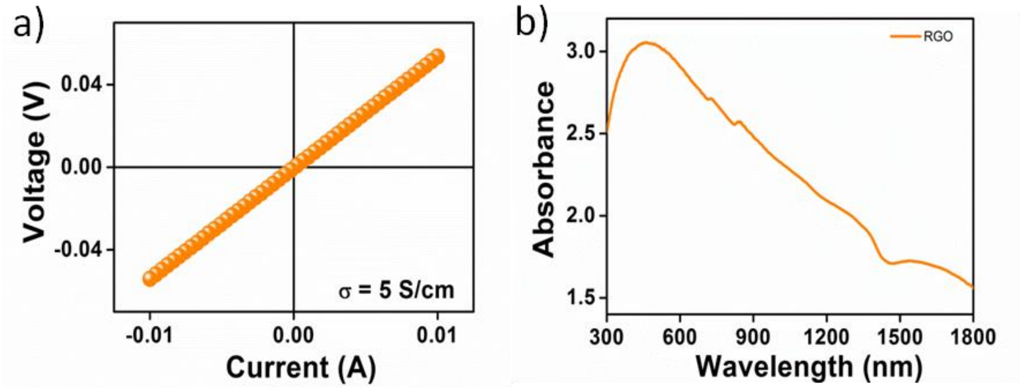

Figure 6.3. a) Four probe I-V measurement data. b) UV-vis absorbance of rGO on HDPE substrate.

6.3 Results and Discussion

6.3.1 Time Resolved THz Spectroscopy: Carrier Dynamics

Carrier dynamics of rGO film drop casted on non-conducting HDPE sheet was studied using TRTS. We studied the rapid relaxation dynamics of the rGO film after photo exciting the sample using 600 nm, 800 nm, and 1300 nm pump wavelengths. The rGO film showed positive photoconductivity. Conductivity in rGO occurs due to free carriers and almost instantaneously (~300 fs) the peak conductivity is reached. The pump induced change in THz transmissions was recorded by measuring the evolution of THz peak value as a function of pump-probe delay.

With increasing pump fluence, we observe an increase in the peak value of THz transients of rGO for excitation at all three wavelengths (Figure 6.4a, 6.5a, and 6.6a). Interestingly, the peak value shows a nonlinear dependence on fluence when excited with 600 nm and 800 nm wavelengths (Figure 6.4b and 6.5b), whereas a linear dependence was observed for 1300 nm excitation (Figure 6.6b).

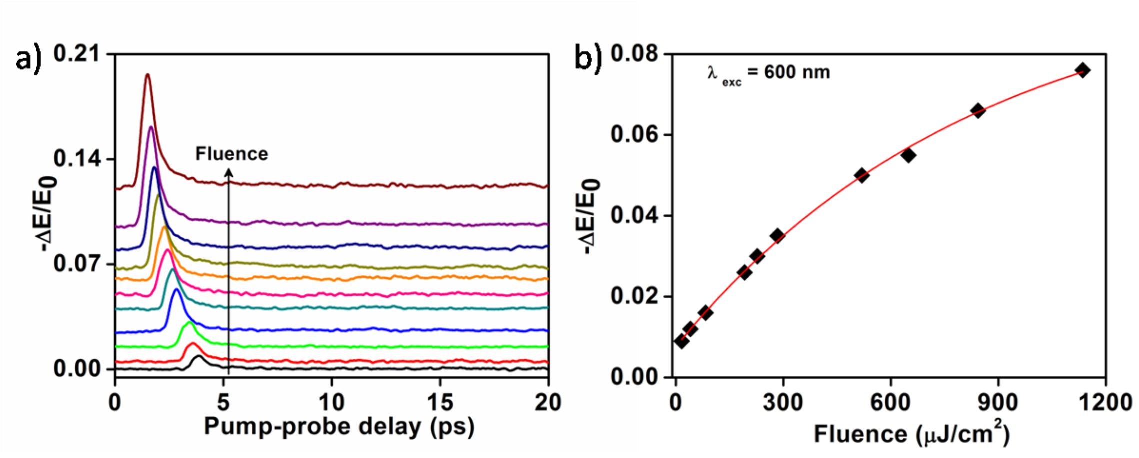

Figure 6.4. a) Frequency averaged photoinduced THz transmissions vs pump-probe delay for 600 nm pump with fluences ranging from ~16–1000 μJ/cm². The THz transients at fluences, except at 16 μJ/cm², have been offset horizontally and vertically for clarity. b) Peak THz transients with increasing excitation fluences.

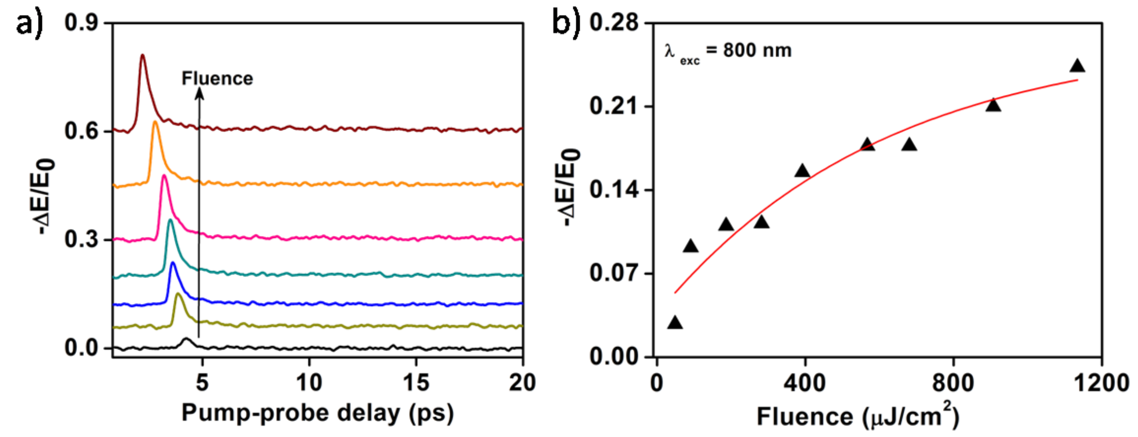

Figure 6.5. a) Frequency averaged photoinduced THz transmissions vs pump-probe delay for 800 nm pump with fluences ranging from ~50–1000 μJ/cm². The THz transients at fluences, except at 50 μJ/cm², have been offset horizontally and vertically for clarity. b) Peak THz transients with increasing excitation fluences.

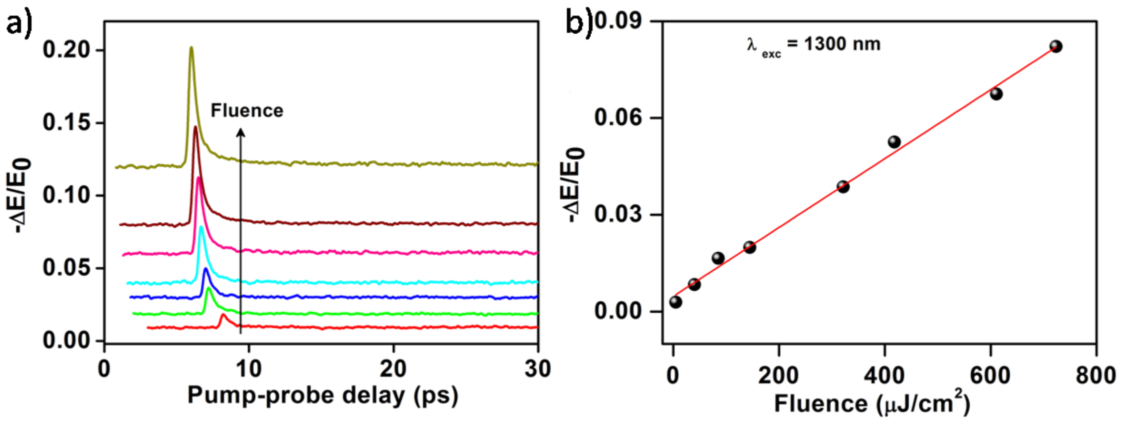

Figure 6.6. a) Frequency averaged photoinduced THz transmissions vs pump-probe delay for 1300 nm pump with fluences ranging from ~5–800 μJ/cm². The THz transients at fluences, except at 5 μJ/cm², have been offset horizontally and vertically for clarity. b) Peak THz transients with increasing excitation fluences.

When excited using 600 nm and 800 nm pump wavelengths, the nonlinear positive THz photoconductivity results from two competing processes. With increasing fluence more carriers are produced that lead to increased photoconductivity. Again, higher carrier concentration also gives rise to higher collision rate that decreases the conductivity. Thus, for 600 nm and 800 nm excitation, pump fluence dependence of the THz peak conductivity is the resultant of the two competing processes. When excited using 1300 nm pump, which corresponds to only 0.95 eV of energy, even at higher fluences the carriers do not have sufficient kinetic energy to undergo collisions and we see a linear dependence of THz peak conductivity with increasing fluence.

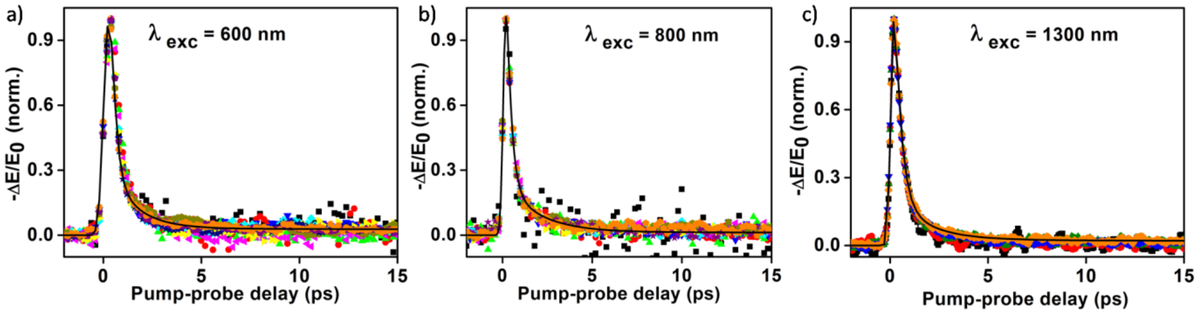

Figure 6.7. Normalized THz transients at different fluences for exciting with a) 600 nm, b) 800 nm and c) 1300 nm pump wavelengths. The solid line is triexponential fit to the photoconductivity decay.

On exciting the rGO with intense optical pump pulse there is an instantaneous increase in photoconductivity followed by a rapid decay. From the normalized photoconductivity decay of rGO, we observe that the decay is fluence independent for all excitation wavelengths. We fitted the decay to multiexponential function convoluted with a Gaussian of the form,

$$y = G(t - t_0) \otimes \sum_i a_i \exp\left[-\frac{t - t_0}{\tau_i}\right] \qquad (1)$$

where $G(t - t_0)$ is a Gaussian function centered at t_0 with FWHM of ~300 fs (the instrument response time of our TRTS experiment), and a_i is the contribution of the i^{th} exponential decay channel with a time constant τ_i towards the entire decay process. We got the best fit by fitting the decay to triexponential function keeping the time-scale for the slowest process to be fixed at 200 ps. Increasing the time for the slowest process improved the fit till 200 ps. Already there are studies reporting three time scales for conductivity decay in rGO with the slowest process having time scale of few hundred ps.[18,19] In this study also, we find three processes that are responsible for the rapid decay of carrier concentration in rGO. The timescales for the three processes and their contribution to the entire decay is listed in Tables 6.1-6.3. A very fast process (τ_1), even faster than our instrument response function (IRF) of 300 fs is present. The error associated with this timescale must be high since TRTS is limited by sub-ps temporal resolution. This fast timescale can be attributed to carrier-carrier interaction, Auger recombination or optical phonon emission.[18,20] Since the normalized decay is fluence independent, carrier- carrier interaction (n^2 dependent) and Auger recombination which is a three-body mechanism and highly fluence dependent may not be the fastest decay pathway in this case. rGO is likely to have high optical phonon energy as the optical phonon energy of graphene is ~ 200 meV. Therefore, high-energy optical phonon emission is the primary relaxation pathway in optically excited rGO.

Below the optical phonon energy, heat dissipation via acoustic phonon emission is the effective cooling pathway.[21] Nonetheless, theoretically electron and acoustic phonon coupling is momentum restricted and should take more than few hundreds of picoseconds discordant with experimental observations where this pathway is very fast and takes place within few picoseconds. Recent theoretical studies have tried to explain the fast process by elucidating the role of disorder that enables coupling between electrons and acoustic phonons via super collision processes.[22] The timescale (~ 1 ps) for the second decay process (τ_2) in rGO is comparable to the disorder mediated electron-phonon scattering processes (super-collision processes) that directs hot carrier cooling in graphene. [22,23]

The slowest process (τ_3), arises due to electron relaxation in deep trap states.[20] The trap states are formed due to the presence of residual oxygen bonded to sp^3 C atoms in rGO. Presence of these sp^3 sites in rGO impedes the ballistic carrier transport and foster hopping mechanism.[24,25] But the contribution from the slowest process is negligible as can be seen from a_3 values in the Tables 6.1-6.3 for the rGO studied in this work. This indicates that the rGO synthesized by the novel method[14] has fewer trap states thereby establishing the reduction method using iron (II) chloride an efficient one.

Table 6.1. Parameters obtained by fitting the THz transients of rGO excited using 600 nm pump wavelength.

Fluence (μJ/cm^2)	a_1	τ_1 (ps)	a_2	τ_2 (ps)	a_3	τ_3 (ps)
16.22	0.88 (0.02)	0.25 (0.02)	0.11 (0.12)	1.88 (0.10)	0.01 (0.000)	200
40.55	0.82 (0.04)	0.23 (0.025)	0.17 (0.1)	1.21 (0.06)	0.004 (0.000)	200
82.72	0.76 (0.08)	0.25 (0.02)	0.23 (0.06)	0.93 (0.04)	0.002 (0.000)	200
129.76	0.82 (0.05)	0.23 (0.01)	0.16 (0.03)	0.91 (0.04)	0.013 (0.000)	200
191.4	0.88 (0.02)	0.34 (0.01)	0.10 (0.02)	1.47 (0.08)	0.01 (0.000)	200
227.08	0.86 (0.02)	0.13 (0.02)	0.14 (0.42)	1.02 (0.03)	0.01 (0.000)	200
283.85	0.87 (0.07)	0.32 (0.38)	0.12 (0.16)	1.06 (0.03)	0.01 (0.000)	200
519.05	0.89 (0.02)	0.30 (0.01)	0.10 (0.01)	2.32 (0.07)	0.011 (0.000)	200
648.81	0.83 (0.31)	0.11 (0.01)	0.16 (0.02)	0.75 (0.01)	0.006 (0.000)	200

843.46	0.91 (0.03)	0.26 (0.003)	0.08 (0.01)	1.77 (0.03)	0.008 (0.000)	200
1135.42	0.87 (0.03)	0.23 (0.01)	0.12 (0.01)	1.35 (0.02)	0.011 (0.000)	200

Table 6.2. Parameters obtained by fitting the THz transients of rGO excited using 800 nm pump wavelength.

Fluence (μJ/ cm^2)	a_1	τ_1 (ps)	a_2	τ_2 (ps)	a_3	τ_3 (ps)
48.72	0.96 (0.17)	0.24 (0.03)	0.04 (0.07)	1.52 (0.90)	0.001 (0.009)	200
90.94	0.86 (0.02)	0.29 (0.01)	0.13 (0.01)	1.73 (0.07)	0.003 (0.000)	200
186.76	0.86 (0.03)	0.25 (0.01)	0.13 (0.02)	1.46 (0.07)	0.007 (0.001)	200
282.58	0.89 (0.01)	0.33 (0.01)	0.10 (0.01)	1.75 (0.09)	0.013 (0.001)	200
393.01	0.87 (0.01)	0.3 (0.01)	0.12 (0.01)	1.53 (0.06)	0.011 (0.000)	200
568.41	0.70 (0.03)	0.26 (0.01)	0.29 (0.04)	0.85 (0.03)	0.017 (0.000)	200
682.09	0.77 (0.03)	0.22 (0.01)	0.22 (0.03)	0.87 (0.03)	0.013 (0.000)	200
909.45	0.89 (0.01)	0.28 (0.00)	0.09 (0.01)	1.85 (0.05)	0.017 (0.000)	200
974.42	0.87 (0.02)	0.27 (0.01)	0.12 (0.01)	1.88 (0.06)	0.007 (0.001)	200

Table 6.3. Parameters obtained by fitting the THz transients of rGO excited using 1300 nm pump wavelength.

Fluence (μJ/cm^2)	a_1	τ_1 (ps)	a_2	τ_2 (ps)	a_3	τ_3 (ps)
32	0.81 (0.02)	0.31 (0.01)	0.18 (0.03)	1.12 (0.05)	0.004 (0.001)	50.38 (11)
320	0.89 (0.01)	0.37 (0.00)	0.10 (0.01)	1.75 (0.06)	0.011 ± (0.001)	88.17 (7.9)
418	0.89 (0.01)	0.37 (0.00)	0.10 (0.01)	1.75 (0.06)	0.011 (0.001)	86.76 (7.7)

610	0.87 (0.00)	0.33 (0.00)	0.12 (0.01)	1.67 (0.03)	0.008 (0.000)	100 (9.2)
723	0.87 (0.00)	0.33 (0.00)	0.12 (0.01)	1.69 (0.03)	0.014 (0.000)	89.37 (4.6)

6.3.2 Photoconductivity and mobility

The photoconductivity $\Delta\sigma(t_p)$ of the film which is proportional to the photo-induced THz transmission ($\frac{-\Delta E(t_p)}{E_0(t_p)}$), is given by:

$$\Delta\sigma(t_p) = \frac{\varepsilon_0 c}{d}(n_a + n_b)\frac{-\Delta E(t_p)}{E_0(t_p)} \qquad (2)$$

where ε_0 is the permittivity of free space, c is the speed of light, d is the thickness of the photoexcited sample, and n_a and n_b are the refractive indices of the media on either side of the photoexcited sample. Here, n_a =1 for air and n_b = 1.54 for HDPE substrate. The fluence dependent peak photoconductivity values calculated using above equation range from 0.7- 6 S/cm for the rGO film. The conductivity value obtained by TRTS which measures the transient local ac conductivity in a noncontact fashion is comparable to that obtained from four probe DC I-V measurement (5 S/cm).

Using the equation, $\varphi\mu \cong \frac{\Delta\sigma}{qN_0}$, effective carrier mobility for rGO film, at the peak of THz transients are calculated, where q is the elementary charge, N_0 is the total carrier density and φ is the photon to free carrier conversion ratio. The effective mobility values range from 0.3 – 3.85 cm^2/(V.s) depending on fluence and excitation wavelength. With an increase in energy of the pump light, increase in mobility value is observed, with the highest value being 3.85 cm^2/(V.s) for 600 nm excitation. The mobility value is reasonably high and comparable to other rGO films.[26] The hole mobilities for films are 0.12 cm^2/(V·s) (chemical reduction) and 10.4 cm^2/(V·s) (chemical + thermal reduction), respectively. High hole mobility of 123 cm^2/ (V.s) is also reported.[27]

6.4 Conclusion

Employing TRTS, we have measured the photoconductivity and studied the carrier dynamics in this rGO film. The ac conductivity of the rGO film measured using the noncontact TRTS technique is comparable to the dc conductivity value determined by four probe I-V measurements. The overall carrier dynamics is very similar to that reported for single layer graphene. The rapid relaxation of carriers in the rGO film is mainly dictated by 1) optical phonon emissions (< 300 fs), 2) disorder mediated acoustic phonon emissions of thermalized carriers (1-2 ps), and 3) inefficient slow relaxation of electrons and holes in deep trap states (50-200 ps). The mobility value depends on excitation wavelength and is reasonably high (~ 3.85 $cm^2/(V.s)$).

6.5 References

(1) Novoselov, K. S.; Geim, A. K.; Morozov, S. V.; Jiang, D.; Katsnelson, M. I.; Grigorieva, I. V.; Dubonos, S. V.; Firsov, A. A. *Nature* **2005**, *438*, 197-200.
(2) Zhang, Y.; Tan, Y.-W.; Stormer, H. L.; Kim, P. *Nature* **2005**, *438*, 201-204.
(3) Castro Neto, A. H.; Guinea, F.; Peres, N. M. R.; Novoselov, K. S.; Geim, A. K. *Rev. of Mod. Phys.* **2009**, *81*, 109-162.
(4) Kim, K. S.; Zhao, Y.; Jang, H.; Lee, S. Y.; Kim, J. M.; Kim, K. S.; Ahn, J.-H.; Kim, P.; Choi, J.-Y.; Hong, B. H. *Nature* **2009**, *457*, 706-710.
(5) Liu, M.; Yin, X.; Ulin-Avila, E.; Geng, B.; Zentgraf, T.; Ju, L.; Wang, F.; Zhang, X. *Nature* **2011**, *474*, 64-67.
(6) Shi, E.; Li, H.; Yang, L.; Zhang, L.; Li, Z.; Li, P.; Shang, Y.; Wu, S.; Li, X.; Wei, J.; Wang, K.; Zhu, H.; Wu, D.; Fang, Y.; Cao, A. *Nano Lett.* **2013**, *13*, 1776-1781.
(7) Miao, X.; Tongay, S.; Petterson, M. K.; Berke, K.; Rinzler, A. G.; Appleton, B. R.; Hebard, A. F. *Nano Lett.* **2012**, *12*, 2745-2750.
(8) Sun, Z.; Hasan, T.; Torrisi, F.; Popa, D.; Privitera, G.; Wang, F.; Bonaccorso, F.; Basko, D. M.; Ferrari, A. C. *ACS Nano* **2010**, *4*, 803-810.
(9) Xia, F.; Mueller, T.; Lin, Y.-m.; Valdes-Garcia, A.; Avouris, P. *Nat Nano* **2009**, *4*, 839-843.
(10) Gilje, S.; Han, S.; Wang, M.; Wang, K. L.; Kaner, R. B. *Nano Lett.* **2007**, *7*, 3394-3398.
(11) Gómez-Navarro, C.; Weitz, R. T.; Bittner, A. M.; Scolari, M.; Mews, A.; Burghard, M.; Kern, K. *Nano Lett.* **2007**, *7*, 3499-3503.
(12) Loh, K. P.; Bao, Q.; Eda, G.; Chhowalla, M. *Nat Chem* **2010**, *2*, 1015-1024.
(13) Chen, J.-H.; Cullen, W. G.; Jang, C.; Fuhrer, M. S.; Williams, E. D. *Phys. Rev. Lett.* **2009**, *102*, 236805.
(14) Jha, P. K.; Singh, S. K.; Kumar, V.; Rana, S.; Kurungot, S.; Ballav, N. *Chem*, *3*, 846-860.
(15) Jnawali, G.; Rao, Y.; Yan, H.; Heinz, T. F. *Nano Lett.* **2013**, *13*, 524-530.
(16) Kravets, V. G.; Marshall, O. P.; Nair, R. R.; Thackray, B.; Zhukov, A.; Leng, J.; Grigorenko, A. N. *Optics Express* **2015**, *23*, 1265-1275.
(17) Cançado, L. G.; Jorio, A.; Ferreira, E. H. M.; Stavale, F.; Achete, C. A.; Capaz, R. B.; Moutinho, M. V. O.; Lombardo, A.; Kulmala, T. S.; Ferrari, A. C. *Nano Lett.* **2011**, *11*, 3190-3196.
(18) Kar, S.; Jayanthi, S.; Freysz, E.; Sood, A. K. *Carbon* **2014**, *80*, 762-770.

(19) Xing, X.; Zhao, L.; Zhang, Z.; Fang, L.; Fan, Z.; Liu, X.; Lin, X.; Xu, J.; Chen, J.; Zhao, X.; Jin, Z.; Ma, G. *J. Phys. Chem. C* **2017**, *121*, 2451-2458.
(20) Kaniyankandy, S.; Achary, S. N.; Rawalekar, S.; Ghosh, H. N. *J. Phys. Chem. C* **2011**, *115*, 19110-19116.
(21) Mihnev, M. T.; Kadi, F.; Divin, C. J.; Winzer, T.; Lee, S.; Liu, C.-H.; Zhong, Z.; Berger, C.; de Heer, W. A.; Malic, E.; Knorr, A.; Norris, T. B. *Nat. Comm.* **2016**, *7*, 11617.
(22) Song, J. C. W.; Reizer, M. Y.; Levitov, L. S. *Phys. Rev. Lett.* **2012**, *109*, 106602.
(23) Graham, M. W.; Shi, S.-F.; Ralph, D. C.; Park, J.; McEuen, P. L. *Nat Phys* **2013**, *9*, 103-108.
(24) Bagri, A.; Mattevi, C.; Acik, M.; Chabal, Y. J.; Chhowalla, M.; Shenoy, V. B. *Nat. Chem.* **2010**, *2*, 581.
(25) Du, X.; Skachko, I.; Barker, A.; Andrei, E. Y. *Nat. Nanotechnol.* **2008**, *3*, 491.
(26) Kim, H.-J.; Kim, D.; Jung, S.; Yi, S. N.; Yun, Y. J.; Chang, S. K.; Ha, D. H. *J. Phys. Chem. C* **2015**, *119*, 28685-28690.
(27) Feng, H.; Cheng, R.; Zhao, X.; Duan, X.; Li, J. *Nat. Comm.* **2013**, *4*, 1539.

Chapter 7

Summary and Outlook

Terahertz (THz) Spectroscopy, a relatively new spectroscopic technique, can provide significant insights into numerous physical, chemical, and biological processes occurring in picosecond time scales with energies in meV range. Its frequency range roughly spans from 0.3 to 20 THz, where 1 THz corresponds to 33.3 cm^{-1} in wavenumber, 4 meV in energy and 300 μm in wavelength. This thesis describes the setup of a THz spectrometer offering an ultra-broad bandwidth (0.5-15 THz), optical pump THz probe experimental setup and how THz can be used as a spectroscopic tool to study the dynamics occurring in condensed matter. Ambient air was used for broadband generation and detection of THz light. Unlike other spectroscopic methods which measure only intensity, THz spectroscopy measures the transient electric field and thus provides both amplitude and phase of the spectral components making up the THz pulse. Employing amplitude and phase, frequency dependent complex refractive index, complex dielectric functions, and complex conductivity can be calculated.

Using time domain THz spectroscopy, the complex dielectric properties of polar liquids have been studied and it has been found that dielectric response has contributions from Debye relaxation and three damped harmonic oscillators. The dielectric study of carried out at a broad spectral range in THz frequency domain will enable researcher to choose these alcohols as a solvent prudently in THz experiments.

The time domain study was further extended to time resolved study where pump probe experiments were performed on semiconductor nanocrystals (NCs) using an optical pump and THz probe (OPTP). This enabled the measurement of transient photoconductivity of semiconductor NCs without any electrical contact. Understanding the photophysics of semiconductors is crucial to their better utilization in photovoltaic and photocatalytic devices. Hot carrier transfer from colloidal $CsPbBr_3$ NC to molecular acceptors occurring in sub-ps timescale has been studied. Studying time resolved THz spectroscopy (TRTS) of NC-molecule interface reveals the response from the NCs eliminating the contribution from the molecule. Having understood this system one would be in better position to understand the dynamics in bulk NC/interface that is used in a PV function. We will extend our study to such systems in future.

Cubic $CsPbI_3$ has the appropriate band gap of 1.73 eV for photovoltaic applications. To use these NCs in optoelectronic devices, the insulating capping ligands need to be removed. Using TRTS, cubic $CsPbI_3$ NC films and effect of ligand treatment on photoconductivity and mobility of the films, under ambient condition have been investigated. Washing the NC films with MeOAc and $Pb(OAc)_2$ displace the insulating oleylamine ligands used for capping the NCs which results in increased inter NC coupling. This enhances the conductivity and mobility of the films but also introduces new trap states. Further studies using suitable capping ligands that will passivate the trap states without impeding the transport properties of the NCs will help to improve the photovoltaic efficiencies.

Lastly, the carrier dynamics of reduced graphene oxide prepared by a novel method was probed using TRTS. The synthesis procedure of rGO is extremely crucial as it affects the quality of the rGO produced and determines how close the rGO properties are to pristine graphene. TRTS can be used not only to find out the transport properties of the rGO film, but it can also provide insights about the rapid carrier relaxations occurring in rGO films. The ac conductivity of the rGO film measured using the noncontact TRTS technique is similar to the dc conductivity value determined by four probe I-V measurements. The overall carrier dynamics is very similar to that reported for single layer graphene.

My Orders My Library My Profile **Welcome** sohinis@students.iiserpune.ac.in Log out | Help

My Orders > Orders > All Orders

License Details

This Agreement between Ms. Sohini Sarkar ("You") and Elsevier ("Elsevier") consists of your license details and the terms and conditions provided by Elsevier and Copyright Clearance Center.

printable details

License Number	4174190519378
License date	Aug 22, 2017
Licensed Content Publisher	Elsevier
Licensed Content Publication	Chemical Physics Letters
Licensed Content Title	Broadband terahertz dielectric spectroscopy of alcohols
Licensed Content Author	Sohini Sarkar,Debasis Saha,Sneha Banerjee,Arnab Mukherjee,Pankaj Mandal
Licensed Content Date	Jun 16, 2017
Licensed Content Volume	678
Licensed Content Issue	n/a
Licensed Content Pages	7
Type of Use	reuse in a thesis/dissertation
Portion	full article
Format	both print and electronic
Are you the author of this Elsevier article?	Yes
Will you be translating?	No
Title of your thesis/dissertation	Terahertz Spectroscopic Study of Solvent Dynamics, Charge Transfer and Carrier Recombination
Expected completion date	Aug 2017
Estimated size (number of pages)	130
Requestor Location	Ms. Sohini Sarkar Main Academic Building IISER, Pune Dr Homi Bhabha Road Pune, Maharashtra 411008 India Attn: Ms. Sohini Sarkar
Total	**0.00 USD**

BACK

Home Account Info Help

Title: Terahertz Spectroscopic Probe of Hot Electron and Hole Transfer from Colloidal CsPbBr3 Perovskite Nanocrystals
Author: Sohini Sarkar, Vikash Kumar Ravi, Sneha Banerjee, et al
Publication: Nano Letters
Publisher: American Chemical Society
Date: Aug 1, 2017

Logged in as:
Sohini Sarkar
Account #:
3001172446
LOGOUT

PERMISSION/LICENSE IS GRANTED FOR YOUR ORDER AT NO CHARGE

This type of permission/license, instead of the standard Terms & Conditions, is sent to you because no fee is being charged for your order. Please note the following:

- Permission is granted for your request in both print and electronic formats, and translations.
- If figures and/or tables were requested, they may be adapted or used in part.
- Please print this page for your records and send a copy of it to your publisher/graduate school.
- Appropriate credit for the requested material should be given as follows: "Reprinted (adapted) with permission from (COMPLETE REFERENCE CITATION). Copyright (YEAR) American Chemical Society." Insert appropriate information in place of the capitalized words.
- One-time permission is granted only for the use specified in your request. No additional uses are granted (such as derivative works or other editions). For any other uses, please submit a new request.

BACK CLOSE WINDOW